UNIVERSIDAD COMPLUTENSE DE MADRID

FACULTAD DE CIENCIAS FÍSICAS

TESIS DOCTORAL

Cataclysmic Variables in Wide Field Surveys/Variables Cataclísmicas en cartografíados de gran campo

MEMORIA PARA OPTAR AL GRADO DE DOCTOR

PRESENTADA POR

Javier Abril Ibáñez

DIRECTOR

Alessandro Ederoclite

UNIVERSIDAD COMPLUTENSE DE MADRID
FACULTAD DE CIENCIAS FÍSICAS

TESIS DOCTORAL

Cataclysmic Variables in Wide Field Surveys

MEMORIA PARA OPTAR AL GRADO DE DOCTOR

PRESENTADA POR

Javier Abril Ibáñez

DIRECTOR

Alessandro Ederoclite

UNIVERSIDAD COMPLUTENSE DE MADRID

DOCTORAL THESIS

Cataclysmic Variables in Wide Field Surveys/Variables Cataclísmicas en cartografíados de gran campo

---

Author:
Javier ABRIL IBÁÑEZ

Supervisor:
Prof. Dr. Alessandro EDEROCLITE

UNIVERSIDAD
COMPLUTENSE
MADRID

A thesis submitted in fulfillment of the requirements for the degree of Doctor of Philosophy

in the

Departamento de Física de la Tierra y Astrofísica

UNIVERSIDAD COMPLUTENSE DE MADRID

Abstract

Facultad de Ciencias Físicas
Departamento de Física de la Tierra y Astrofísica

Doctor of Philosophy

Cataclysmic Variables in Wide Field Surveys/Variables Cataclísmicas en cartografíados de gran campo

by Javier ABRIL IBÁÑEZ

English version

Introduction. Cataclysmic Variables (CVs) are interacting binary systems comprised of a white dwarf (WD) and a secondary star, typically a red dwarf (RD). The secondary is transferring material through the inner Lagrangian point (L_1) which, in absence of strong magnetic fields, forms an accretion disc surrounding the central WD. The evolution of CVs is driven by angular momentum loss, moving from long orbital periods and high mass transfer rates to short orbital periods and low mass trasnfer rates. Their evolution proceeds in this way until reaching the period minimum at ~ 78 min. In addition, there is an abrupt drop in the number of systems with periods between 2 h and 3 h, the period gap. Below the gap, the main mechanism of angular momentum loss is governed by gravitational radiation while above it, the stronger magnetic braking dominates.

Objectives. Nonetheless, discrepancies between theory and observations exist, and a larger and well known population of CVs becomes necessary. This work intends to enlarge the CV sample to help solving these disagreements and, in this journey, several analyses related to the evolution of these systems and the properties of their different subtypes are also discussed.

Methodology. In this thesis, an analysis of the absolute magnitudes and colours of CVs is provided to give continuity to the understanding of the evolution of these systems. Several methodologies to find new CVs, using a combination of public wide field surveys are presented. The Javalambre-Photometric Local Universe Survey, J-PLUS, is the base-line source of data, which is combined with the Wide-field Infrared Survey Explorer (WISE) and the Global Astrometric Interferometer for Astrophysics survey (Gaia). The methodologies make use of classical techniques such as colour-colour and Hertzsprung–Russell diagrams. They shed light about the complications related to the discovery of these objects as well as about the limitations of the said techniques. Therefore, subsequently more recent techniques in the field of Machine learning (ML) are tested. Colour-colour and colour-magnitude diagrams do not fit well with missing data, usually bringing loss of information and decrease of completeness. Moreover, cutting criteria do not usually capture the more subtle patterns and conversely, ML techniques can provide objective results by capturing less noticeable patterns. A comparison of different ML techniques to predict missing values (data imputation technique), result from cross-matching data between different surveys, is exhibited. This new generated dataset is used to train a fully connected neural network in charge of finding new CV systems.

Results. The color-color methodologies fail to define a sample of CVs with a satisfactory purity coefficient, including numerous contaminants. However, the resulting set of data from imputed values fed into the neural network allows a wider parametric space to be explored, yielding a completeness of 87% and a purity of 59%.

UNIVERSIDAD COMPLUTENSE DE MADRID

Abstract

Facultad de Ciencias Físicas
Departamento de Física de la Tierra y Astrofísica

Doctor of Philosophy

Cataclysmic Variables in Wide Field Surveys/Variables Cataclísmicas en cartografíados de gran campo

by Javier ABRIL IBÁÑEZ

Versión en español

Introducción. Las Variables Cataclísmicas (CV por sus siglas en inglés) son sistemas binarios que interactúan entre sí, compuestos por una enana blanca y una estrella secundaria, típicamente una enana roja. La secundaria transfiere material a través del punto interno de Lagrange (L_1) que, en ausencia de fuertes campos magnéticos, forma un disco de acreción que rodea a la enana blanca central. La evolución de las CVs está impulsada por la pérdida de momento angular, pasando de largos períodos orbitales y altas transferencias de masa a períodos orbitales cortos y bajas transferencias de masa. Su evolución prosigue de esta manera hasta alcanzar el período mínimo de $\sim 78\,\mathrm{min}$. Además, hay un descenso abrupto en el número de sistemas con períodos entre 2 h y 3 h, el ′period gap′. Por debajo del gap, el principal mecanismo de pérdida de momento angular se rige por la radiación gravitatoria, mientras que por encima de él, domina el frenado magnético más fuerte.

Objetivos. Sin embargo, existen discrepancias entre teoría y observaciones, y por tanto, contar con una mayor y bien conocida población de CVs se hace necesaria. Este trabajo pretende ampliar la muestra de CVs para ayudar a resolver estos desacuerdos y de camino, también se discuten varios análisis relacionados con la evolución de estos sistemas y las propiedades de sus diferentes subtipos.

Metodología. En esta tesis, se proporciona un análisis de las magnitudes absolutas y los colores de las CVs para dar continuidad a la comprensión de la evolución de estos sistemas. Se presentan varias metodologías para encontrar nuevas CVs, utilizando una combinación de cartografíados de gran campo públicos. El cartografiado Javalambre-Photometric Local Universe Survey, J-PLUS, es la fuente de datos base, que se combina con el Wide-field Infrared Survey Explorer (WISE) y el Global Astrometric Interferometer for Astrophysics survey (Gaia). Las metodologías utilizan técnicas clásicas como los diagramas color-color y Hertzsprung-Russell. Esta metodologías arrojan luz sobre las complicaciones relacionadas con el descubrimiento de estos objetos, así como las limitaciones de dichas técnicas. Por tanto, posteriormente se prueban técnicas más recientes en el campo del Machine learning (ML). Los diagramas color-color y color-magnitud no encajan bien con datos ausentes, lo que suele traer la pérdida de información y la disminución de completitud. Además, los criterios de corte no suelen captar los patrones más sutiles y, en cambio, las técnicas de ML pueden dar resultados objetivos al captar los patrones menos perceptibles. Se exhibe una comparación de diferentes técnicas de ML para predecir valores ausentes (técnicas de imputación de datos), resultado del cruce de datos entre diferentes cartografiados. Este nuevo conjunto de datos generados se utiliza para entrenar una red neural totalmente conectada encargada de encontrar nuevas CVs.

Resultados. Las metodologías de color-color no logran definir una muestra de CVs con un coeficiente de pureza satisfactorio, incluyendo numerosos contaminantes. Sin embargo, el conjunto de datos resultante de los valores imputados introducidos en la red neuronal permite explorar un espacio de parámetros más amplio, dando una completitud del 87% y una pureza del 59%.

Acknowledgements

If there is a key person who has made possible the writing of this thesis, that is Alessandro Ederoclite, whose role has gone beyond that of a supervisor.

Thank you for clearing the way and letting me choose my own path. Thank you for believing in me when it was more challenging, for taking the risk, for your commitment. Thank you for being an example inside and outside the academy. And above all, for your infinite patience.

But also thank you for your contagious enthusiasm, for your generosity, your joy, sensitivity and innocence... And of course I can’t forget to mention your entertaining "ability" for poetry and rhyme. Grazie per aver scelto di insegnare.

This thesis would have been a very different work if it had not been for the contribution of Linda Schmidtobreick, who selflessly opened the doors of her "house" to me. Thank you for your ability to simplify and make the difficult easy and for teaching me to focus on the important things. Thank you also for putting up with my quirks and giving the push with the right intensity at the right time.

To Anna Pala and Valentin Le Gouellec, for all those infinite conversations and "conversamoles" improvised anywhere; to GOT, the "grupo de operaciones telescópicas de CEFCA", everything began with them; to Jesús Corral for his precise eye; and to Anacris, who was always listening to my pains and sufferings radiating positivity. Thanks to all of them the journey has been much easier.

I can’t stop thanking my family and friends who always convinced me that this thesis had to be written when I had least strength.

Contents

List of Figures

List of Tables

Chapter 1

Overview

1.1 Introduction

Cataclysmic Variables (CVs) are interacting binaries comprising a white dwarf (WD) which is accreting mass from a less evolved companion, the secondary star, which typically is a low-mass late-type main sequence star. The transferred material, depending on the magnetic activity of the WD, either forms an accretion disc surrounding the central WD or its trajectory is interrupted by the magnetic field, forcing the accreting material to fall along the field lines (see e.g., Warner 1995, Hellier 2001 and Knigge, Baraffe, and Patterson 2011 for comprehensive reviews).

The evolution of these binaries is driven by angular momentum loss, which controls the mass transfer rate and the corresponding change of orbital period (Townsley and Gänsicke, 2009). As a consequence of the angular momentum loss and the mechanisms driving it, CVs move from long orbital periods and high mass transfer rates to short orbital periods and low mass transfer rates (Paczynski and Sienkiewicz 1983; Townsley and Gänsicke 2009; Pala et al. 2017). In the standard model of CV evolution (Howell, Nelson, and Rappaport 2001; Goliasch and Nelson 2015) this is explained by the presence of different mechanisms of angular momentum loss characterized by different efficiencies together with changes in the internal structure of the secondary (Knigge, Baraffe, and Patterson, 2011). The evolution of CVs proceeds in this way until the system reaches the period minimum at $\sim$ 76–80 minutes (Knigge 2006; Gänsicke et al. 2009; Kalomeni et al. 2016) in which the donor mass has become so low that core H-burning ceases, and the star turns into a brown dwarf (BD). Consequently, the orbital separation and period now increases as the mass-transfer continues becoming in the so-called period bouncers. Theory predicts that 70% of the CVs (Kolb, 1993) should be period bouncers, faint systems with BD donors in the period range $\sim$ 76 min $\leq P_{\mathrm{orb}} \leq 2\,\mathrm{h}$.

On their way to the period minimum, observations show an abrupt drop in the number of systems with periods between 2 h and 3 h, referred to as the period gap. Below this range ($P_{\text{orb}} < 2\,\text{h}$), systems have low mass-transfer rates mainly governed by gravitational radiation (GR) while the higher mass-transfer rates above the gap ($P_{\text{orb}} > 3\,\text{h}$) are a consequence of the stronger magnetic braking (MB), see Rappaport, Joss, and Verbunt (1983); Spruit and Ritter (1983); Hameury et al. (1988); Davis et al. (2008). The standard explanation for the gap suggests that MB switches off or is greatly reduced when the secondary becomes fully convective, quenching/weakening the magnetic dynamo (observational evidence of this can be found in Zorotovic and Schreiber 2017 and Schreiber et al. 2010). As a consequence, the secondary contracts to its thermal equilibrium and detaches from its Roche lobe. This occurs at an orbital period of $\sim 3\,\text{h}$. The continuing angular momentum loss by GR shrinks the orbit until it reaches a period of about 2 h, when the Roche lobe makes contact with the stellar surface and mass-transfer is re-established, albeit, at a lower level.

Some discrepancy from this general picture come from magnetic CVs which show no evidence of a period gap (Townsley and Gänsicke 2009). Some CV sub-types unexpectedly overabundant in specific period ranges, e.g. the group of SW Sex stars, peak just above the period gap at periods between 3 and 4 h (Schmidtobreick 2017 or Schmidtobreick, Rodríguez-Gil, and Gänsicke 2012). Moreover, in disparity with the expected 70% CV population, only a selected few period bouncers have been identified (e.g. Pala et al. 2018). It is not clear yet whether these differences are intrinsic or due to observational biases of the overall CV population.

Since the structure of both components is relatively simple, CVs are one of the best sources to test our understanding of many astrophysical phenomena involving evolution of compact, interacting binaries and accretion phenomena. Their study helps to resolve standing discrepancies between current population models and observations in many present and complex topics including black hole binaries, short gamma-ray bursts, X-ray transients, millisecond pulsars and Supernovae Ia.

1.2 The White Dwarf

White Dwarfs are compact objects with low luminosity and radius on the order of that of the Earth. It is a faint star at the end-stage of the evolution of intermediate and low-mass stars. WDs evolve from stars with an initial mass of up to four solar masses. As the hydrogen fuel runs out in the entire core, the star becomes a red giant. If the red giant does not have enough temperature to fuse carbon and oxygen, the gravitational forces compress its core and the envelope is expelled, thus producing a planetary nebula. The star loses a major fraction of its original mass through stellar winds and through its ejected envelope. The hot planetary-nebula nucleus left behind will eventually cool down to become a WD. Following the complete exhaustion of its reservoir of thermal energy, the WD reaches the final stage of its evolution and becomes a cold and inert stellar remnant known as black dwarf.

Unlike most other stars, WDs are not supported against their own gravitation by thermal gas pressure but by the degeneration pressure of the electron gas in their core. This electron gas[1] at high densities adopts a particular configuration that obeys Fermi-Dirac statistics (Fermi 1926 and Dirac 1926). WDs reach densities up to 10^6 $\mathrm{g\,cm^{-3}}$ or even higher, only exceeded by neutron stars and black holes. At these densities come into play *Heisenberg's principle of indetermination* and *Pauli's exclusion principle* for the electrons, generating such electronic degeneration pressure which opposes the collapse of the star. The application of the Fermi-Dirac statistics and of special relativity to the study of the equilibrium structure of a WD yields to a mass-radius ratio constraint where a unique radius is assigned to a given mass; the larger the mass, the smaller the radius. Moreover, it is also derived a limiting mass for WDs, the Chandrasekhar limit, $\sim 1.4\ \mathrm{M}_\odot$. If a WD reaches that limit, the gravitational pressure would either force the electrons to combine with the protons to form a neutron star or explode as a type Ia Supernova.

Typical masses of WDs are in the range $0.5 - 0.6\ \mathrm{M}_\odot$, however, measurements of WDs in CVs are in the range $0.8 - 1.2\ \mathrm{M}_\odot$ (e.g., Warner 1973, Warner 1976b; Ritter 1976; Robinson 1976). This discrepancy has been explained as a selection effect where more massive WDs release more energy and hence, are easier to discover (Ritter and Burkert, 1986). However, Littlefair et al. (2008) and Savoury et al. (2011) measured WD masses for faint CVs yielding a mean value of $\sim 0.8\ \mathrm{M}_\odot$ while Zorotovic, Schreiber, and Gänsicke (2011) showed that the mass distribution of such systems should be biased towards low-mass WDs. Further studies of the WD mass distribution in CVs are needed to disentangle these disagreements.

---

[1] More generally, a gas comprised of Fermions, subatomic particles with half-integer intrinsic angular momentum.

1.2.1 The Spectral Energy Distribution of a White Dwarf

A WD is a close approximation to a black body. Being usually a hot object, its flux in bluer wavelengths is high and differences with a black body are due to a layer of hydrogen and/or helium atoms[2] on its surface.

When a photon emerges from the nucleus of a WD, it may have the right energy to move an electron from its quantum state to another. The energy of the photon is absorbed and therefore causes a deficit in the wavelength that corresponds to that energy, visible in the resulting spectrum. Thus, the Spectral Energy Distribution (SED) of a WD shows the Balmer lines caused by the hydrogen atoms (Hα, Hβ, Hγ and Hδ in Figure 1.1), and the more energetic Lyman lines in the ultraviolet and not in the range of the figure. The SED of a WD is also characterised by the width of the spectral lines. This is a product of the intense pressure to which the atmosphere of a WD is exposed, which causes perturbations in the energy of the electron orbits according to the *Heisenberg uncertainty principle*. These perturbations extend the wavelength range of the photons, making easier finding an atom to absorb them.

1.3 The Red Dwarf

The most common type of secondary in a CV is a red dwarf (RD). This is a small star, although much larger than the WD, and relatively cold, belonging to the main sequence, either of the late K or M spectral type. Most stars belong to these types, with mass and diameter values less than half of those of the Sun (down to 0.08 solar masses, when it becomes a BD) and a surface temperature of less than 4000 K. However, the part of the surface of the RD facing the WD can be heated up to 7500 K (Hellier, 2001). This causes the reflection effect, the RD absorbs the radiation from the WD and re-emits it. This can be seen from studying eclipsing CVs: near the eclipse, the heated face of the RD is not visible and the visible face is too weak causing an abrupt drop in flux. As the RD emerges from the eclipse, the heated surface becomes more visible by increasing its brightness, until it reaches its maximum when the entire heated surface is visible (see Figure 1.2).

---

[2] It usually contains other elements previously accreted.

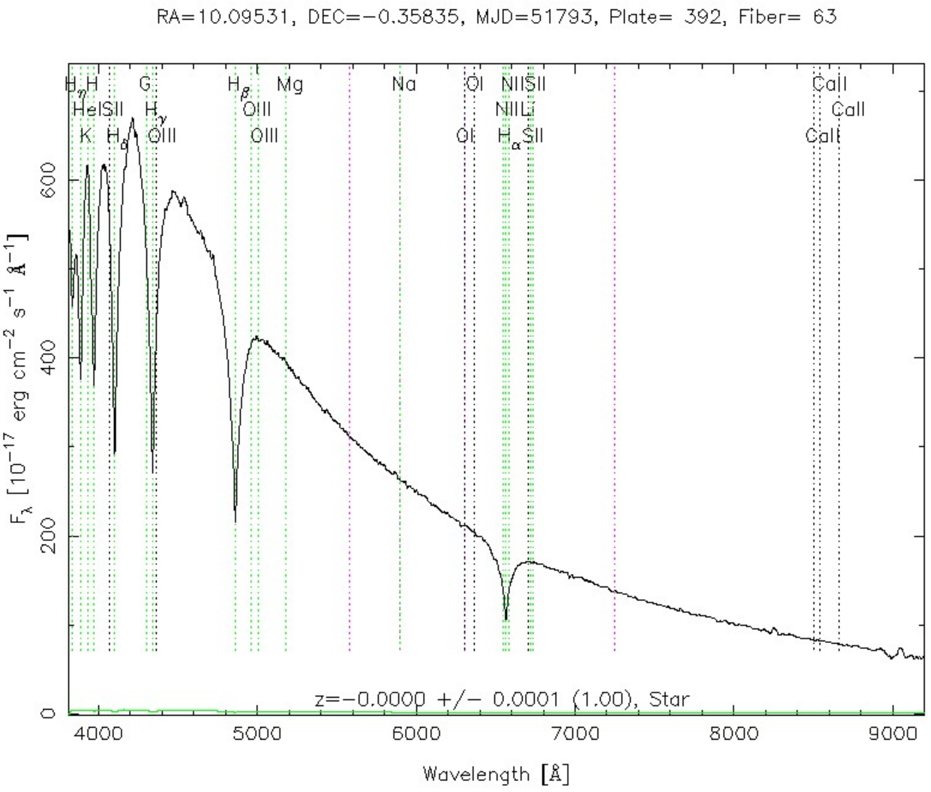

FIGURE 1.1: Spectral energy distribution of a White Dwarf. Source, SDSS-III

1.3.1 The SED of a Red Dwarf

The spectrum of the RD (Figure 1.3) has its maximum emission at red and infrared wavelengths. Because the surface of the RD is much larger than that of the WD, it is visible and even dominates the WD towards the red when it starts emitting. The low-energy bonds that bind atoms to molecules can survive in the low-temperature atmosphere of a RD. These molecules re-absorb the photons that emerge from the core, producing strong molecular lines in the spectrum. However, because molecules can rotate and vibrate in many more ways than the electrons in the atoms, the characteristics in the resulting spectrum are a complex set of broad dips.

1.4 The Roche geometry

Binary stars that are sufficiently separated from each other, as well as lone stars, tend to be spherical due to gravity. With a radius $\sim 1/50$ times the separation of both stars, this effect applies to the WD in CVs. However, the much larger but less massive RD is increasingly distorted by the gravity of its

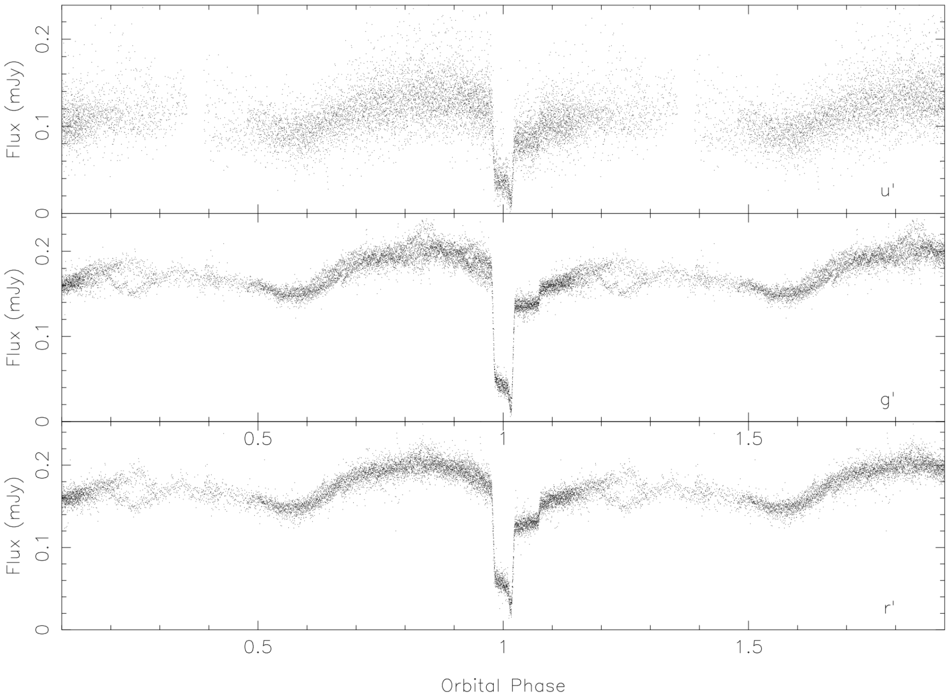

FIGURE 1.2: Orbital phases of the eclipsing CV SDSS J150722.30+523039.8 in SDSS u′-, g′- and r′-bands, respectively from top to bottom. Image reference: Littlefair et al. 2007

companion as the binary separation shrinks due to angular momentum loss during its evolution (discussed in Sections 1.1 and 2.1), to the point where the gravitational pull of the WD removes the outer layers of the RD (Roche lobe overflow).

The Roche geometry, which was first studied by Edourard Roche (from whom takes its name) in the nineteenth century, is a mathematical description of the interactions of stars and, where appropriate, as in the case of CVs, of the exchange of matter between the components of the binary. The Roche approach is simplified by assuming the orbits to be circular[3] and, for dynamical purposes, that the mass of the stars are concentrated at their centers. The surfaces over which the gravitational potential is constant, the equipotentials, when near the stellar centers, are circular, but at distances comparable to the binary separation are distorted towards the companion due to tidal forces (see Figure 1.4).

The gravitational potential Φ at a specific point given by the vector r, with stellar masses M_1 and M_2 located at r_1 and r_2 respectively, is given by

---

[3] This is accepted as a good approach since tidal effects tend to circularize the orbits on short timescales compared to the duration of mass transfer processes.

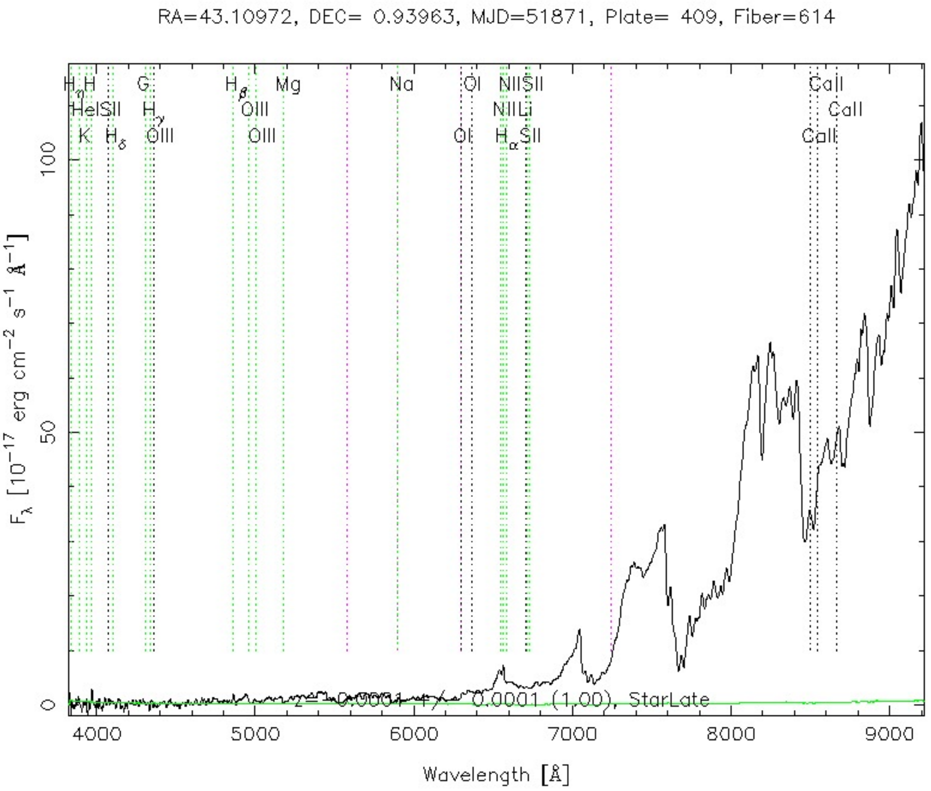

FIGURE 1.3: Spectral energy distribution of a RD. Source, SDSS-III

$$\Phi = -\frac{G\,M_1}{|r - r_1|} - \frac{G\,M_2}{|r - r_2|} - \frac{1}{2}\,(\omega \wedge r)^2 \tag{1.1}$$

where ω is the angular frequency of the orbit and $\frac{1}{2}\,(\omega \wedge r)^2$ accounts for the centrifugal force. Figure 1.4 shows the equipotentials for several values of Φ and the equipotential represented by the thickest line, number 3 in the figure, defines the Roche lobe of each star. The shape of the equipotentials depends on the mass ratio $q = \frac{M_2}{M_1}$ and on the binary separation a obtained from *Kepler's law* (see Equation 1.4 in next section). The equilibrium points of the Roche potential are called the Lagrangian points $L_1 - L_5$. The inner Lagrangian point, L_1, connects the regions dominated by the potential of the two components, the easiest path by which material can be transferred between the stars.

In addition, apart from q and a, the sizes of the Roche lobes and the distances from the L_1 point to the stars are needed to define the Roche geometry. Eggleton (1983) used the radius of a sphere with the same volume as the lobe as an approximation for the Roche lobe sizes, yielding a radius for the secondary Roche lobe of

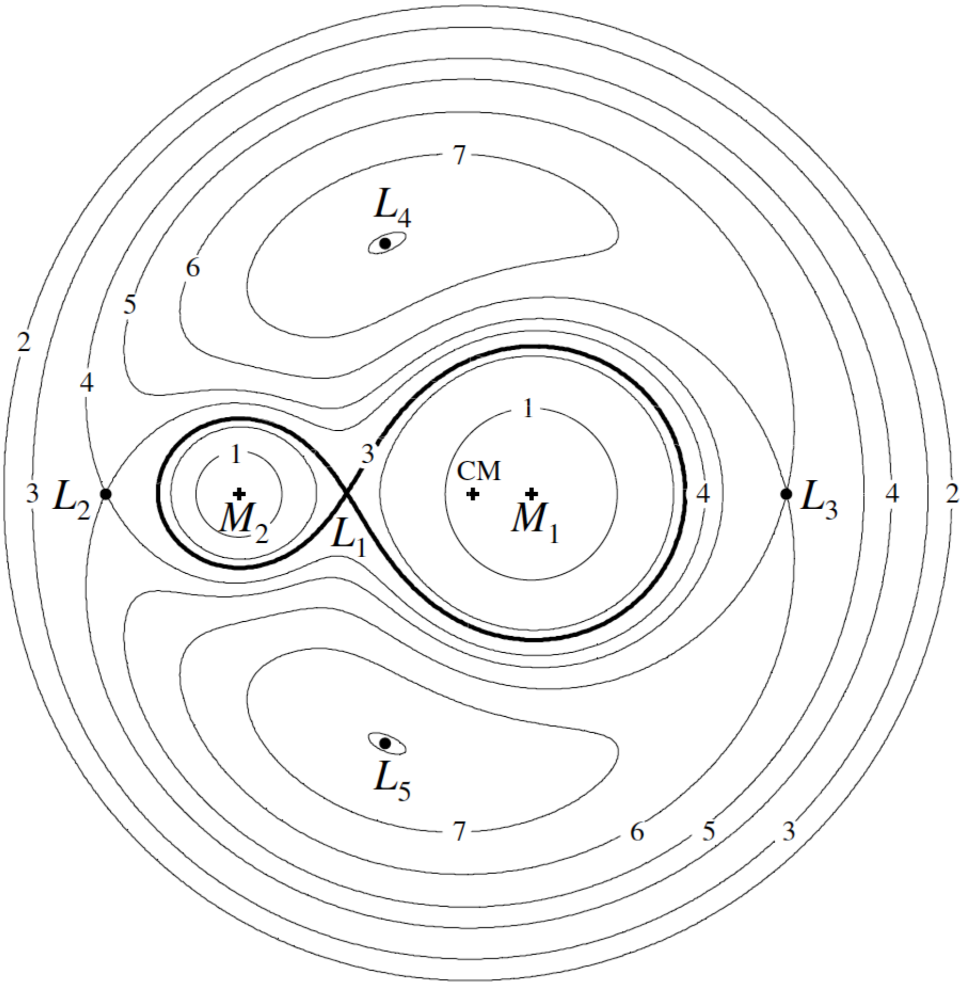

FIGURE 1.4: Contours of equal gravitational potencial, equipotentials, for a binary system with mass ratio $q = M_2/M_1 = 0.25$. Shown are the centre of mass (CM), the Lagrange points $L_1 - L_5$ and the equipotentials are labelled $1 - 7$ in order of increasing Φ. Figure taken from Frank, King, and Raine 2002.

$$R_2 = \frac{a\,0.49\,q^{2/3}}{0.6\,q^{2/3} + ln\,(1 + q^{1/3})} \tag{1.2}$$

and a circularization radius of

$$r_{circ} = a\,0.0859\,q^{-0.464} \tag{1.3}$$

for 0.05 < q < 1. Which is the minimum radius of the disc's outer edge.

It is assumed that the rotation of each star is synchrounous with the orbital motion[4]. In this case, the surfaces of the stars will lie on one of the

---

[4] Synchronism is usually a good approximation as tidal forces bring it on similar timescales to that for circularization of the orbit.

equipotentials. If the surface of the star fills its Roche lobe, mass transfer is triggered and the material then flows between the two stars. This is the case for the RD in CVs, which results in the formation of an accretion disc surrounding the WD, the most distinguishable feature of a CV.

1.5 Mass transfer

The secondary star fills its Roche lobe letting a thin stream of material flow into the WD through L_1. In turn, the pressure of the stellar atmosphere pushes this material into the Roche lobe of the WD. Due to the angular momentum from the orbit that this material has, it does not fall directly on the primary star, but instead comes out in jets which are orbiting perpendicular to the direction of the material, at more than 100 km/s. Therefore, the current rotates in an orbit around the WD instead of flowing directly towards it. At this point the gravitational attraction of the secondary becomes negligible and the movement of the stream of material is directed by the gravitational attraction of the primary and the material's own speed.

In this phase, the stream of material follows an apparently disordered flow, which after dissipating energy in the produced shocks, ends up adopting a circular orbit, minimizing the energy used. In order to ensure the same angular momentum as the outgoing material of L_1, it orbits at the radius necessary for it, the circularisation radius. However, within this formed ring of material, the parts closer to the primary star must orbit slightly faster and the external parts slightly slower. It can be inferred from *Kepler's law*

$$P_{orb}^2 = \frac{4\,\pi^2\,a^3}{G\,(M+m)} \tag{1.4}$$

For the circumference of the orbit, the orbital period is $P_{orb} = (2\pi r)/v$. Substituting on Equation 1.4, yields the *Keplerian velocity*

$$v = \sqrt{\frac{G\,M}{r}} \tag{1.5}$$

and therefore, the *Keplerian velocity* decreases as the radius of the orbit r is increased and vice-versa.

This causes friction that heats the gas causing irradiation of the energy outwards and the consequent displacement of some of the material into shorter orbits. The angular momentum is given by $J = mrv$, and substituting v for Equation 1.5

$$J = \sqrt{GM}\, m \,\sqrt{r} \tag{1.6}$$

which shows that angular momentum decreases as r increases. In order to preserve the angular momentum, some of the material must also be moved towards more distant orbits, spreading out all the material in the form of a disc. The disc continues to expand until its inner part either makes contact with the WD or is disrupted by the magnetic field of the WD if sufficiently strong.

The material moving through the disc towards larger radius transports angular momentum flows outwards, allowing the flow of material inwards. Thus, it accumulates onto the WD resulting in the consequent release of energy. At the outer edge of the disc, tidal interactions with the secondary star absorb the angular momentum and return it to the orbit of the secondary star, limiting the outward propagation of the disc. The disc is replaced by the mass transfer current of the secondary, which provides both fresh material and more angular momentum. As long as it flows, the disc is maintained.

1.5.1 The accretion disc

Accretion discs play an important role in various branches of astronomy. As in CVs, accretion discs form by redistributing angular momentum to allow gas clouds to collapse into stars or planets and are the material from which black holes are fed. The accretion discs around black holes at the center of Quasars (QSOs) are extremely bright and the furthest sources of light that we can see today. However, QSOs are too far away and star formation is often covered by the star-dust from which they are formed, making them difficult to study. The CVs are in a remarkable position because they are binaries, so masses can be derived and allow us to study accretion discs more clearly than with other objects, allowing to apply the acquired knowledge obtained in other phenomena.

The SED of an acretion disc

The spectra of accretion discs are more difficult to study and understand than the stellar spectra. In a CV, the temperature gradient ranges from $\sim$ 5000 K in the outer parts to $\sim$ 30000 K in their inner regions, and therefore, it is not appropriate to treat them as a single entity. Instead, the disc is divided into annuli, interpreted as individual black bodies at the corresponding temperature and then added together by weighting them by their surface. The resulting spectrum is an approximation of the continuum but that cannot reproduce the spectral lines. An alternative is to assume that each annulus emits the spectrum corresponding to a star of the same temperature and add them up (*Chromospherically Active Binary Stars* 1994) as in the previous approach. Although this approach adds spectral lines, these are in absorption while those of the discs are usually in emission.

Emission and absorption lines

When an atom absorbs a photon and causes an electron to jump to another level of energy, it is very likely to return to its previous level by emitting an exact replica of the incoming photon. If a photon tries to pass through an optically thick material, it will travel a short distance before interacting with the surrounding atoms. This distance is known as the *mean free path*. When this distance is short, the photon needs many interactions before escaping from the material. The mean free path determines the *optical depth*, i.e. the distance (on average) that a photon penetrates before it is absorbed. Similarly, the photons emerging from the optically thick material come from a depth equal to their mean free path. At uniform temperature (in local thermodynamic equilibrium), the depth from which they emerge is the same as the depth of penetration. The number of absorptions is equal to the number of emissions, they cancel each other out and no spectral lines are seen, therefore the spectrum emitted is that of a black body.

However, photons at wavelengths of a spectral line are more likely to interact with the surrounding atoms. Therefore their mean free path and hence their optical depth are shorter. In the case of stars and discs there is no thermodynamic equilibrium because they are hotter in their inner layers and colder in their outer ones. Photons with shorter main free path emerge from colder areas, while the rest emerge from hotter parts and their radiations are therefore brighter. The radiation on the lines, which comes from the colder surface, is weaker and they appear as absorption lines.

In optically thin conditions, the emitted photons emerge without interactions. However, there are still two processes that can cause alterations in the energetic orbits. The collisions of atoms and the photo-ionisation due to the radiation on the material and which expels the electrons from the atoms. These processes produce photon emission which, in the absence of absorption, register spectral emission lines.

Accretion discs show emission lines on some occasions and absorption lines on others, indicating changes of state between optically thick and optically thin conditions. Sometimes they even show absorption and emission characteristics simultaneously. This can occur if an optically thick disc is surrounded by a hot, optically thin corona. Therefore, due to all these variables, it is difficult to model accretion discs and, in any case, a model of the accretion disc must take into consideration the pressure and density in the different parts of the disc, which in turn depends on the gravity of the WD, the generation of radiation by viscous processes, the propagation of radiation through the disc material and other additional complications such as gas turbulence and energy transport by convection.

1.5.2 The bright spot

Once the disc is formed, the stream of material from the secondary star hits it, forming the bright spot. The stream of material encounters the disc moving in its circular orbit. The consequences of this impact are very complex and not completely understood but some simulations suggest that the stream makes a hole in the disc that is slowly absorbed by it (Armitage and Livio 1996, Speith and Kunze 2002). The irradiation caused by the bright spot can reach 30% of the total brightness of the system.

Through the study of light-curves of eclipsing systems, we can determine the size of the bright spot (see Figure 1.5). The eclipses of the WD and the bright spot are comparable or even larger for the bright spot. This indicates that the bright spot is similar in size or even larger than the WD. In addition, the radius of the disc can be determined using the phase in which the bright spot eclipse occurs. Thus, the smaller discs fill about half of the WD's Roche lobe and the larger discs fill $\sim 80 - 90\%$ of its Roche lobe.

1.6 Doppler effect

The Doppler effect is caused by the movement of the emitter with respect to our point of view. When a source of photons moves towards us, the wavelength is shortened because the distance travelled in that interval has to be subtracted from the distance between the wavelength peaks[5]. This produces

---

[5] For waves which do not require a medium, such as electromagnetic waves or gravitational waves, Doppler effect considers time dilation effect of special relativity and do not involve the medium of propagation as is the case for waves that propagate in a medium, such as sound waves.

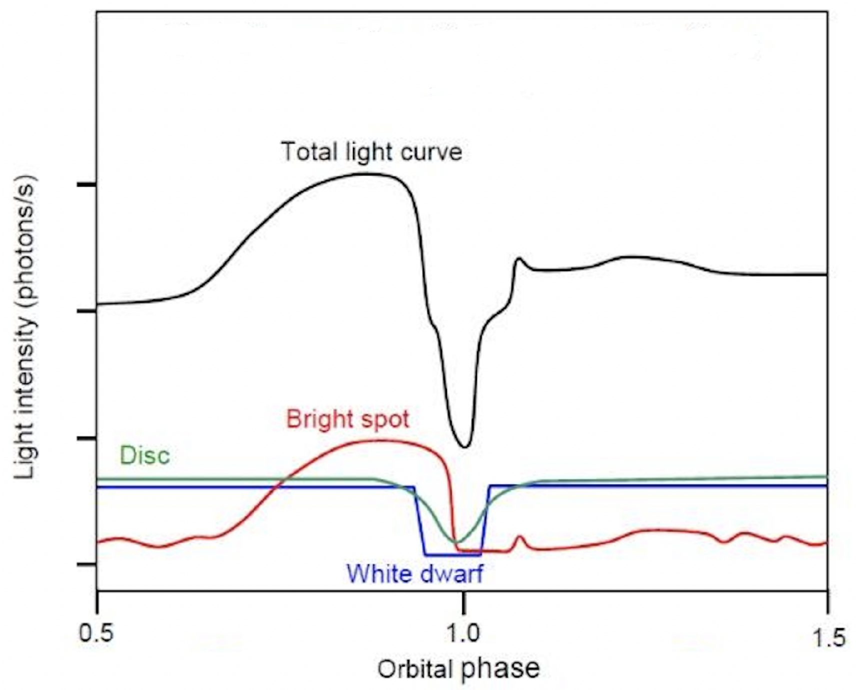

FIGURE 1.5: The light-curve of Z Cha, an eclipsing accretion disc binary. At the bottom of the figure, the orbital phases are shown and in different colours the contributions of its components. The WD eclipse causes a very abrupt drop in brightness, the one of the disc is smoother. The bright spot however is out of phase with the latter two and also forms a hump before its eclipse itself.

apparent wavelength shifts towards more energetic frequencies or towards the blue. The redshift is the equivalent of the photon emitter moving away from us. Both effects are perceptible in an accretion disc with a certain inclination, the part of the disc which moves away from us suffers a redshift and the part which approaches, a blueshift. The amount of redshift or blueshift is directly proportional to the velocity at which the material moves along the line of sight

$$1 + z = (1 + \frac{v}{c})\,\gamma \tag{1.7}$$

where z is the redshift, v the velocity, c the speed of light and γ the Lorentz factor.

Depending on the phase of a CV, its different parts will cause a red or blue shift. Thus, if we measure the Doppler effect caused by one of its parts during the whole orbital cycle, the result will be a sinusoid for circular orbits, the S-wave. All emission sources moving with the system form an S-wave but the maximum red or blue shift of an S-wave occurs with the bright spot at one extreme from our viewpoint. This instant reflects the total velocity of the material for an edge-on system. More generally, for systems with an inclination i, the movement v in the binary plane can be resolved into a $v \cdot sin(i)$ along our line of sight and a component perpendicular to it. The amplitude of the S-wave from a bright spot does not reflect the speed of the accretion current in free fall, nor the Keplerian speed of the disc material it has hit, but a speed halfway between the two.

A disc can be considered as a collection of small regions that emit S-waves of the same radial velocity amplitude and the profile, a sum of them weighted by the area they are comprised of. The result is a double peak profile displaced from the center of the line by a typical velocity of the outer disc (see Figure 1.6). The disc is centered on the WD, and thus follows its movement around the common center of mass. This means that the whole double-peak profile of the disc executes an S-wave in synchrony with the WD.

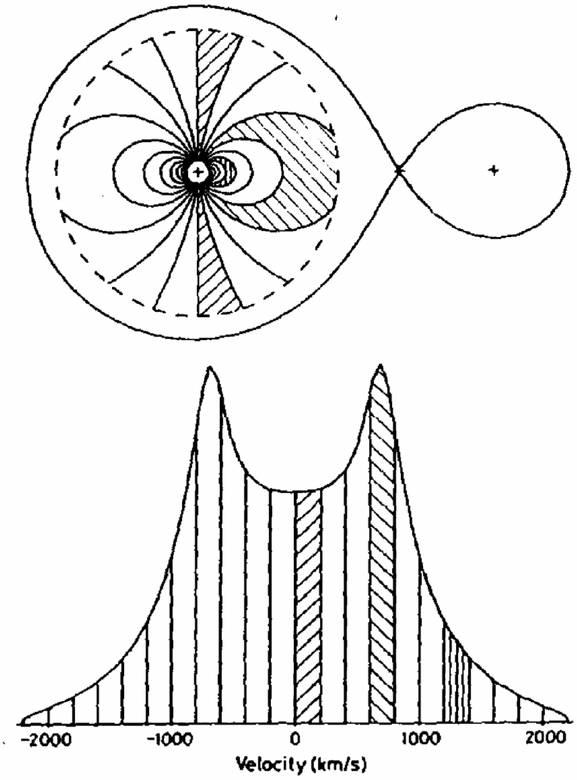

FIGURE 1.6: At the top, a map of a CV as seen from above, in plane view (inclination = 0); At the bottom, a double-peaked spectral line, the height of which is the light intensity and the horizontal axis shows velocity of the material emitting the corresponding part of the line. The shaded regions on the spectral line correspond to the shaded regions of the disc. The higher velocities are seen in the innermost regions of the disc, which equate to the wings of the spectral line, when that part of the disc is moving along our line of sight. Negative velocities indicate motion away from the observer, positive velocities towards the observer. Although the inner parts of the disc are hotter and brighter, the outer regions have a much larger surface area and so contribute more to the brightness of the whole image. Thus, the faster moving inner regions emits lower total light intensities and so the intensity drops off at the wings of the line. Figure taken from Hellier (2001).

Chapter 2

CV evolution

Stars form from clouds of interstellar dust and gas that collapse under their own gravity. Depending on the mass contained in these clouds, gravitationally bound young stars will form in binaries, triples, binary pairs or other combinations, and only in a low percentage, single stars. In this context, the stars most likely to become CVs are binary systems in which one component has a lower mass than the Sun (which will become the secondary star), while the other one is more massive (later becoming the primary or DW). In addition, they must be separated by a few hundred solar radii and orbital periods ~ 10 years. The higher mass in the core of the future WD translates into more energetic nuclear reactions due to its higher pressure and temperature. It results in a faster evolution with respect to its companion and will eventually expand to become a red giant. As explained in section 1.2, WDs form as the core of this red giant, whose outer layers extend to ~ 100 solar radii. At this stage, the red giant fills its Roche lobe, transferring its outer layers to its less evolved and less massive companion. This configuration is the opposite of a CV, where the less massive star fills its Roche lobe and is the one transfering mass to the more massive WD.

This situation is not stable. The more massive star, which is nearer to the binary center of mass, is the one transferring the material. Therefore, the material transferred to its companion is now at a larger distance from the center of mass. This increases the angular momentum of that material, and to preserve the angular momentum of the whole system, the stellar distance must be decreased. This decrease in stellar separation causes a decrease in both Roche lobes volumes which get even more overloaded and therefore, mass transfer increases. This can be derived from the basic formula $J = mrv$ where the velocity v is perpendicular to the lever arm r, and using *Kepler's law* (Equation 1.4) we obtain

$$J = M_1\, M_2\, (\frac{Ga}{M})^{1/2} \tag{2.1}$$

where $M = M_1 + M_2$. If the total mass is conserved ($\dot{M} = 0$) and taking natural logs and differntiating with respect to time then gives

$$\frac{\dot{a}}{a} = 2\frac{\dot{J}}{J} + 2\frac{-\dot{M}_2}{M_2} - (1 - \frac{M_2}{M_1}) \tag{2.2}$$

Therefore, if angular momentum is also conserved ($\dot{J} = 0$), transfer from the secondary ($\dot{M}_2 < 0$) leads to increasing a, provided $M_2 < M_1$.

Thus, both stars end up with their overloaded Roche lobes resulting in a 'common envelope' surrounding the two stars. The nascent CV is effectively orbiting inside a red giant.

The drag of the orbiting stars drains their orbital energy, causing them to spiral inwards. Their separation is reduced from $\sim$ 100 R$\odot$ to $\sim$ 1 R$\odot$ in about 1000 years. The energy extracted from the binary orbit pushes the envelope into interstellar space, forming a 'planetary nebula'.

The end result is a WD-RD binary that continue to get closer due to gravitational and magnetic braking. The period in which the binary becomes a CV depends on the size of the secondary when it emerges from the common envelope. In the case that it does not fill its Roche lobe, there is no mass transfer and so it will not yet be a CV. These systems are known as pre-Cataclysmic Variable[1]. Nonetheless, magnetic braking will continue to function as a mechanism for angular momentum loss until the RD makes contact with its Roche lobe and initiates mass transfer, a scenario that will likely occur at shorter orbital periods.

2.1 Mass transfer mechanisms

Differently from the Pre-CV phase explained in the previous Section 2, the mass transfer in CVs occurs from the less evolved and less massive secondary to the primary WD. Assuming that the angular momentum of the system is maintained, the transferred material goes from the secondary to the more massive primary and therefore, from a larger distance to the center of masses to a shorter one. This causes a loss in angular momentum which is offset by widening the binary separation and, in turn, causes the secondary to separate from its Roche lobe, halting the mass transfer. To keep mass transfer stable, the system must lose angular momentum progressively by another mechanism. This would shrink the orbit and the Roche lobe of the secondary, allowing the resulting excess of material to be transferred (see Equations 2.1

---

[1] If they can reach contact within Hubble time.

and 2.2). There are two main mechanisms by which CVs lose angular momentum: gravitational radiation and magnetic braking.

2.1.1 Gravitational radiation

The repetitive orbit of two stars causes a systematic deformation of space that ripples outwards in a periodic wave. This wave is called gravitational radiation. The energy to generate this wave is extracted from the binary orbit, which causes a loss of angular momentum of the system and a slow spiral inwards.

In most binaries, the effects of this gravitational radiation are negligible because they have wide orbits and long orbital periods compared to the masses involved. However, as the binaries orbit closely, their orbital period speeds up and the gravitational radiation increases. From the theory of general relativity, the gravitational radiation of a CV and in turn, the mass transfer rate, can be computed. For a CV with a period of 2 h, the gravitational radiation causes a mass transfer rate of $\sim 10^{13}\,\mathrm{kg\,s^{-1}}$ ($\sim 10^{-10}\,\mathrm{M_\odot\ yr^{-1}}$, Iben, Fujimoto, and MacDonald 1992).

2.1.2 Magnetic braking

The combination of the stellar wind caused by the secondary with its own magnetic field forms the theory of magnetic braking. The stellar wind is plasma expelled from a star, and is expected to be expelled by the secondary in the CVs. Being a late-type star, it is also expected to have a magnetic field. Moreover, it seems that the rotation speed of a star is proportional to the strength of such magnetic field. Therefore, RDs in CVs should have very strong magnetic fields since they have rotation periods equal to their orbital periods, that is, a few hours. The magnetic braking theory says that electrically charged stellar wind particles cannot cross the magnetic field and instead flow along the magnetic field lines. Therefore, such particles co-rotate with the RD and are accelerated until they get ejected into interstellar space at high speeds. These particles take with them part of the angular momentum of the system, which, not being able to be transferred to the rotational slowdown of the secondary one since it is tidally locked, is transferred to the orbital period, which is reduced accordingly.

Knowing the distance to the system and the mass of the WD, it is possible to deduce the speed at which the material accumulates into the WD (and therefore the mass transfer rate) from the increase in luminosity with respect to that corresponding to such a system. In many cases, the distances are uncertain and, in addition, much of this luminosity occurs in ranges of the ultraviolet spectrum that are very difficult to measure, so these measurements can lead to large errors. However, some estimates determine a mass transfer rate $\dot{M} \sim 10^{14}\,\mathrm{kg\,s^{-1}} \sim 10^{-9}\,\mathrm{M}\odot\ \mathrm{yr}^{-1}$ (Iben, Fujimoto, and MacDonald, 1992).

2.2 The orbital period

By studying the population of CVs, we can try to understand their evolution. As CV lifecycles are several tens of millions of years long, we study the population of CVs in the hope of finding distributed systems in all their stages. Figure 2.1 shows a compilation of CVs from Downes et al. (2001) and Ritter and Kolb (2003) catalogues, for which their orbital period is known, 1544 CVs in total.

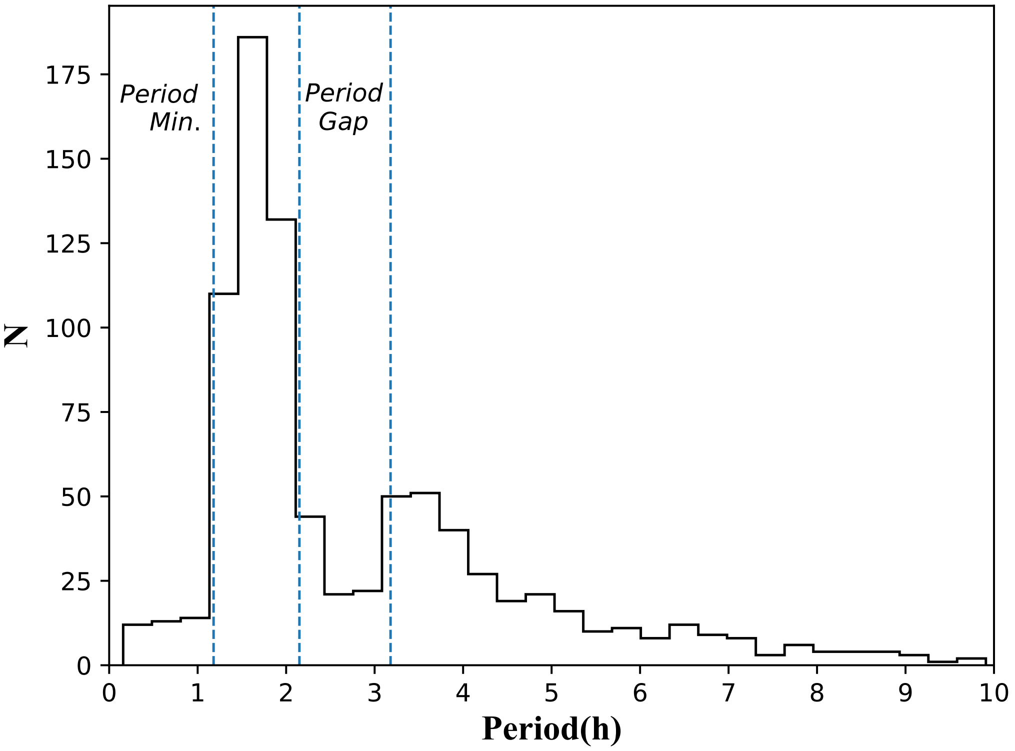

FIGURE 2.1: The distribution of Cataclysmic Variable orbital periods.

2.2.1 The upper limit of the orbital period

Figure 2.1 shows a decrease in systems at orbital periods longer than 6 – 7 h. The upper limit of the orbital period is marked by the mass of the Secondary. A CV is constituted by a WD whose mass limit is the Chandrasekhar limit, 1.4 $M_\odot$ and, as mentioned at the beginning of this chapter, 2, the secondary must be less massive than the WD, therefore its mass limit is the same. As the orbital period gets longer, the secondary must be larger and therefore more massive in order to fill its Roche lobe. For a secondary mass equal to the Chandrasekhar limit, the period corresponds to $\sim$ 12 h. Nonetheless, a decrease of systems is noticeable from $\sim$ 6 h upwards. Some systems, however, have longer orbital periods. These are explained because they are evolved from the Main Sequence, making them larger (although not more massive) and filling their Roche lobe at longer periods.

2.2.2 The period gap

From the birth of a CV, magnetic braking progressively shrinks the orbit at mass transfer rates $\dot{M} \sim 10^{-9} - 10^{-8}\ M_\odot\,\mathrm{yr}^{-1}$. However, when arriving at orbital periods $\sim$ 3 h, an abrupt fall in the number of systems is observed which lasts up to $\sim$ 2 h, the period gap. Below 2 h, the mass transfer rates are reduced considerably to those of gravitational radiation $\dot{M} \sim 10^{-10}\ M_\odot\,\mathrm{yr}^{-1}$.

Standard theory suggests that magnetic braking is switched off when a CV has evolved down to 3 h. At periods about 3 h, the RD reaches the appropriate mass at which convective motions in a RD circulate all over the star, removing the non-convective core present at higher masses, thus resulting in the shutdown of the magnetic dynamo. The secondary is also out of equilibrium due to the mass transfer processes.

As the RD loses its outer layers, the pressure on the core and thermonuclear reactions decrease. Gravity is now stronger than thermonuclear reactions and the star therefore contracts. But it does so at the thermal timescale, if this timescale is longer than the mass transfer rate, it does not have time to contract and finds itself with a very large radius for its mass. When the magnetic braking is turned off, the mass transfer is halted and the star adjusts to its equilibrium size and detaches from its Roche lobe. To make contact with its Roche lobe again, the orbit must decrease. Gravitational radiation comes into play by reducing the orbit up until a period of $\sim$ 2 h, the RD makes contact with its Roche lobe and the mass transfer is re-established, albeit at a lower rate.

Some systems, however, are found in the period gap. This might occur if a CV is born at a period of 2 – 3 h. In these cases the secondary has not been taken out of its equilibrium because there has been no mass transfer. It is large enough to make contact with its Roche lobe allowing mass transfer. The period gap is also populated by magnetic CVs, whose WDs' magnetic fields alter their evolution.

2.2.3 The period minimum

The CV emerges from the period gap and its secondary continues to transfer mass to the WD. When the mass of the RD is low enough, a degenerative process begins, as with WDs. At this stage, the gravitational force is compensated by the Fermi gas pressure. This produces that as the secondary continues to lose mass, it increases in size. In normal conditions, RD transfers mass, the orbital distance increases and the Roche lobe separates consequently while the size of the secondary is slightly reduced. But simultaneously the angular momentum loss reduces the binary separation, allowing it to maintain contact with its Roche lobe, mass transfer continues steadily and the system evolves to shorter periods. The process is similar with a degenerated secondary, but instead of reducing the size of the RD, it increases without losing contact with its Roche lobe. The period will be slightly longer and appropriate to the new size of the RD, and so the system evolves to longer periods. Simulations that take into account the mass-radius ratio of the secondary as it degenerates show that the CVs evolve from longer periods to the minimum period around $\sim$ 72 min. and then evolve to longer ones.

After going through the period minimum, the mass of the secondary is $\sim 0.06\mathrm{M}_{\odot}$ (Knigge, 2006) and continues to decrease as the orbital separation continues to increase.

There is one group that reaches periods below the period minimum, AM CVn stars. These systems have secondary systems comprised mainly of helium. Helium is heavier than hydrogen (dominant in standard CVs), these stars are more compact and need shorter orbital periods to make contact with their Roche lobe. The reduced orbits of these systems enhance gravitational radiation causing greater mass transfer. As with hydrogen CVs, the secondary ones lose mass and degenerate to a (different) period minimum. The existence of AM CVn requires very particular conditions and are quite rare.

Chapter 3

CV classification

The most characteristic phenomenon of many of the CVs and from which they get their name is the outburst. The most energetic ones are nova outbursts, their intensity increases up to 19 magnitudes in the interval of days, to gradually fade away later during months or years. There is no known recurrence for novas although, there are theoretical reasons to think that these outbursts repeat in the lapse of $10^4 - 10^5$ years.

Less dramatic are those known as Dwarf Novae outbursts, the intensity of many CVs increases by several magnitudes in time frames of the order of 1 day, to progressively fade away in the time-space of a few weeks. These outbursts, produced by thermally unstable accretion discs, do show a recurrence in which, after several months of quiescence, the outburst is repeated[1]. In contrast, Nova-like stars are high mass transfer systems with stable accretion discs which has never shown an outburst.

Another class consists of systems whose white dwarfs possess a magnetic field, these are known as magnetic CVs. These systems do not allow the formation of the accretion disc because the material coming from the secondary is intercepted by this magnetic field of the WD. A type of intermediate systems, whose WD's magnetic fields are not sufficient to override the accretion disc completely, are the so-called intermediate polar systems.

CVs have historically been classified according to the long-term optical light curves features which, in turn, are defined by the intensity and frequency of their outbursts, by its magnetic activity and other properties of its components. In this chapter we will go through the main types of CVs and their distinctive properties.

---

[1] Depends on the system, some have outbursts every few days.

3.1 Novae. Classical and recurrent novae

A CV that has shown only one outburst is known as a classical nova[2], and systems that have shown multiple outbursts are known as recurrent novas (RNe). These systems show outburst of 7 – 11 magnitudes.

The amplitude of the outburst of a classical novae is the largest of all CVs. These outbursts are caused by a nuclear fusion of hydrogen-rich material accumulated on the surface of the WD. This material, coming from the secondary, is subject to high pressures due to the gravitational field of the WD and its temperature also increases as it accumulates. When pressure and temperature reach the critical level of the hydrogen nuclear fusion, a thermonuclear runaway explosion occurs, expelling at least, a big proportion of this material into the interstellar space.

RNe, which have larger mass transfer rates, harbour a very massive WD, hence the thermonuclear explosion can be triggered with the accretion of less material and, therefore, on a shorter time scale. Despite being very few, there are 3 subgroups within the RNe (Anupama, 2008).

- Oph, T. This group is comprised of systems with long orbital periods ($>$ 100 days) with red giants as secondaries and whose eruptions are the result of interactions with the wind of the red giant.
- U Sco. With orbital periods of around ~ 1 day and evolved secondary, they have rapid eruptions of up to 2 magnitudes which decrease rapidly within a few days.
- T Pyx. Systems with short periods ($P_{orb} < 3\,\mathrm{h}$) with high mass transfer rates. T Pyx and IM Nor are the references of this group.

Novas concentrate at orbital periods typical of high mass transfer rates (Figure 3.1). Nonetheless, several systems are found within the period gap and below it.

3.2 Dwarf Novae

Dwarf Novae (DNe) outbursts increase the brightness of the system between 2 and 6 magnitudes. They are more or less regular, but their duration and

---

[2] Strictly speaking, Classical novae is not a CV subtype, but since they show different characteristics from the other CV subtypes is treated separately.

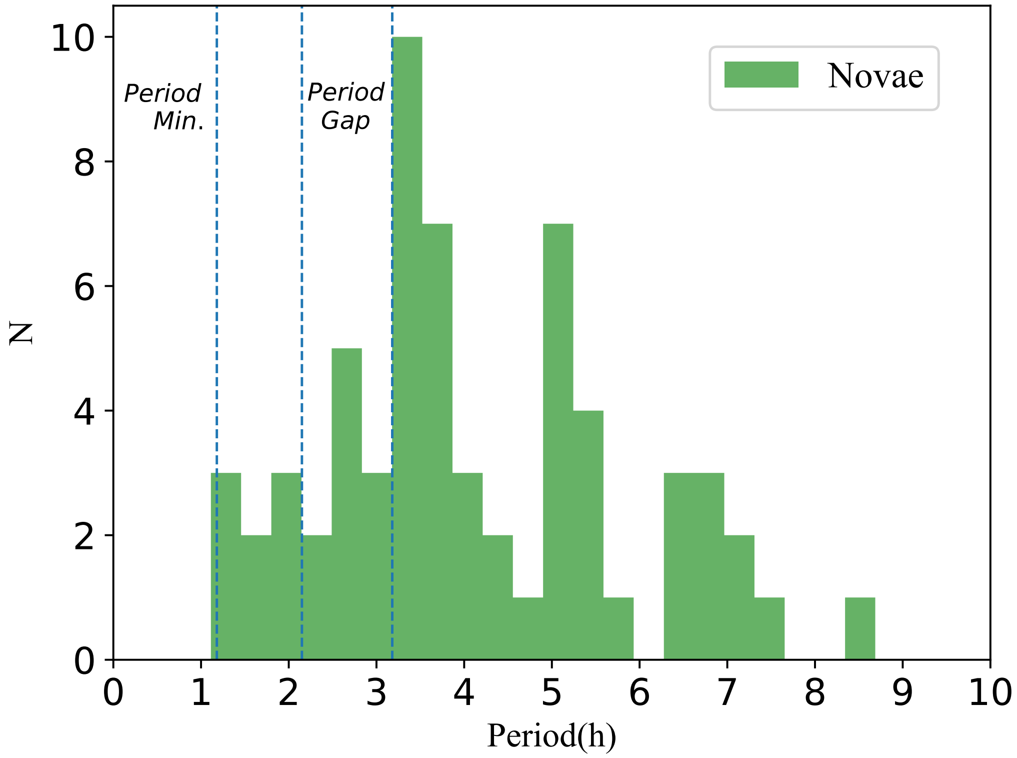

FIGURE 3.1: Orbital period distribution of Novae. Although there is an accumulation just above the period gap, a non-negligible amount of novas are found withing and below the period gap.

recurrence are variable[3]. The theory proposed by Osaki (1974) and widely accepted, says that these outbursts are caused by instabilities in the accretion disc. It proposes that if the material is transferred from the secondary during quiescence at a constant rate and if this rate is higher than the one that can be carried across the disc by viscous interactions, then the material is stored in the outer parts of the disc. If this material exceeds some critical point, it causes instabilities and boosts viscosity. Initially, the gas flowing from the secondary forms a thin accretion disc around the WD. As more gas is accreted, viscous drag will cause frictional heating of the material until it reaches the hydrogen photo-ionisation point. The increase in viscosity significantly increases the angular momentum transfer by spreading the excess material to the WD and outwards. The increase in accretion onto the WD causes an increase in brightness as the material drains the disc and allows it to return to a quiescence, low-viscosity state and start a new cycle.

---

[3] Different from system to system but quite regular for a given binary.

In general terms, DNe outbursts have very sharp rises and slower declines. However, some are longer than others and sometimes the outburst shape is more symmetrical with slower rises, see Figure 3.2. The reasons for such irregularities are related with the radius at which the outburst is triggered and the distribution of the remaining material left by the previous one.

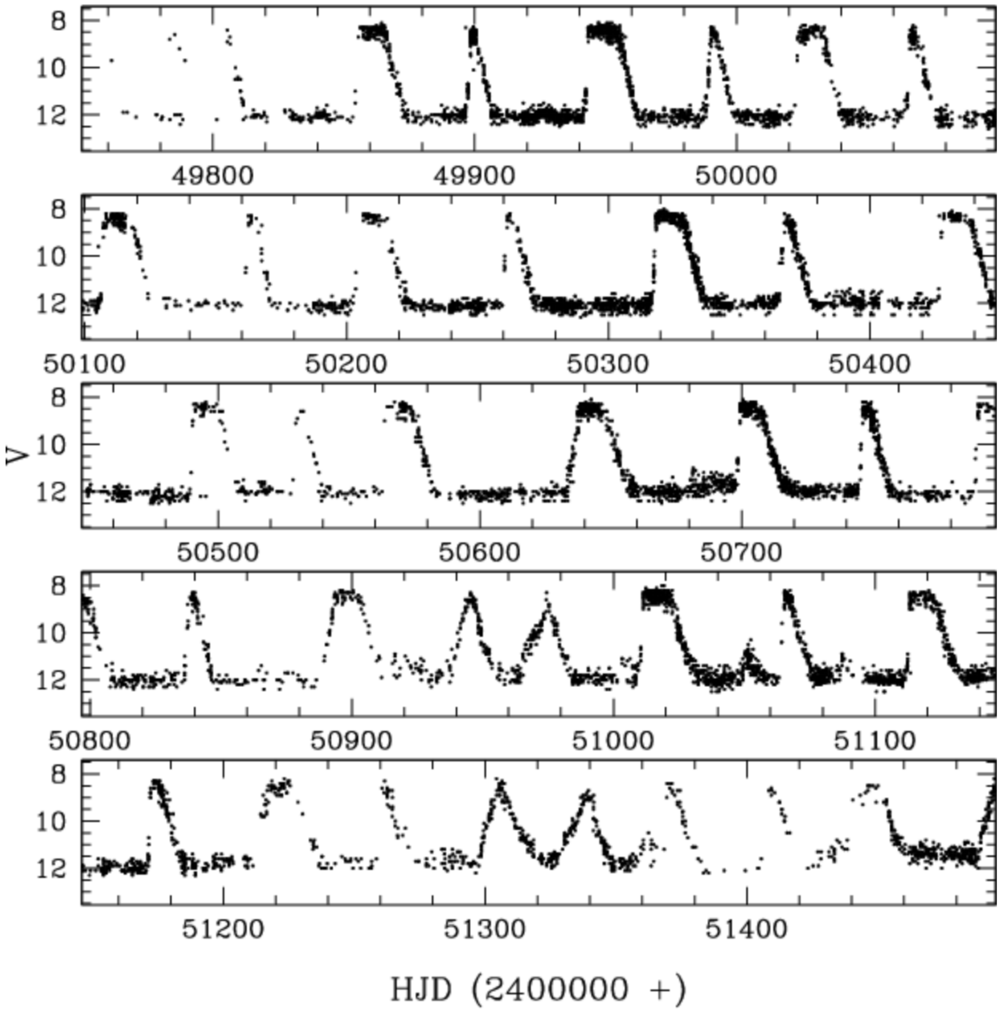

FIGURE 3.2: SS Cyg's lightcurve showing different outburst shapes. The duration of some of them is longer (∼ 10 days), they showing a plateau at the top. The outburst rises are either rapid (∼ 2 days) or slow (∼ 8 days); but the declines all take ∼ 8 days. Data compilation by the AAVSO.

Dwarf Novae are concentrated below the period gap (Figure 3.3). Gravitational radiation is the main mechanism driving angular momentum loss in Dwarf Novae which are also the most populated CV subtype.

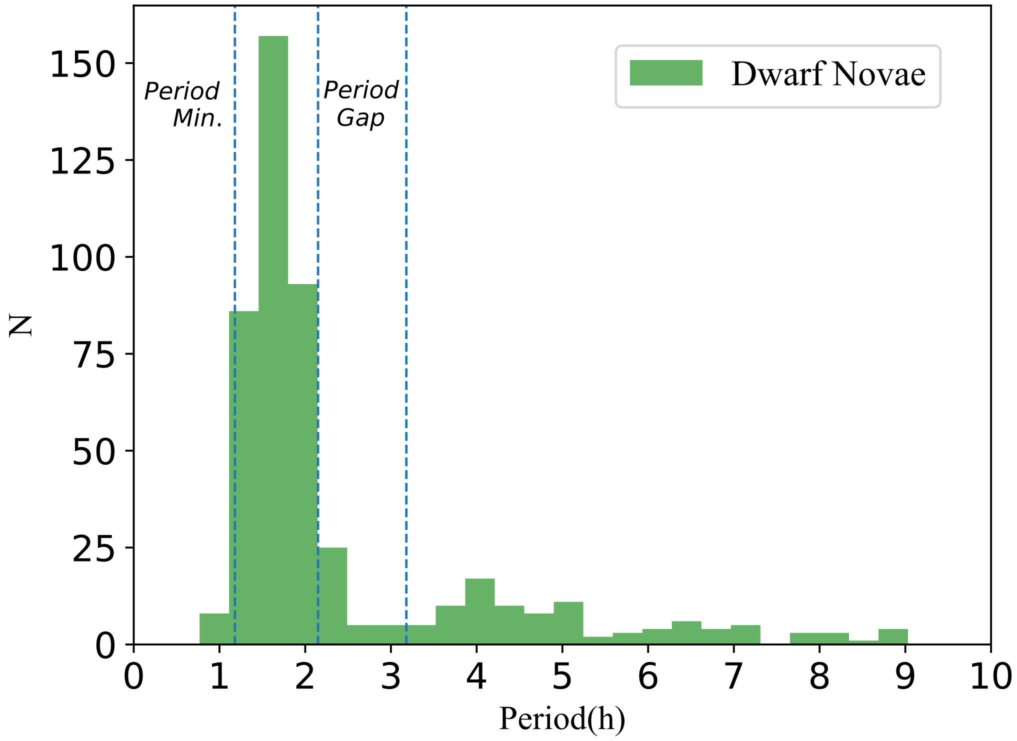

FIGURE 3.3: Orbital period distribution of Dwarf Novae. With orbital periods in the action range of gravitational radiation they are accumulated below the period gap.

3.3 Nova-like

The Nova-like variables (NLs) are CVs that do not exhibit any outbursts. Instability in the disc occurs when the mass accumulated reaches a certain temperature. If the flow is low enough to ionise the hydrogen, the disc would remain stable and there would be no outburst. No such system is known, perhaps because they are too weak objects to be detected. On the other hand, if the mass transfer rate is so high that it constantly maintains the instabilities in the disc, the disc will always be in an outburst state. These types of CVs are known as Novalikes (NL), CVs that have never shown any outburst and with a sufficient mass transfer rate to keep the disc on the hot side of instability. The higher mass transfer rate in NLs releases greater amounts of energy when accumulated in the WD and therefore, NLs are inherently brighter than DNe discs in quiescence.

Nova-likes are dominated by a high mass-transfer accretion disc, that usually outshines the WD and the secondary star. Thus, as expected from high mass transfer rates driven by magnetic braking mechanisms, Novalikes appear mainly above the period gap in the CV orbital period distribution,

Figure 3.4.

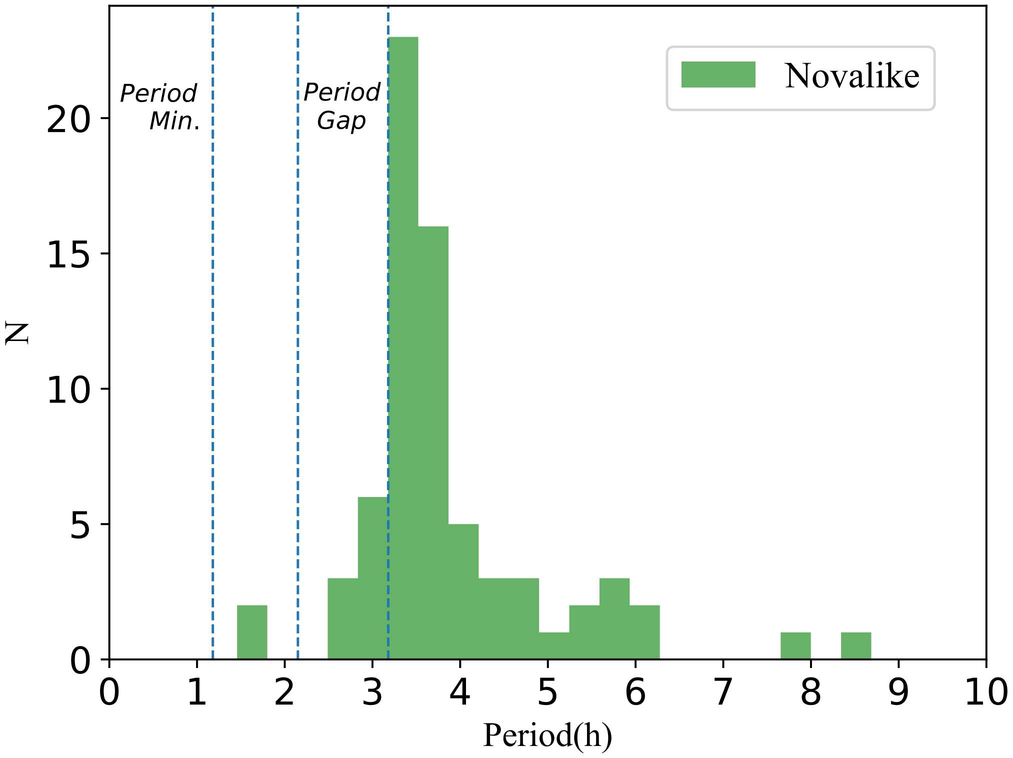

FIGURE 3.4: Nova-likes orbital period distribution. Most of them above the period gap, in accordance with their typical high mass trasnfer rates.

3.4 Magnetic CVs

When WDs in CVs have a sufficiently strong magnetic field (>10 MG), they are classified as Polar, magnetic or AM Her stars. A magnetic field alters the motion of charged particles, and in turn, charged particles in motion generate magnetic fields. Therefore, the interactions between the magnetic field of a WD and the ionised gas of the matter transferred by the secondary cause a complex field structure. Initially, matter is far from the magnetic field of the WD and its kinetic energy is dominant, therefore the field does not cause significant alterations in matter. As matter approaches the magnetic field, the interaction matter-field is much stronger, the field lines remain firm and the particles have no choice but to flow along them finally accreting directly onto the magnetic poles of the WD. That is, the behaviour of a magnetic CV can be broken down into two parts, a zone outside the range of the magnetic field that behaves as if it did not exist, and the zone dominated by the magnetic field (magnetosphere) where the behaviour of the magnetic CV is almost entirely determined by it.

Just before the material enters the magnetosphere, where it will be forced to corrotate with the WD, the material is governed by a circular Keplerian motion. The WD tends to readjust so that the circular motion inside the magnetosphere is equal to that of the material just outside it. This adjustment occurs in relatively long timescales so changes in mass transfer rates may alter the whole behaviour. Assuming stable mass transfer rates, it causes a slowing down of the WD rotation. Therefore, WDs with weak magnetic fields rotate faster than those with a larger magnetic field. Thus, the magnetic field strength, spin rate and mass transfer rate determine the subclass of magnetic cataclysmic variables.

Magnetic CVs are mainly located below the period gap as seen in Figure 3.5. Magnetic CVs need a strong magnetic field or relatively short orbital period to not forming a disc which is in accordance with their location in the orbital period distribution histogram.

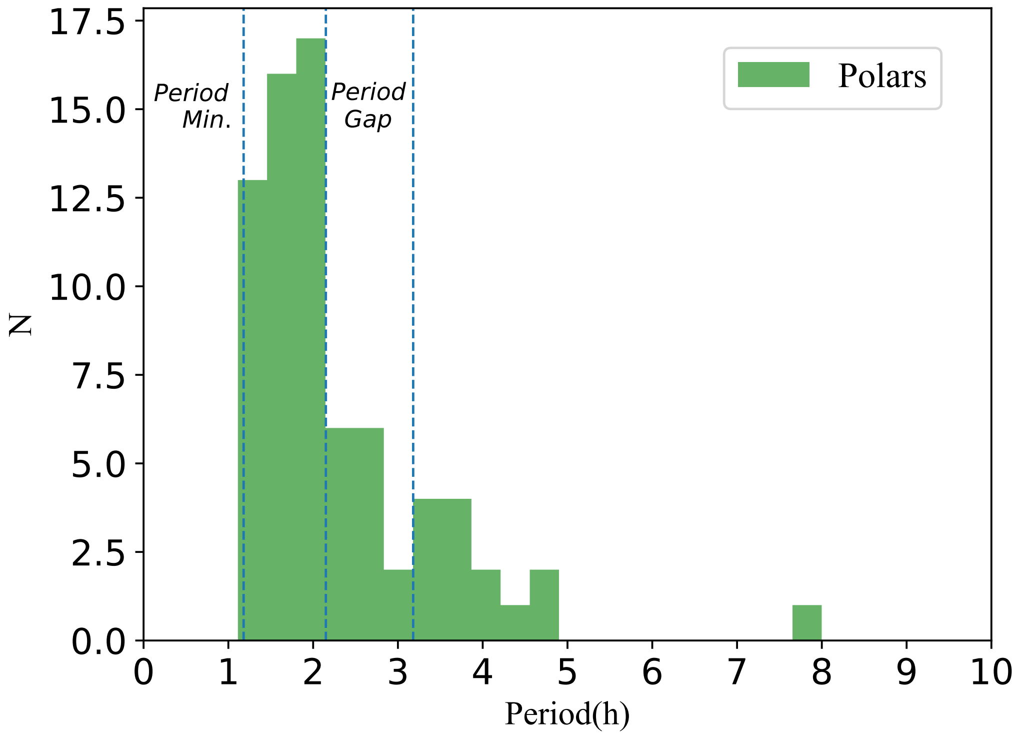

FIGURE 3.5: Orbital period distribution for Magnetic CVs.

3.5 Intermediate Polars

At an intermediate point between the systems whose magnetic fields are so weak that they can be ignored and those of the magnetic CVs are the intermediate polars (IPs) or DQ Her stars. Systems with magnetic fields between 1 – 10 MG. With an intermediate field strength, the IPs combine the features of the non-magnetic systems in their outermost regions forming a disc, with those of the magnetic systems in areas close to the WD, disrupting the disc and re-routing the material to the magnetic poles.

When the magnetic field of the WD is not sufficiently strong as in the case of intermediate poles, it can interact with the secondary magnetic field at the point where they meet, thus forming a drag force that is eventually transferred to slower rotation periods. The system can become completely out of synchronism, ending with periods of rotation of one tenth of its orbital period.

The orbital period distribution of IPs, although more dominant above the period gap, are quite spread (Figure 3.6). To form a disc they need either a relatively weak magnetic field or large orbital periods.

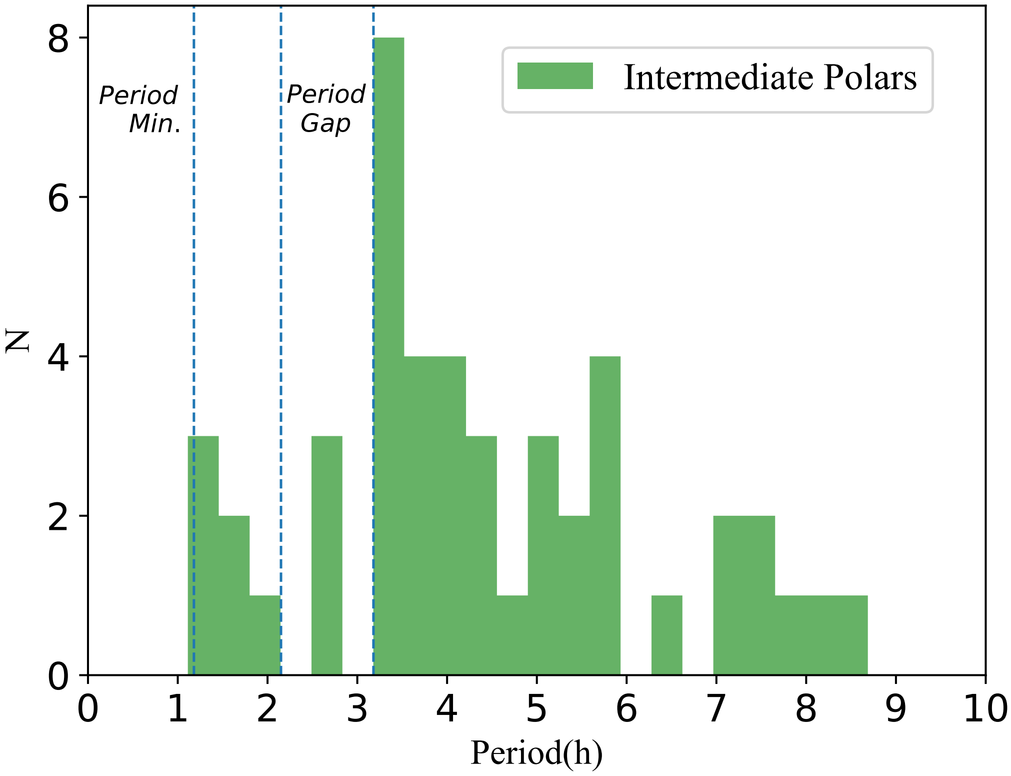

FIGURE 3.6: Period distribution for IPs. Most of them accumulated above the gap.

Chapter 4

Wide field survyes and ancillary data

4.1 Wide field surveys

It is difficult to find a definition for a survey. One can attempt by saying that an astronomical survey *is an observational systematic study of a class of objects or a region of the sky*. On the basis of the adopted technique, one can roughly divide surveys in “photometric” and “spectroscopic”. As their name suggests, “photometric” surveys are observations in one or more bands and they will be the main topic discussed further. “Spectroscopic” surveys employ spectroscopic observations to characterise an object or a class of objects. Depending on the adopted field of view, we can also speak about “pencil beam” surveys and “wide field surveys”. A “pencil beam” survey is an observation of a small region of sky. Normally, this is done in different filters and it is carried out at very big depths to identify very faint objects (typically, very far away galaxies). Conversely, a “wide field survey” is, as its name suggests, an observation of a large region of sky.

One can also be tempted to refer as “survey” as the study of one specific object at multiple wavelengths. This would certainly be the case of relevant objects like η Carinae.

In this section, we will refer to a series of surveys, recall their main characteristics and their impact on astronomy.

4.1.1 The Hubble Deep Field

It is hard to speak about surveys without mentioning the Hubble Deep Field, perhaps the most iconic observation ever done with the Hubble Space Telescope (HST). The HDF was a cosmological survey using the unique capability of the Wide Field / Planetary Camera 2 (WFPC2) on board the HST to reach unprecedented limiting magnitudes. Together with the extraordinary quality of this unique dataset, the key feature of the HST is that the data were immediately made public, so that the whole community could use them.

Several surveys have built on the experience of this project. It is perhaps worth remembering the OSIRIS Tunable Emission Line Object (OTELO) project, the deepest emission line survey ever made, carried out with the Optical System for Imaging and low-Intermediate-Resolution Integrated Spectroscopy (OSIRIS) instrument on the Gran Telescopio Canarias, the largest fully-steerable telescope of the world.

4.1.2 The Sloan Digital Sky Survey

The Sloan Digital Sky Survey (SDSS) defines a before and after with respect to the planning, execution and data distribution of a survey. The project has been designed to study the cosmological large scale structure using quasars. The filter set developed for the photometry of this project has soon become a largely used standard in several observatories. The more rectangular shape with respect to, for example, the Johnsons-Cousins filters makes the SDSS filters ideally suited for separating population of objects. The project also benefited from a multi-object spectrograph which is still providing high quality data. Of course, the availability of a dedicated wide field telescope has been key to the success of the project which could be performed without having to share telescope time with anyone else.

Arguably, the main reason for the success of SDSS is that the access to the science-ready data is comparatively easy. The use of multiple filters and repeated (incremental, both in amount and quality) data releases, has allowed the project to be successful well beyond its original idea thus making it a reference for surveys to come.

4.1.3 Surveys beyond the optical regime

As briefly commented for SDSS, a crucial aspect for a survey is the availability fo a dedicated telescope. In the case of the Two Micron All-Sky Survey (2MASS), these have been two telescopes located in the two hemispheres providing a unique and uniform all sky coverage in near-infrared in broad band J, H and K_S filters. Considering the wavelength coverage and the filters adopted, it is clear that this project has been particularly successful in the study of cool stellar objects (cold stars and BDs) and distant (yet bright) QSOs.

In some cases, the dedicated telescope needs to be placed in space, like it has been the case of the Galaxy Explorer (GALEX) or the Wide-field Infrared Survey Explorer (WISE). GALEX is an ultraviolet spacecraft which carried out a survey of the extra-galactic sky in ultraviolet. This represents the largest ultraviolet dataset available. Despite missing the Galactic plane, this project has given large contribution to stellar astronomy, in particular in the study of very hot objects, like white dwarfs.

WISE is an infrared satellite observing the whole sky in 4 custom broadband filters. The success of this mission can be measured in the fact that it has been revived several times already, every time with a different scope and that multiple catalogues have been produced.

4.1.4 Time-domain Surveys

Over the last few years, several projects have started taking repeated observations of the sky to obtain time-domain information. This requires some trade off between the field of view of the telescope, the image quality, the cadence of the observations and the filters to be used. The main science cases for these projects tend to be Solar System objects (in particular the surveillance for potentially hazardous objects) and supernovae.

The Catalina Real Time Survey (CTRS) and the All-Sky Automated Survey for SuperNovae (ASAS-SN) are two surveys based on an array of multiple telescopes spread all around the world providing nearly continuous coverage to the sky observation. The size of the telescopes is modest and only one or two filters are used. Over the last few years, these projects have provided exquisite light curves of virtually any type of variable object.

The Panchromatic Survey Telescope And Rapid Response System (Pan-STARRS) is a project based in Hawaii. Originally featuring four 2-m telescopes, only two have been built. It observes in 5 photometric bands (g, r, i, z, and y) and its repeated observations have resulted in very deep images of the Northern sky which are now the photometric reference in that region.

The Palomar Transient Facility (PTF) and the Zwicky Transient Facility (ZTF) are also being carried out with a single telescope, located at Palomar Observatory. ZTF, being currently observed, provides an almost continuous stream of discoveries which is being a critical factor in preparation for the Vera Rubin Observatory (VRO, formly known as Large Survey of Space and Time, LSST) which will be carried out with a dedicated wide field 8-m telescope. VRO will last ten years and it is expected to revolutionise astrophysics providing a time-domain multi-filter view of the sky and impacting virtually all branches of astrophysics thanks to its filters, the excellent image quality and the repeated observations of a telescope with such a vast collecting area.

In summary, surveys (and in particular wide-field surveys) have largely impacted most fields of astrophysics. They are critical in the discovery and study of rare phenomena as well as in the possibility to provide large samples for statistical studies.

Arguably, the success of a survey can be measured in the number of works which use the data of a project by people who were not involved in the definition, construction and execution of it.

As it has been shown, the quality of the data is only one important aspect that leads to the success of a survey. Easy data access and clear documentation are crucial.

4.2 Ancillary Data

In this section all the data used in later chapters is explained, as well as a brief description of the underlying sources they come from.

As a general guide, the data obtained from the Javalambre Photometric Local Universe Survey (J-PLUS, Section 4.2.1), is the reference data, and depending on the methodology used (explained in 6.3 and 7.1), they are cross-matched with WISE (Section 4.2.3) and/or with the Global Astrometric Interferometer for Astrophysics survey (Gaia, Section 4.2.4). The SDSS survey spectroscopic database (Section 4.2.2) is used to extract the CV synthetic photometry for objects which are not within the J-PLUS DR1 footprint, expanding our CV sample. We also use the available spectra of our CV candidates to obtain an estimate of the purity of the methodology employed.

Since some of the J-PLUS bands are coincident with those of SDSS, to differentiate them, we refer to those of J-PLUS as $uJAVA$, g, r, i and z, and to those of SDSS as u', g', r', i' and z'.

4.2.1 The J-PLUS survey

J-PLUS (Cenarro et al., 2019) is a survey of 8,500 deg^2 of the northern sky. It is carried out with the 0.83-m Javalambre Auxiliary Survey Telescope (JAST/T80) at the Observatorio Astrofísico de Javalambre[1], equipped with the panoramic

---

[1] http://oaj.cefca.es

camera T80Cam, which has a field of view of 2 deg^2, a pixel scale of 0.55 arcsec pixel^{-1} and 12 filters: 4 broad (g, r, i and z, coincident with those in the SDSS), 2 intermediate (*J0861* and *uJAVA*) and 6 narrow band ones (*J0378*, *J0395*, *J0410*, *J0430*, *J0515* and *J0660*)[2]. See Figure 4.1 and Table 4.1 for their properties.

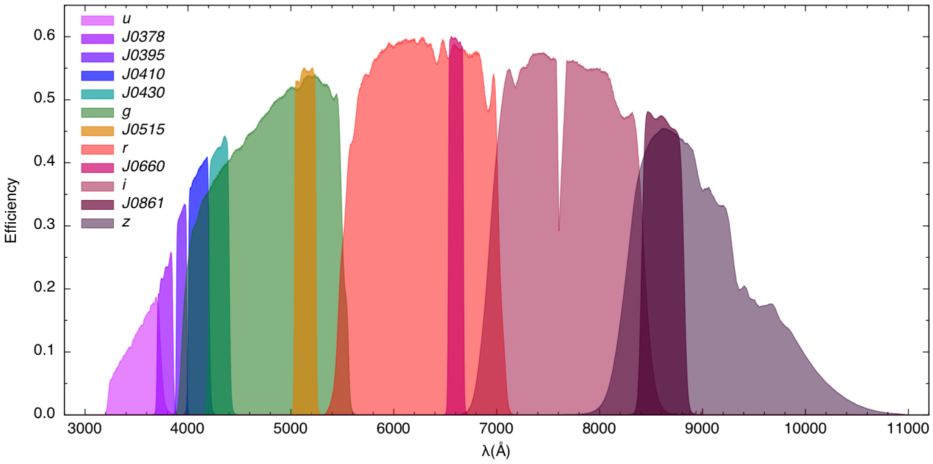

FIGURE 4.1: Efficency curves measured for the set of 12 J-PLUS filters, including the effect of the entire system (sky, mirrors, lenses and CCD). Source, Cenarro et al. (2019)

These filters are located at key stellar spectral features that allow to retrieve accurate spectral energy distributions for more than 5 millions of stars in our Galaxy. Given this unique set of filters, J-PLUS is in a remarkably good position to identify CVs which have gone unnoticed so far.

Photometric Search

We make use of the J-PLUS Data Release DR1 in the J-PLUS archive[3] through the *Virtual Observatory* (VO) *Asynchronous Queries* option, which allows to search the database by different criteria using Astronomical Data Query Language (ADQL). The J-PLUS archive contains several tables for different purposes, including cross-matches with other large surveys such as SDSS DR12, Gaia DR2 or AllWISE. For our search, we use the *jplus.CalibratedMagABDualObj* catalogue, which contains the main parameters of the astronomical objects. The object detection and aperture definition is performed in a reference band (r) and the measurements are done in each filter using SExtractor (Dual Mode).

---

[2] For further information on the J-PLUS photometric system, visit: http://svo2.cab.inta-csic.es/theory/fps/index.php?mode=browse&gname=OAJ

[3] http://archive.cefca.es/catalogues/jplus-dr1

Filter	Central Wavelength [Å]	FWHM [Å]	Comments
uJAVA	3485	508	
J0378	3785	168	[OII]
J0395	3950	100	Ca H+K
J0410	4100	200	Hδ
J0430	4300	200	G-band
g	4803	1409	(a)
J0515	5150	200	Mg*b* Triplet
r	6254	1388	(a)
J0660	6600	138	Hα
i	7668	1535	(a)
J0861	8610	400	Ca Triplet
z	9114	1409	(a)

TABLE 4.1: The J-PLUS filter system. Comments: (a) In common with SDSS.

In order to obtain quality data from the J-PLUS archive, some constraints are placed. We restrict our query to objects with photometry errors lower than 0.2 (*err_filter* < 0.2), with data in most of the exposures comprised by a tile in which the source appears (*Norm_wmap_val_filter* > 0.8), not contaminated by external effects such as reflections or by other sources (*mask_flag_filter* = 0), detected in all filters (*single_detect_filter* > 0), not saturated objects in r but including those flagged as 'variable' (*Flag_r* < 4 or 2047 < *Flag_r* < 2052) and classified as point sources (*CLASS_STAR* > 0.8). Appendix A shows an example of data cleansing through the VO Asynchronous Queries using the ADQL language.

4.2.2 SDSS DR15 spectroscopic database

The SDSS is a multi-colour imaging and spectroscopic survey carried out with a 2.5-m wide-angle optical telescope at Apache Point Observatory in New Mexico, United States. Its DR15 spectroscopic database comprises spectra for more than 4 millions objects. The SDSS spectra is limited by the optical range ($\sim 4000 - 9500$ Å).

The spectroscopic data is accessible through the SkyServer webpage[4] and it provides a set of tools to make queries by position, spectral classification,

---

[4] http://skyserver.sdss.org/dr15/en/home.aspx

redshift and other constraints as well as SQL (Structured Query Language) searches and access to the catalogues, images and spectra downloads. We use this dataset and the tools provided by the SkyServer to simulate J-PLUS observations of our CV sample (see section 6.1) and also as a first testing bench of our CV candidates by checking the nature of the available ones.

4.2.3 WISE

WISE is an infrared-wavelength all-sky survey using a 40-cm infrared space telescope. It has mapped the sky at 3.4, 4.6, 12, and 22 μm corresponding with the so-called filter bands *WISE1, WISE2, WISE3* and *WISE4* respectively.

The WISE All-Sky data can be accessed through the on-line and machine-friendly services of the NASA/IPAC Infrared Science Archive (IRSA)[5] and is VO compatible. WISE allows us to check for infrared excesses from the CV companion, especially for cold secondaries, low mass-transfer CVs where the spectra are not dominated by the disc and the secondary is visible. A similar approach has already been carried out by Scaringi et al. (2013).

4.2.4 Gaia

Gaia is a space observatory whose mission is to make the largest, most precise three-dimensional map of the Milky Way to-date by detecting and measuring the motion of each star in its orbit around the center of the Galaxy.

The second data release (GDR2 hereafter) is based on 22 months of observations and provides positions, parallaxes and proper motions for 1.3 billion sources up to $G \sim 20$ magnitudes. This kind of data allows the derivation of distances and absolute magnitudes among others, offering a global overview of our Galaxy.

Deriving absolute magnitudes

One of the aims of this work is finding the CV locus in the H-R diagram and we make use of GDR2 data to compute their absolute magnitude M through

$$M = m + 5 - 5\log(d) + A, \tag{4.1}$$

where m is the apparent magnitude, A is the interstellar absorption and d, the distance to the source which can be obtained by the GDR2 data.

---

[5] https://irsa.ipac.caltech.edu/Missions/wise.html

However, inferring the distance from the Gaia DR2 parallax is not a trivial issue (Luri et al. 2018). The most direct way to estimate distances is by inverting its parallax (ϖ^{-1}) but the uncertainty on the parallaxes, the non-linearity of the transformation, and the positive constraint of distance (but not of parallax) would lead to unrealistic results for most of the sources. Only those objects with positive parallax and a small fractional parallax error ($f_{obs} = \sigma_{\varpi}\, \varpi^{-1} < 0.2$), are suitable for computing their distance by ϖ^{-1}. Beyond this value of f_{obs}, the probability distribution function (PDF) of the derived distance (d) given ϖ and σ_{ϖ} becomes non-gaussian, looking asymmetrical and presenting a long tail towards large values of d and consequently, the mode of the PDF (the most probable value) does not coincide with the true distance.

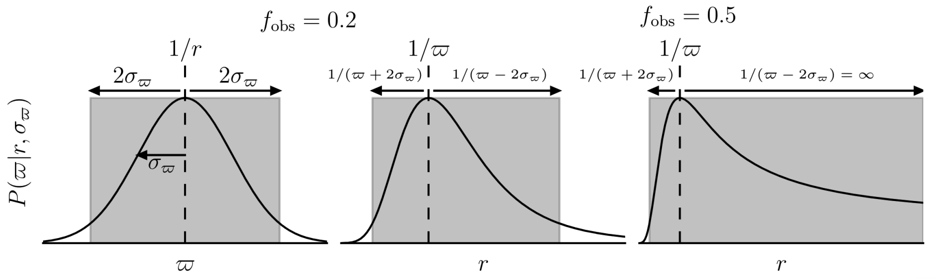

FIGURE 4.2: The left and middle panels are the probability $p(\varpi|d, \sigma_{\varpi})$ as a function of ϖ and of d respectively for an object with $f_{obs} = 0.2$. The right panel is as the middle one but for $f_{obs} = 0.5$. The shaded areas indicate the 2σ credible interval about d^{-1} and the corresponding transformed credible interval. Figure is taken from Astraatmadja and Bailer-Jones (2016)

One could discard all these sources with negative parallaxes and $f_{obs} > 0.2$, but by doing so, we would be missing $\sim$ 80% of the objects. Since our final goal is to build a catalog of CVs, limited but complete in magnitude, we need a different approach to obtain relatively precise estimates of d for all objects with available parallaxes.

In order to do so, we adopt the approach of Bailer-Jones et al. (2018). They infer distances and their uncertainties through a probabilistic analysis based on the Bayes theorem. In this context, the aim is obtaining the most probable distance given a parallax and its uncertainty. It is represented as $p(d|\varpi, \sigma_{\varpi})$, it is called "the posterior" and is computed by the well known Bayes theorem

$$p(d|\varpi, \sigma_{\varpi}) = \frac{p(d, \varpi, \sigma_{\varpi})}{p(\varpi, \sigma_{\varpi})} = \frac{p(\varpi|d, \sigma_{\varpi})\, p(d)}{p(\varpi, \sigma_{\varpi})}, \tag{4.2}$$

where $p(\varpi, \sigma_\varpi)$ is the evidence and can be understood as the normalization parameter. The term $p(\varpi, |d, \sigma_\varpi)$ is the so-called likelihood and represents the PDF of the measured ϖ. Indeed, given any distance and due to the linearity of the model (unlike the model based on d), this likelihood is theoretically of Gaussian shape which has also been confirmed empirically (Lindegren et al., 2018). $p(d)$ is the prior and it describes the assumptions or previous knowledge about the distribution of the distances.

Bailer-Jones et al. (2018) adopted an exponentially decreasing space density (EDSD) prior to compute the distances[6] for the 1.33 billion sources from GDR2. These are available using ADQL[7] and we here use them to derive the absolute magnitudes through Equation 4.1 and also as a delimiter for galactic and extra-galactic objects.

$$P(r|L) = \begin{cases} \frac{1}{2L^3} r^2 e^{-r/L} & \text{if r>0} \\ 0 & \text{otherwise} \end{cases} \tag{4.3}$$

where $L > 0$ is a length scale. L varies as a function of Galactic longitude and latitude(ℓ, b) according to a model which reflects the expected variation in the distribution of stellar distances.

By substituting the Gaussian likelihood with mean ϖ and standard deviation σ_ϖ and the EDSD prior in Equation 4.3, the unnormalized posterior is obtained by

$$P^*(r|\varpi, \sigma_\varpi, L(l,b)) =$$

$$P^* = \begin{cases} r^2 exp\left[-\frac{r}{L(l,b)} - \frac{1}{2\sigma_\varpi^2}\left(\varpi - \varpi_{zp} - \frac{1}{r}\right)^2\right] & \text{if r>0} \\ 0 & \text{otherwise} \end{cases} \tag{4.4}$$

$\varpi_{zp} = -0.029$ mas is the global estimate of the zero point parallax obtained from Gaia's observations of QSOs. ℓ, b, ϖ and σ_ϖ are taken directly from the GDR2 catalog. The normalization term is achieved by equating the

---

[6] For a detailed explanation of this approach and an analysis of applying this technique refer to Bailer-Jones et al. (2018). For a discussion of the use of different priors, see Bailer-Jones et al. (2018),Luri et al. (2018),Igoshev, Verbunt, and Cator (2016),Astraatmadja and Bailer-Jones (2016))

[7] http://gaia.ari.uni-heidelberg.de/tap.html

integral of this posterior to 1.

We use these distances to derive the absolute magnitudes through Equation 4.1 and also as a delimiter for galactic and extra-galactic objects.

Chapter 5

Disentangling cataclysmic variables in Gaia's HR diagram

The text of this chapter is based on Abril et al. (2020)

During the evolution of a CV, the system goes through different states and configurations (see Chapter 2), therefore it will change appearance: The relative contribution of the WD, the secondary star and the accretion disc or stream makes for unique colours (e.g. Szkody et al., 2002). The systems thus occupy distinct locations in colour-colour diagrams with respect to single stars. Due to the relatively small sample of CVs and the inherent difficulty of any source in obtaining its distance, it has not been possible so far to perform an analysis of the CV absolute magnitude distribution. With the arrival of *Gaia*, this has changed. Already Pala et al., 2019 show the advances that *Gaia* parallaxes bring to the understanding of CVs, and we now have the data to study CVs in the HR-diagram.

5.1 The Catalogue of *Gaia* DR2 and the cross-match with CV catalogue

As stated in Section 4.2.4, by measuring the motion and parallax of each star in its orbit, *Gaia's* mission is to obtain a precise three-dimensional map of the Milky Way. To this means, the three filters G, G_{BP} and G_{RP} are observed at several epochs over a period of about 670 days of mission operations (for details, see Gaia Collaboration et al., 2018), which, depending on the nature of the source, might have some implications to consider.

5.1.1 The impact of *Gaia* data on CVs

GDR2 provides weighted mean fluxes[1] and, as CVs are variable stars, this procedure has an effect on their G, G_{BP} and G_{RP} values. The degree of impact might be determined by comparing the 670-days length of the *Gaia*-mission and the cycle of variation length for every CV subtype. The highest impact is on DNe systems as they can have outbursts even on a weekly base (Sterken and Jaschek 2005 and references therein). The low recurrence in Novae, NLs and Magnetic CVs should have no significant impact on the overall sample.

5.1.2 The CV sample

The Catalog and Atlas of Cataclysmic Variables (Downes et al., 2001) includes all objects which have been classified as a CV at some point in time. Although it was frozen on February 1st, 2006, it is one of the main references among the community, providing coordinates, proper motion, type, chart, spectral and period references for all 1830 sources when available. In order to obtain the purest sample, we discarded from this catalogue the objects designated as "NON-CV", which are stars that have been previously identified as CVs but later confuted, and those with the extensions ":" and "::" because their classification is not conclusive.

The Catalog of Cataclysmic Binaries, Low-Mass X-Ray Binaries and Related Objects (Ritter and Kolb, 2003) which only contains objects with a measured period, is updated up to December 31st, 2015 and it provides coordinates, apparent magnitudes, orbital parameters, stellar parameters of the components and other characteristic properties for 1429 CVs. In this case uncertain values are followed by only one ":" and have been discarded as well.

Both catalogues have been merged into a final sample of 1920 CVs, out of which 1187 are contained in the GDR2 footprint. The density studies of CVs in the HR-diagram were done using this full sample. For 839 of these systems, the orbital period is known, and for 1130 systems, the subtype is unambiguously known (see Table 5.1).

---

[1] Weighted means are used because flux errors on different epochs may vary depending on the configuration of each observation. See Carrasco et al., 2016 and Riello et al., 2018 for detailed information.

TABLE 5.1: Distribution of the CV sample utilised by subtype.

CV subtype	Periods sample	Main sample	Centroid position in HRD $G_{BP} - G_{RP}$	G_{abs}
Novalike	76	119	0.37	5.63
Dwarf Novae	484	688	0.64	9.49
Classical novae	77	119	0.79	5.58
Polar	75	135	0.83	9.67
Intermediate Polar	51	69	0.59	5.61
Total Sample	839	1130		

5.2 CVs in the HR-diagram

5.2.1 The impact of the orbital period

Left panel of Figure 5.1 displays the CV locus in the HR-diagram of all CVs for which an orbital period is known (839 systems). The orbital period of each system is represented by the colour of the symbol as defined in the auxiliary axis. The CVs lie on average between the main sequence stars and the WDs. A clear trend is seen on their position with the orbital period: CVs with longer periods fall close to the main sequence path, while, as the orbital period decreases, they approach the WDs region. This behaviour can be understood from the contribution of the secondary star. On average, a Roche-lobe filling secondary star is larger and brighter for longer orbital periods, while the WD does not change much during the secular CV evolution. Hence, the contribution of the secondary should be more dominant for longer orbital periods. Systems below the period gap, are instead dominated by their WD, as the secondary becomes only visible in the near infrared and does not contribute to the *Gaia* colour. The contribution of the accretion disc should change colour and magnitude depending on the sub-type and will be discussed in the next subsection.

The right panel of Figure 5.1 shows the locus of all CVs of our sample defined in Section 5.1.2 within *Gaia's* HR-diagram. On the x- and y-axis, the respective projected density is plotted. A high density area is well distinguishable at $G_{BP} - G_{RP} \sim 0.56$ and $G_{abs} \sim 10.15$ (values obtained from the mode of the marginal distributions) which corresponds to the population below the period gap.

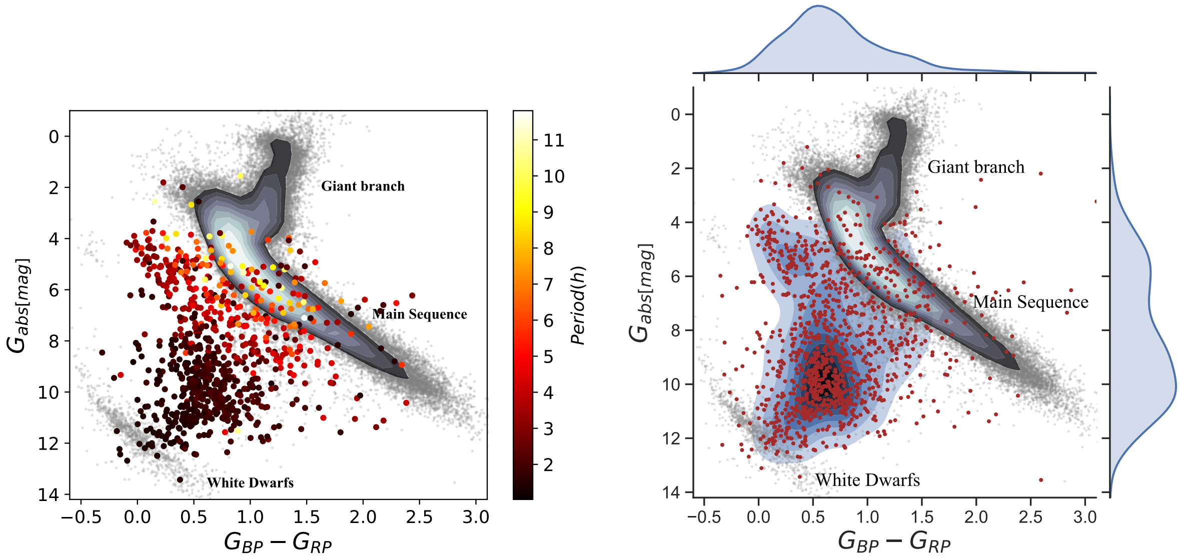

FIGURE 5.1: In grey, all stars from *Gaia*'s 2nd data release are plotted in the HR-diagrams. On the left side, the CVs period distribution, the CVs from our sample with known orbital periods (see Section 5.1.2) are plotted in larger dots. The colour of each dot refers to the orbital period as given in the bar at the right of the panel. CVs with larger periods lie close to the main sequence path getting shorter while approaching the white dwarfs area. On the right, the density distribution of our whole sample of CVs (brown dots), surfaces with different tones of blue represent areas of equal density. On the x- and y-axis the marginal distributions are shown. CVs lie on average between the MS path and the WDs with a high density area peaking at $G_{BP} - G_{RP} \sim 0.56$ and $G_{abs} \sim 10.15$. Such area corresponds to the overpopulation below the period gap as reflected in the left panel by black dots, CVs with orbital period below 2 h.

5.2.2 The locus depending on the subtype

Figure 5.2 exhibits the distribution of every CV subtype on the HR-diagram. Bivariate Gaussian distributions are computed for 1 and 3 σ given by

$$p(x,y|\mu_x,\mu_y,\sigma_x,\sigma_y,\sigma_{xy}) = \frac{1}{2\pi\sigma_x\sigma_y\sqrt{1-\rho^2}} exp\left(\frac{-z^2}{2(1-\rho^2)}\right), \tag{5.1}$$

where

$$z^2 = \frac{(x-\mu_x)^2}{\sigma_x^2} + \frac{(y-\mu_y)^2}{\sigma_y^2} - 2\rho\frac{(x-\mu_x)(y-\mu_y)}{\sigma_x\sigma_y}, \tag{5.2}$$

and

$$\rho = \frac{\sigma_{xy}}{\sigma_x\sigma_y}, \tag{5.3}$$

using the median instead of the mean and the interquartile range to estimate variances in order to avoid the impact of outliers. The results are given in Table 5.1.

NLs are dominated by a high mass-transfer accretion disc, that usually overshines the WD and the secondary star at optical and even infrared wavelengths. Their colour and final absolute magnitude mainly depends on the inclination with respect to the line of sight. In the HR-diagram, they concentrate around $G_{abs} = 5.63$ and $G_{BP} - G_{RP} = 0.37$, i.e. on the blue and bright corner of all CVs. A similar locus but with a much higher scatter is occupied by the classical novae and by IPs. This can be explained by the eclectic composition of these two sub-groups which also contain a large fraction of NL stars.

In contrast, polars which do not accrete mass through a disc, are much fainter and their colour and magnitude will depend on the nature of the secondary. In the HR-diagram they scatter around $G_{abs} = 9.67$ and $G_{BP} - G_{RP} = 0.83$ representing the reddest and faintest of all the CV subgroups.

DNe occupy the whole region between MS stars and WDs with the centroid being at $G_{abs} = 9.49$ and $G_{BP} - G_{RP} = 0.64$. Since the secondary star in these systems can be anything from an early K-type star down to a BD, the range in colours and magnitude is not surprising. In addition, these sources are characterised by undergoing regular outbursts increasing their brightness and blueness. As discussed in Section 5.1, the given magnitude is a weighted

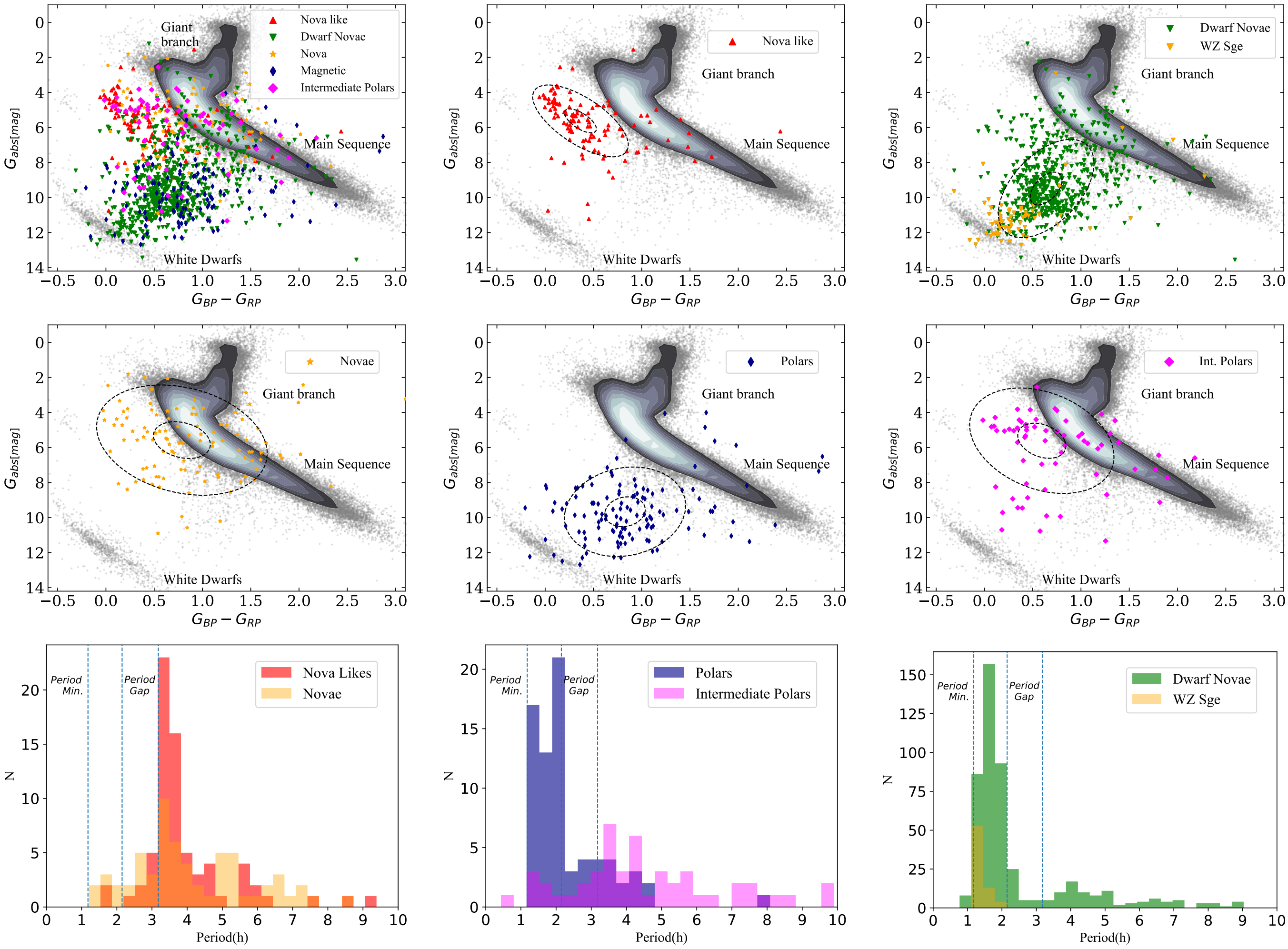

FIGURE 5.2: The distribution of CV subtypes in the HR-diagram. Top-left panel shows all subtypes together, after that every subtype separately. The dashed ellipses represent 1 and 3 σ of each subtype bivariate Gaussian distribution. The sample utilized here is composed by all CVs in the Ritter and Kolb (2003) and Downes et al. (2001) catalogues (see Section 5.1.2) whose subtype is unambiguously known and are included in the *Gaia* footprint; 119 NLs, 688 DNe, 119 Novae, 135 Polars and 69 IPs. On the bottom, the period histograms for each subtype.

mean of several epochs and thus also increases the spread of this distribution. A detailed study of the DNe locus depending on their subtype and outburst state can be done following the next *Gaia* release when individual measurements and epochs become available.

WZ Sge-type objects deserve a separate mention, a class of DNe characterised by great outburst amplitudes, slow declines and long intervals between outbursts compared with ordinary DNe. These kind of systems have been considered to be period bouncer candidates (Patterson, 2011), some of them extensively investigated in this regard (QZ Lib, Pala et al. 2018; J122221 Neustroev et al. 2017 and Kato et al. 2013; J184228 Kato et al. 2013; J075418 and J230425 Nakata et al. 2014). We have plotted a sample of 71 of such systems in the upper-right panel of Figure 5.2, along with the rest of DNe, and it can be seen that they concentrate near the WDs area. This is consistent with them being period bouncers or similar systems, as these are the CVs with the lowest mass transfer and faintest secondary stars. The disc is only visible in some emission lines, the secondary does not contribute to the optical range at all.

5.2.3 Detached CVs

Another question we can address is finding the locus occupied by the so-called detached Cataclysmic Variables (dCVs) crossing the orbital period gap. A first approach could be made by finding the area with boundaries in 2 and 3 h in the left panel of Figure 5.1 using regression techniques. However, since dCVs no longer contain an accretion disc, they should appear fainter than regular CVs of the same period.

Due to the continuous mass loss, the donor is being driven out of equilibrium and secondaries in CVs just above the period gap are bloated up to 30% with respect to regular MS stars (Knigge, Baraffe, and Patterson, 2011). When the mass transfer stops, the secondary shrinks towards its thermal equilibrium radius to nearly its equivalent for MS stars (Howell, Nelson, and Rappaport, 2001) and hence we expect secondaries in dCVs to be comparable to single MS stars of the same type.

Since the mass transfer ceases, the mass and spectral type of the donor star stays constant during the interval in which the binary is detached. In regular CVs this happens at $M_{sec} = 0.2 \pm 0.02\,\mathrm{M}_{\odot}$ (Knigge, 2006) and spectral type $\sim$ M6 (Rebassa-Mansergas et al., 2007), though variations occur depending on the moment in which the CV started the mass transfer and the time passed as CV until the secondary becomes fully convective. In the extreme case of a CV starting the mass transfer within the period gap range, the donor star type will be that of a fully convective isolated M star, which, according to Chabrier and Baraffe (1997), occurs at $M_{sec} \sim 0.35\ \mathrm{M}_{\odot}$ and spectral type M4. We thus assume that the secondary of dCVs is in the range M4–M6.

So far the only observational evidence for the existence of dCVs come from Zorotovic et al. (2016), who show that the orbital period distribution of detached close binaries consisting of a WD and an M4–M6 secondary star cannot be produced by Post Common Envelope Binaries (PCEBs) alone, but a contribution of dCVs is needed to explain the peak between 2 and 3 h. They also show that the systems inside this peak have a higher average mass than would be expected for normal WDMS systems. Still, with only 52 such systems known in total (WDMS systems with secondary spectral types in the range M4–6 and orbital periods below 10 h) and 12 between 2 and 3 h, the significance is not very high.

We distinguish two groups, the sources with orbital periods corresponding to those of the period gap (2–3 h) and therefore, more likely to be dCVs, and the rest with periods outside this range. In Figure 5.3 they are plotted in the HR-diagram, the former appear fainter compared to the latter. This can be explained by the higher WD masses in CVs, and consequently in dCVs, than in PCEBs, making them smaller in size and surface and contributing in a lesser extent on the brightness of the whole system.

In summary, we have analyzed the evolutionary cycle of CVs from a statistical perspective using *Gaia* DR2 data in conjunction with the HR-diagram tool. We have reported the discovery of a trend of the period and mass accretion with colour and absolute magnitude. We have also investigated their density distribution as a whole population, peaking at $G_{BP} - G_{RP} \sim 0.56$ and $G_{abs} \sim 10.15$, and the contribution of the main CV subtypes to this regard, highlighting the location of WZ Sge systems, which are period bouncer candidates. Finally, we have identified the location and a trend among systems comprised of a WD and secondary in the range M4–M6, which correspond with dCVs, CVs going through the orbital period gap.

Acknowledgements. This research has made use of the VizieR catalogue access tool, CDS, Strasbourg, France (DOI: 10.26093/cds/vizier). The original description of the VizieR service was published in 2000, A&AS 143, 23.

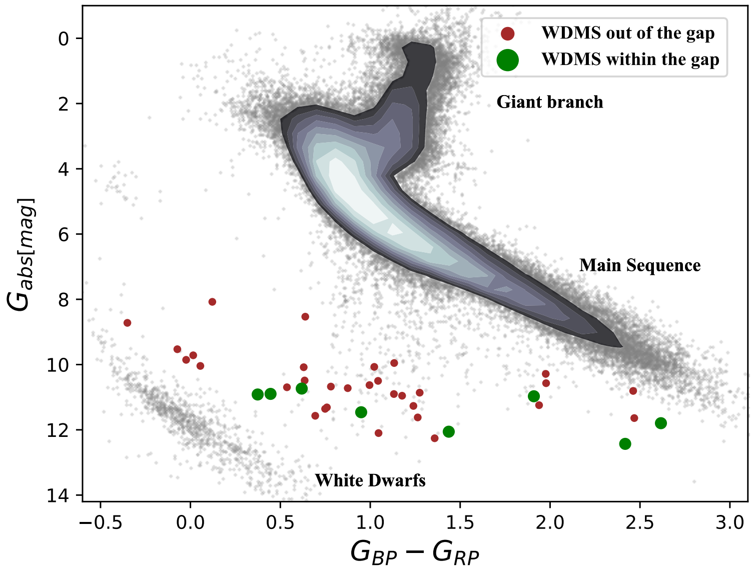

FIGURE 5.3: Systems comprised by a WD and an M4-6. The figure contains the 39 objects from the sample by Zorotovic et al. (2016) present in *Gaia* (see text). In green are those within the period gap and in brown the rest. All of them follow a trend but the objects within the gap are on average fainter.

Chapter 6

Identification of CVs through J-PLUS colours

As already mentioned in the introduction of this thesis, Section 1.1, CVs are one of the best sources to test our understanding of many astrophysical phenomena involving evolution of compact, interacting binaries. However, in spite of more than 1100 systems known (see Ritter and Kolb, 2003), no large sample with the completenes and observational bias known and understood could be established so far and this yields problems with the interpretation of the period distribution of CVs.

It is fundamental to resolve these disagreements in order to validate the application of these models to many other present and complex systems and a larger and well known population of them becomes necessary. The aim of this chapter is to provide the necessary enlargement of the sample of well characterized CVs in order to carry out in a future work a stringent test on the present models of CV evolution.

In this context, we aim at searching for CVs in J-PLUS. We also make use of the SDSS , WISE and Gaia. In this chapter, three methodologies using colour-colour diagrams are presented while the next one covers a different approach by using machine learning techniques. Both are based on the first data release of J-PLUS DR1 catalog which covers 1022 deg^2.

6.1 CVs Synthetic Photometry

At the date of this thesis, J-PLUS DR1 has released the data from the observations of 1022 deg^2. Since the CV population is characterized by a relatively low space density (de Kool, 1992; Kolb, 1993) , the J-PLUS DR1 has only observed 32 known CVs. This number is not statistically meaningful, but it will be useful as a test set.

We take the sample of 1920 CVs described in Section 5.1.2 and retrieved the spectra of all of them included in the spectroscopic database of SDSS DR15, resulting in 343 CVs which were revised one by one by eye in order to validate their CV nature. This sample contains several CVs of the different CV subtypes as well as high and low mass-transfer rate systems and therefore, we consider the sample to be representative of the CV population. We then computed the corresponding J-PLUS synthetic magnitudes by convolving the SDSS spectra with the J-PLUS filter transfer functions (see Figure 6.1). Since SDSS spectroscopy is limited to the range $\sim 4000 - 9500$ Å, it includes the i passband, but does not fully cover the range of the z filter. This complicates our intended use of the $i - z$ colour as a diagnostic method. In principle, we could take the z' value from the SDSS photometric data, while deriving i via the above outlined method. However, CVs are known to undergo periodic brightenings with amplitudes of up to 9 mag (Mattei, 1990) that arise from thermal instabilities in the accretion disc. Thus, in order to calculate colours, it is important that the individual magnitudes were obtained in the same brightness state. Because the SDSS photometric and spectroscopic data were taken during different epochs, it is possible that they correspond to different brightness states of the CV. To account for that possibility, we decided to take both the i' and the z' values from the SDSS photometry, so that it yields a consistent colour.

6.2 Background in the search of CVs

As already mentioned, the SED of a CV is the combination of spectra of a WD, the secondary star and, depending on the accretion rate and the magnetic field of the WD, an accretion disc. Therefore the SED of a CV will be very different from the SED of isolated non-accreting stars. Given their nature, CVs have been discovered in very diverse ways. Due to their variable nature, the search for CVs greatly benefited from serendipity findings based on their variability properties, mainly large-amplitude variables including DNe or classical novae. Such property has been exploited both in the past, e.g. U Geminorum (Hind, 1856), and also in recent times, for example, the CRTS has reported one thousand CVs (Breedt et al., 2014).

However, the ratio of discovered CVs was relatively slow until Warner (1976a), who gave great impetus to the search for CVs and their understanding by discussing the properties of 27 systems with known orbital periods,

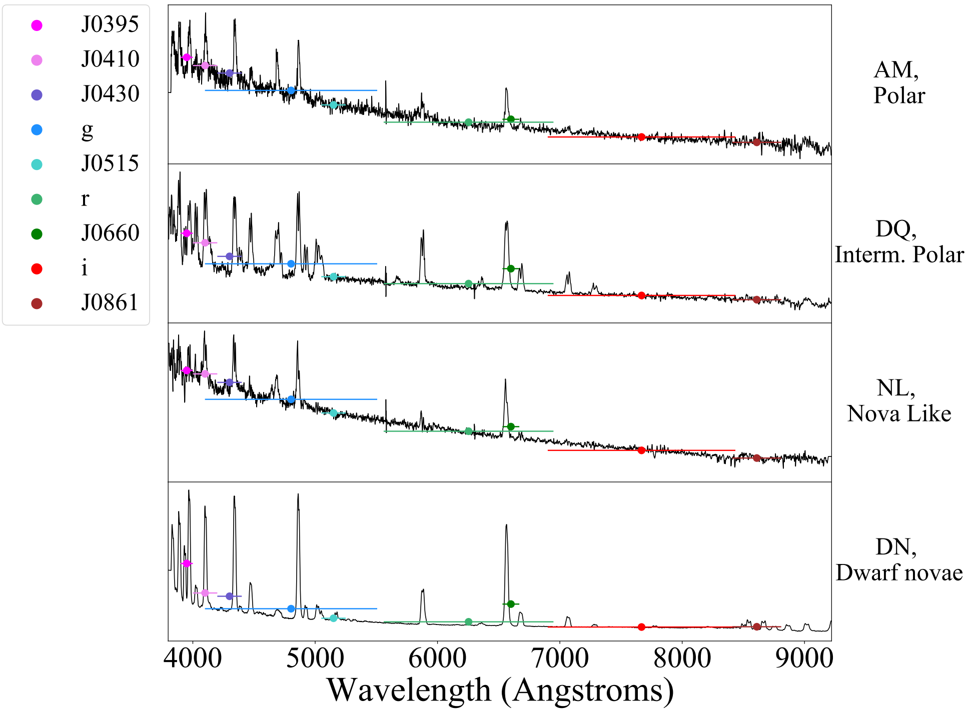

FIGURE 6.1: SDSS spectral samples of the four major types of CVs and their J-PLUS synthetic photometries overlapped, the horizontal lines represent their respective band FWHM. Bands *J0378*, *uJAVA* and *z* are not represented due to their insufficient coverage in SDSS.

revealing two of their most important features: a high density population at shorter orbital closely related to sharp cut-off at ~ 78 min periods (the period minimum), and an absence of systems in the $2-3$ h orbital period range. These findings led to the study of CVs in subsequent years, e.g. Eggleton (1976), relating the distribution of orbital period CVs to their angular momentum loss ratios, Whyte and Eggleton (1980) published for the first time the histogram of orbital periods with a sample of 33 CVs clearly showing the absence of systems between $2-3$ h, the period gap. This gave rise to the standard theory of CV evolution, the disrupted magnetic braking (Rappaport, Joss, and Verbunt 1983; Paczynski and Sienkiewicz 1983; Spruit and Ritter 1983).

More recently, with the arrival of large field surveys like the Two-degree-Field Galaxy Redshift Survey (2dFGRS) or the SDSS, CVs were found as by-product of QSO searches since they tend to cover the same locus in colour-colour diagrams based on broad-band, optical filters. In the last years, some attempts have been made to identify CVs based on Hα excess and WISE colours (Scaringi et al., 2013) or SDSS colours and proper motions (Gentile

Fusillo, Gänsicke, and Greiss, 2015).

6.2.1 Classification of CVs according to the search criteria

Depending on the mass-transfer rate, the magnetic activity of the WD and the inclination of the system, CVs can display a variety of observational properties. In general terms, the SED of a CV is defined by the effective temperature of the WD, the accretion disc, and the companion star. Typical temperatures of CV WDs are within the range of 10 000 K to 50 000 K (Pala et al., 2017) and, therefore, its contribution dominates the blue part of the spectrum. On the other hand, the colder companion emits mainly at red and infrared wavelengths. Furthermore, a CV spectrum usually shows Balmer lines in emission originating from the accretion disc, which, for high mass-transfer rate CVs, can be the dominant continuum source over the whole optical range.

Therefore, the search criteria seeking for different CV properties leads to an interesting classification. Four techniques have been the dominant ones in the search for CVs: variability, with a bias towards dwarf/classical novae; X-ray emission techniques for magnetics; colour cuts methods, suitable for NLs systems and those selected via spectroscopic techniques having no preference for any CV subtype.

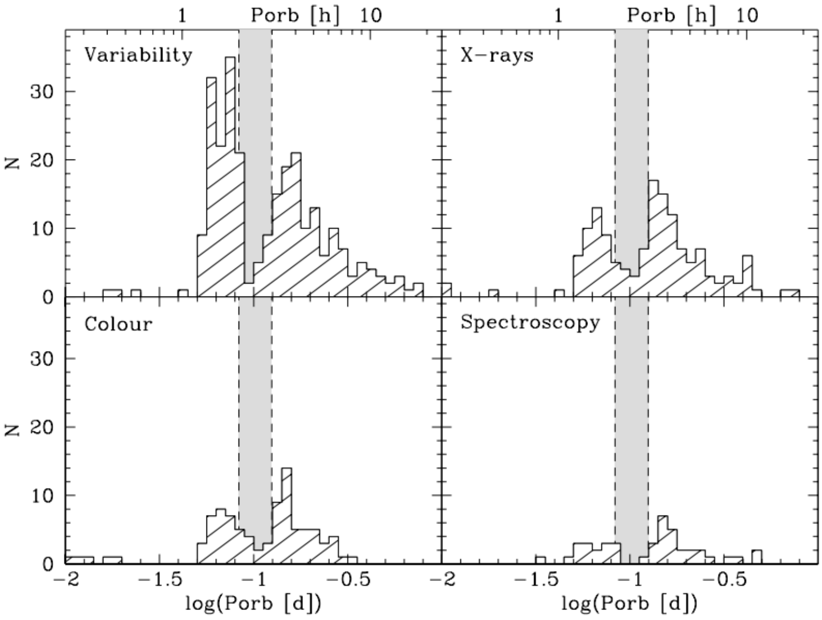

FIGURE 6.2: Distribution of CVs according to their discovery technique. Figure taken from Gänsicke (2004).

It is noteworthy that the four groups respect the above-mentioned features, the period gap and the period minimum (see Figure 6.2).

6.2.2 QSO as contaminants and the era of surveys

Roughly speaking, a CV spectrum can be blue and/or red depending on the mass transfer rate and, usually shows Hα in emission due to the presence of the accretion disc. High mass transfer CVs spectra tend to be dominated by the disc contribution so they often show higher Hα emission lines along with flatter continuum where the secondary is rarely visible.

However, since QSO spectral energy distributions are redshifted, they can display a variety of observational properties. Moreover, their much higher density compared to CVs makes them the main contaminants in CVs searches and their distinction more convoluted.

In broad band filters, QSOs at low redshifts appear mostly blue while they become redder as their redshifts increases. According to the redshift of the QSO, some line may be located at the same wavelength of Hα at rest frame (e.g. [O III] and Hβ at z $\sim$ 0.35, Mg II at z $\sim$ 1.35, C III at z $\sim$ 2.4 or C IV at z $\sim$ 3.25, see Figure 6.3).

This difficulty in distinguishing QSOs from CVs, added to the surge of large surveys in recent decades, has led to the discovery of an increasing number of CVs as byproduct of QSO searches. As compiled in Gänsicke (2004), the identification of 31 new CVs (Ringwald 1993, Ringwald 1996) resulted from the photographic U and B Palomar-Green survey. The ROSAT mission, the first imaging survey in soft X-rays, had great impact on the discovery of magnetics CVs (Haberl and Motch 1995, Beuermann 1998, Thomas and Beuermann 1998) but also providing new non-magnetic CVs and reaching over a hundred of new discoveries. The Edinburgh-Cape survey, another imaging U and B survey carried out by a 1.2-m telescope, found 15 new systems (Chen et al., 2001). The 2dFGRS Quasar Survey contributed with 21 new discoveries from a set of 48000 QSO colour-selected candidates.

The Hamburg Quasar Survey (HQS), an objective prism Schmidt survey carried out with the 80-cm Schmidt telescope at Calar Alto (Spain) led to the identification of 53 new CVs (see Gänsicke, Hagen, and Engels 2002) by the detection of Balmer lines in emission, blue colours and variability. The used criteria was able to detect $\sim$ 90% of the known short-period systems ($P_{orb} <$ 2 h) dropping to $\sim$ 40% above the gap due to the weak or lack of Balmer

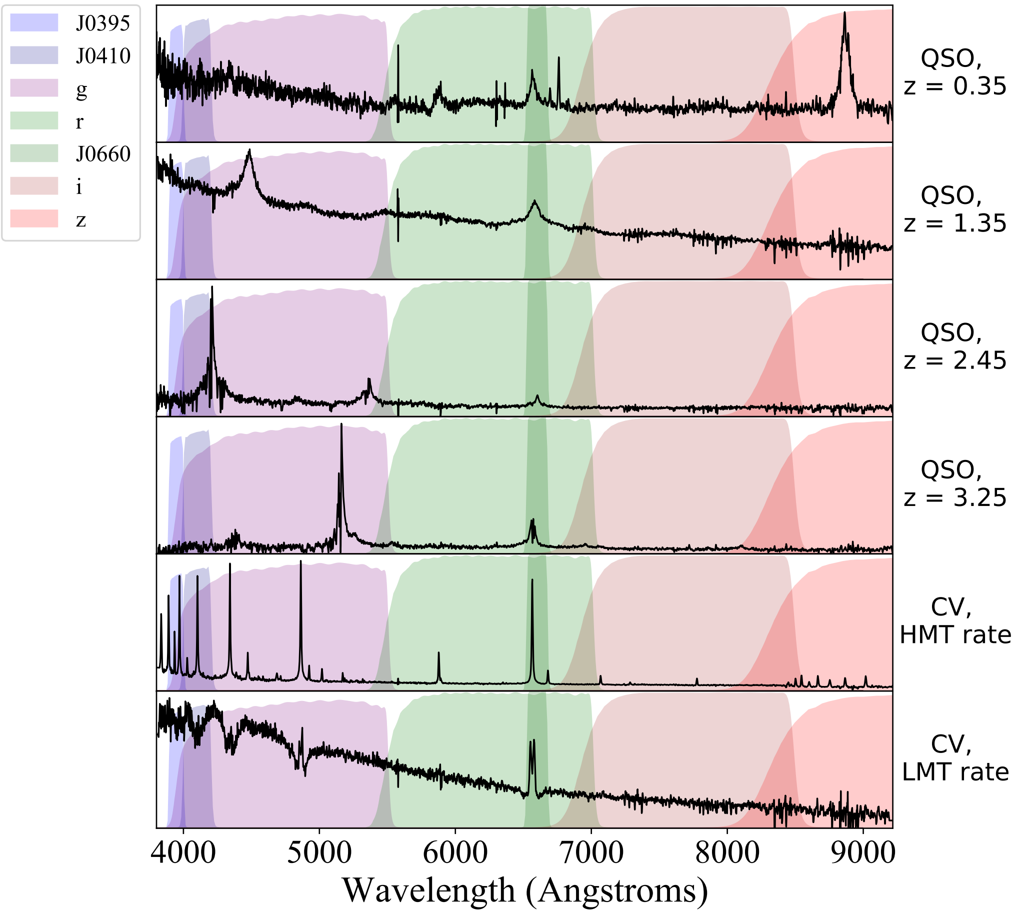

FIGURE 6.3: Comparative spectra of four QSOs at different redshifts at the top and two CVs at the bottom at high and low mass transfer rates. The QSO redshifts are selected so that an emission line lies in the Hα restframe. The filters of the J-PLUS survey are superimposed.

lines in such systems. Also interesting the HQS discovery of HS 2237+8154, a detached WD-RD whose orbital period is at the upper edge of the period gap (178 min) and donor is almost filling its Roche-lobe, (Gänsicke et al., 2004) suggest three evolutionary states, a pre-CV almost starting mass transfer, a CV entering the period gap which stopped the mass transfer recently or a hibernating nova.

The SDSS alonediscovered more than 400 new CVs (Szkody et al., 2002). This survey was designed to obtain a large photometric and spectroscopic data-base of galaxies and QSO. Notable are Szkody's CV discoveries based on colour methods (Papers I-VIII, Szkody et al. 2002, Szkody et al. 2003, Szkody et al. 2004, Szkody et al. 2005, Szkody et al. 2006, Szkody et al. 2007, Szkody et al. 2009, Szkody et al. 2011) who first used the bands u' and g' to separate CVs from main-sequence stars which, however, largely overlap with

QSO and WDs. Then they tried simultaneous blue and red criteria ending up with the following colour cuts:

- $u' - g' < 0.45$
- $g' - r' < 0.7$
- $r' - i' > 0.30$
- $i' - z' > 0.4$

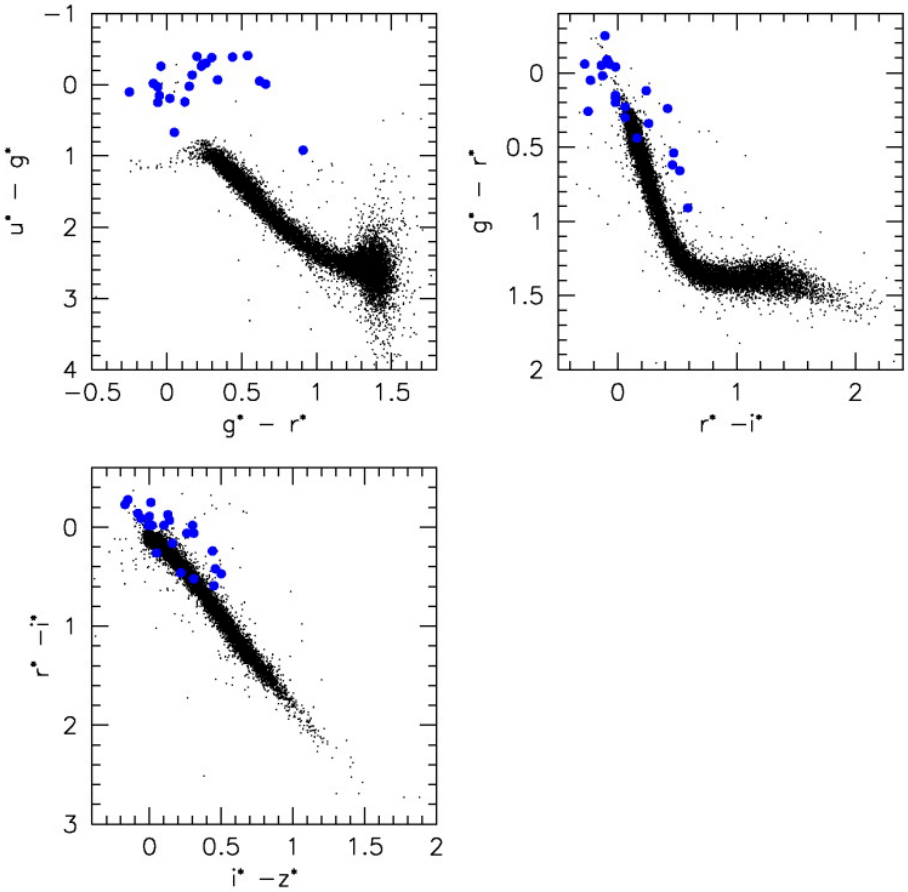

FIGURE 6.4: SDSS colour-colour plots for 22 objects. The filled circles are the CVs, while the dots are stars defining the stellar locus. Figure taken from Szkody et al. (2002)

Such criteria is able to select mostly non-interacting WD+M binaries and a few CVs, which used among the QSO candidates (primarily on candidates having near 0 redshift and broad hydrogen Balmer and helium emission lines) resulted in good performance with over 400 new discoveries. However and in spite of its success, the purity and completeness of the method are not known but expected to be low since such findings are biased towards broad hydrogen Balmer and helium emission lines. Moreover, it also implies a lot of manual work on the final discrimination, making a systematic search difficult to carry out.

Often, broad-band filters such as those from SDSS do not provide the necessary information to discriminate CVs efficiently and systematically but in contrast, recent surveys such as J-PLUS, provides information of a filter set comprised by narrow- and broad-bands which have been designed for stellar classification by situating some of them at key stellar spectral features.

6.3 Discriminating CVs from QSOs

6.3.1 Early data release

We first investigated the possibility to improve the method proposed by Scaringi et al. (2013), involving Hα excess and WISE colors. The idea is to develop a methodology to efficiently distinguish CVs from their main contaminants, QSO, in order to apply it to the whole population of punctual sources extracted from the J-PLUS survey and understand the biases produced to bear in mind in following steps.

Since the Hα emission line is usually the strongest spectroscopic feature in a CV, the relation between the *J0660* narrow band filter and the r filter is our starting point for their identification, particularly by high mass transfer rates CVs and whose spectral appearance is hence dominated by emission lines from the accretion disc.

As stated in the previous section, it is possible that, depending on the redshift, some QSOs will show emission lines in the $J0660$ filter, for example Hβ and HeI at redshifts $z \sim 0.35$ or CIV at $z \sim 3.25$ and therefore, a colour to measure the blueness of the object (i.e. $uJAVA - r$) allows us to get rid of QSOs at high redshifts and other hot objects showing emission in the Hα wavelength range. Low-mass transfer rate CVs let see the secondary in the infrared so combining the J-PLUS data with the WISE survey allow to discriminate them, mainly from QSO whose slope in the infrared should be negative (see also Scaringi et al. 2013). On the other hand, quasars at $z \sim 0.35$ can be confused with high mass transfer rate CVs. They shift Hα at around 8600Å and we use the i and $J0861$ bands located in this part of the spectrum (see Figure 6.3) for their discrimination.

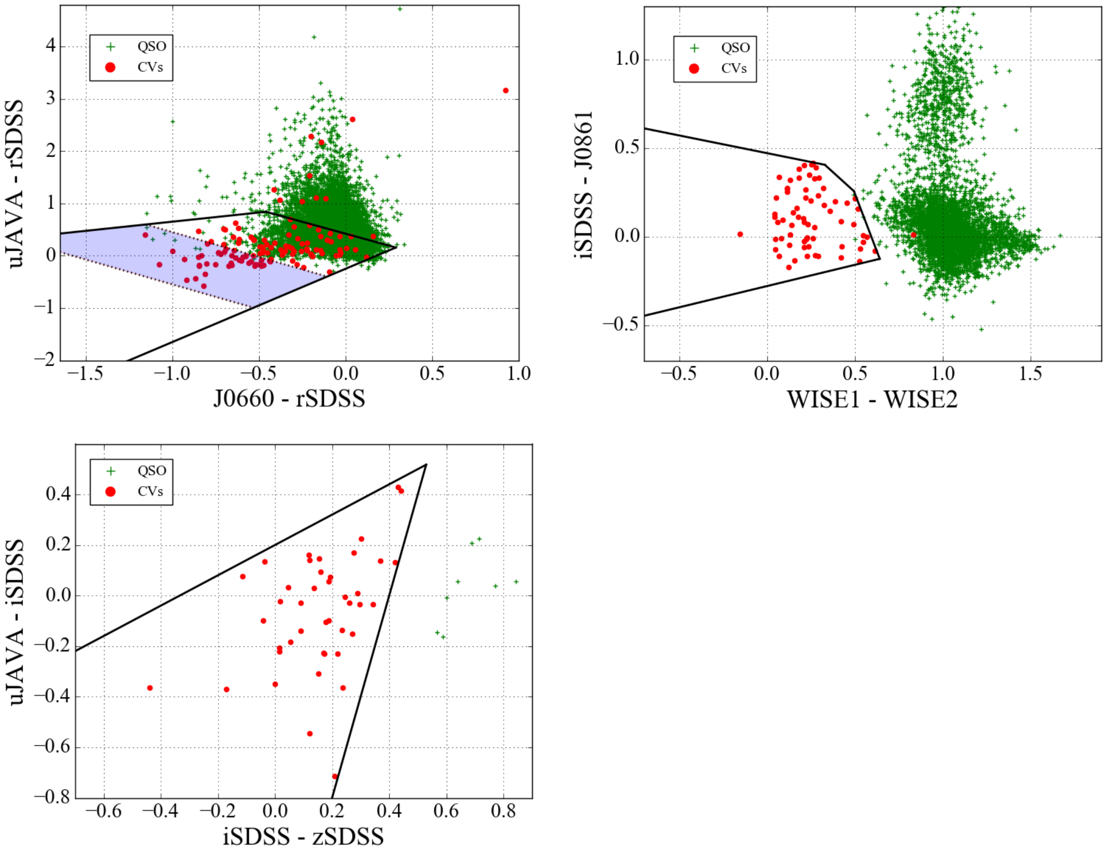

FIGURE 6.5: Three color-cuts devised to disentangle CVs from Quasars, the red dots are the CVs and the green crosses are the Quasars. Top-left panel shows the colour-colour diagram $J0660 - rSDSS$ vs $uJAVA - rSDSS$. The objects from the unshaded part are collected in the top right panel comparing $WISE1 - WISE2$ to $iSDSS - J0861$. Sources from the shaded part go to the bottom-left panel.

Top-left panel of Figure 6.5 shows the colour-colour diagram $J0660 - r$ vs $uJAVA - r$. Most of the CVs lie within the black borders due to the Hα emission combined with low $uJAVA - r$, but there are also two well-defined regions inside. The unshaded part contains low-mass transfer CVs and a big amount of QSOs of different redshifts. Top-right panel collects all these objects from the unshaded part on top left panel and compares $WISE1 - WISE2$ to $i - J0861$, all with the aim of detecting the secondary of the CVs whose spectra is not dominated by the disc, and nonexistent on QSOs, thus recovering the CVs. High-mass transfer CVs and some QSOs at very specific redshifts are located on the shaded part and bottom-left panel takes them. Since the higher the redshift the redder the spectrum, the contribution in the $uJAVA$ filter is small compared to redder regions of the spectrum and therefore, quasars at $z \sim 2.4$ and $z \sim 3.25$ are distinguishable using the $uJAVA - i$

colour (there are no synthetic QSOs at these values but there are some examples in Figure 6.6). Low redshift QSOs as $z \sim 0.35$ display higher $i - z$ colour than CVs since those have Hα redshifted to the z band.

To test the validity of this methodology, first we applied it to 9255 QSOs, selected as being classified as point-like sources, and 121 CVs whose spectroscopy was available from SDSS. After convolving them with the J-PLUS filter system and apply this methodology, we could recover 109 of the CVs, therefore obtaining a completeness of 90 %, and only 4 QSO contaminants.

Later, we checked the goodness of our method with real J-PLUS data, concretely with a first internal release of 150 deg^2 and more than 18000 objects cataloged as punctual sources, and with restrictions in magnitude and S/N, Figure 6.6. This time we recovered the 100% of the known CVs in it (7/7) and had 20 candidates/contaminants, 4 cataloged as QSOs, 3 as galaxies and 13 as stars.

It is noteworthy that several of these contaminant stars are binary systems composed by a WD and a MS star (period gap CV candidates) or a white dwarf and a brown dwarf (WD-BD, period bouncer CV candidates) and it seems we have strong candidates to help solving the still CV evolution discrepancies. The figure 6.7 shows two examples of period gap candidates, our methodology classifies them as CVs and the lack of emission lines, meaning they don't have accretion, makes them strong period gap candidates.

6.3.2 J-PLUS Data release 1

After the J-PLUS DR1 covering 1022 deg^2 of sky, we try to extend the colour-colour technique to a larger sample. Moreover, we also count with a larger and more heterogeneous CV sample observed in J-PLUS DR1 which was not available in the internal data release to test and understand our results. At this stage we develop three different methods, one only makes use of J-PLUS data so we can test the capabilities of J-PLUS alone to find new CVs. Its main advantage is the consistency of data since they all come from the same source. Also, missing data is very rare and in any case not comparable with combinations of two or more different surveys. In the other hand, this method obtains no information from the companion beyond the J-PLUS spectral range limit. Secondly, we try to improve the methodology from the previous section, which in turn tries to improve the method proposed by Scaringi et al. (2013) using infrared information from the WISE survey. Lastly, we add Gaia

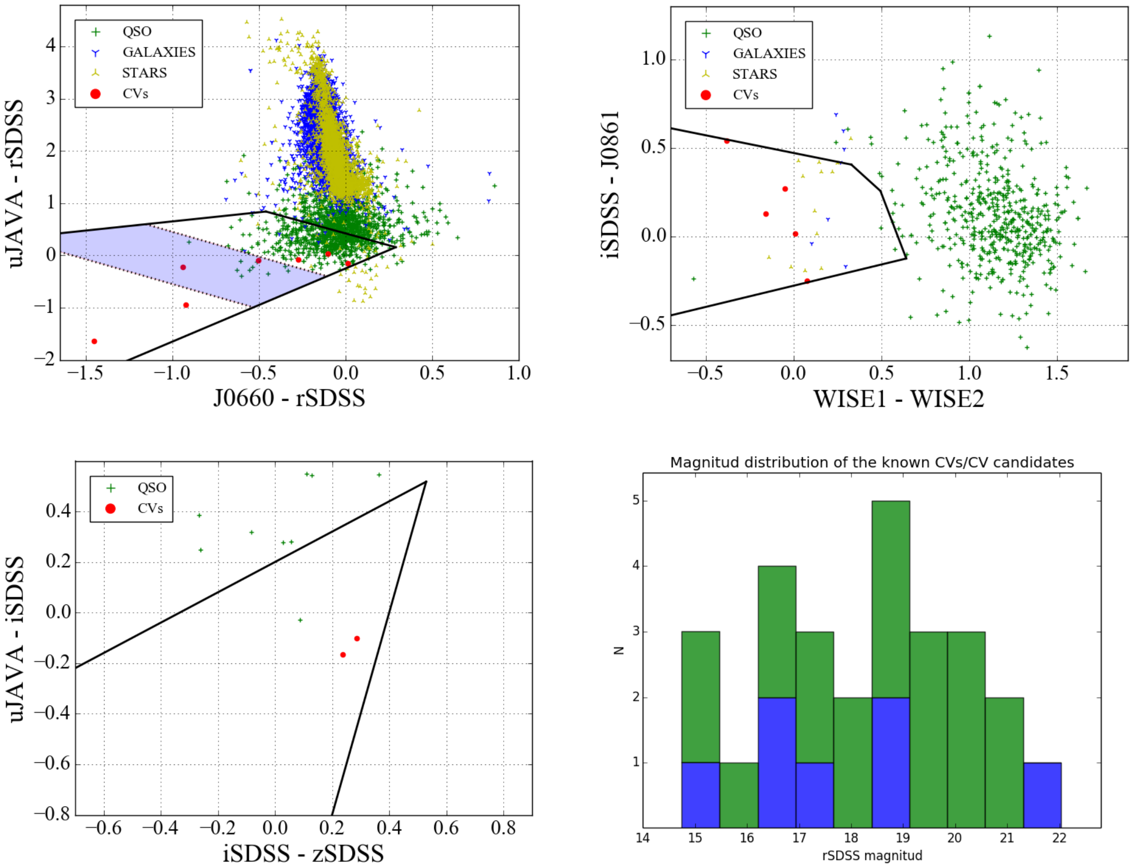

FIGURE 6.6: The three color cuts applied to the first 150 deg^2 of J-PLUS. The different symbols refer to the classification given by SDSS for objects with J-PLUS photometry. The objects falling in the shaded area in the left panel are evaluated again in the bottom-left one. The objects out of the shaded area but within the cuts are evaluated in the upper-right panel. The bottom-right panel shows the distribution in magnitude of the known CVs and candidates/contaminants, in total there are 20 CV candidates in green and 7 known CVs in blue, with magnitudes in the range between 15 and 22.

information deriving absolute magnitudes and finding the CV locus in the H-R diagram.

The *J0660-r* vs *J0395-g* colour-colour diagram acts as a base-line in the three methodologies we present here, allowing us to differentiate CVs from QSOs at a wide range of redshifts and most of the others point sources. Unlike in the previous section, we use *J0395-g* instead of *uJAVA-r* as the blue identifier due to several empirical experiments showing a better performance for the former. The broader *uJAVA* band is more prone to larger errors and in addition, more difficult to simulate for our synthetic sample. For the more

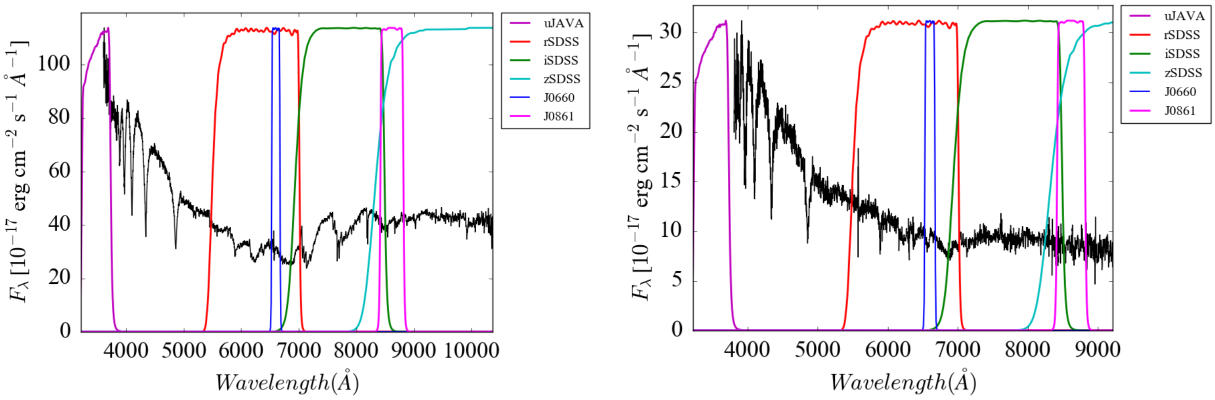

FIGURE 6.7: The figure shows two examples of period gap candidates, our methodology classifies them as CVs and the lack of emission lines, meaning they don't have accretion, makes them strong period gap candidates.

troublesome QSOs and other contaminants such as WD-MS binaries or hot stars, we use different approaches. The first one involves only J-PLUS data, the second one combines J-PLUS and WISE data, and the last one adds Gaia and the H-R diagram.

The strategy followed is the computation of a set of colour-colour diagrams to distinguish CVs from QSOs and then apply it to the entire J-PLUS DR1.

Method A: J-PLUS only

The presented methodology here only makes use of J-PLUS simulations and real data. For such purpose we use the 343 CV sample and a collection of 9376 QSOs. These QSOs are a sub-sample from SDSS-III (Alam et al., 2015) and are comprised by the sources that were observed spectroscopically and marked as point-sources by SDSS. They are representative of the whole population as they are distributed along a wide range of redshifts. Both the CV and the QSO spectra are convolved with the J-PLUS filter response curves.

However, as mentioned in section 6.1, we cannot compute the z synthetic photometry from SDSS spectra. The *i*-*z* colour is quite relevant to distinguish CVs from quasars using J-PLUS only, therefore in this case we use i' - z' instead, both from the SDSS survey, in order to keep consistency. The two bands, i' and z' are coincident with i and z from J-PLUS, see Table 4.1, and act as a good approximation.

The first diagram to be applied is the one displayed in Figure 6.8, it shows the *J0660-r* against *J0395-g* colour-colour diagram, the CVs are represented in green, QSO at redshifts between 0.3 and 0.4 in blue and the rest of QSO in gray. Negative values of *J0660-r* indicate the presence of Hα emission and the colour *J0395-g* is a measure of the blue slope of the SED, both being diagnostic features of CVs.

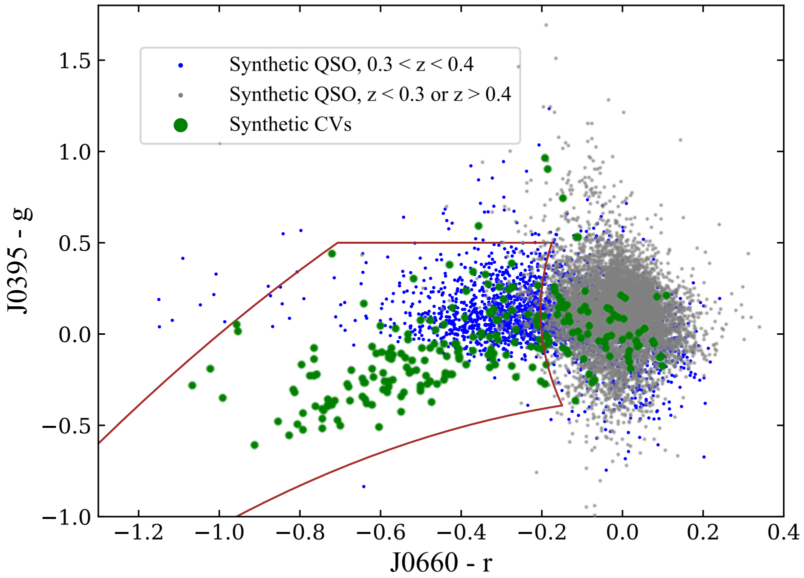

FIGURE 6.8: CVs in green, QSOs with redshifts between 0.3 and 0.4 in blue, rest of QSOs in gray. Most of the QSO contaminats are those within the redshift range 0.3-0.4 while a majority of the rest of QSO are well discriminated. The cuts applied are $x = -0.2 - 0.05y + 0.2y^2$; $y = -0.35 + 0.2x - 0.5x^2$; $y = 1.35 + 0.85x - 0.5x^2$ and $y = 0.5$.

Most of the QSOs lie outside the cuts, however a number of them (mainly those with redshifts between 0.3 and 0.4) still fall among most of the CVs. A portion of the CVs, 94 out of 343, also lie out of the bounds of the cuts. At this stage we focused on discarding most of QSOs with no emission in Hα and no big effort was invested in CV completeness.

Among the QSOs, our main contaminants are those at redshifts ∼0.35, ∼1.35, ∼2.45 and ∼3.25 whose emission lines fall into the *J0660* band (see Figure 6.3). The colour *J0395-g* discriminates well QSOs at redshifts ∼2.45 and ∼3.25 whose peak has been shifted beyond 4000 Å and a majority of QSO at redshifts ∼1.35, however it is not valid for redshifts ∼0.35. In order to get rid of these QSOs, and bearing in mind the QSO shape at this value of redshift from Figure 6.3, we see that Hα is shifted to the *z*-band making the colour *i′-z′* suitable to discriminate them as shown in Figure 6.9.

The *i′-z′* colour is compared against *J0410-J0395* with the aim of detecting the Hδ and Hϵ emission lines located there which are quite common among

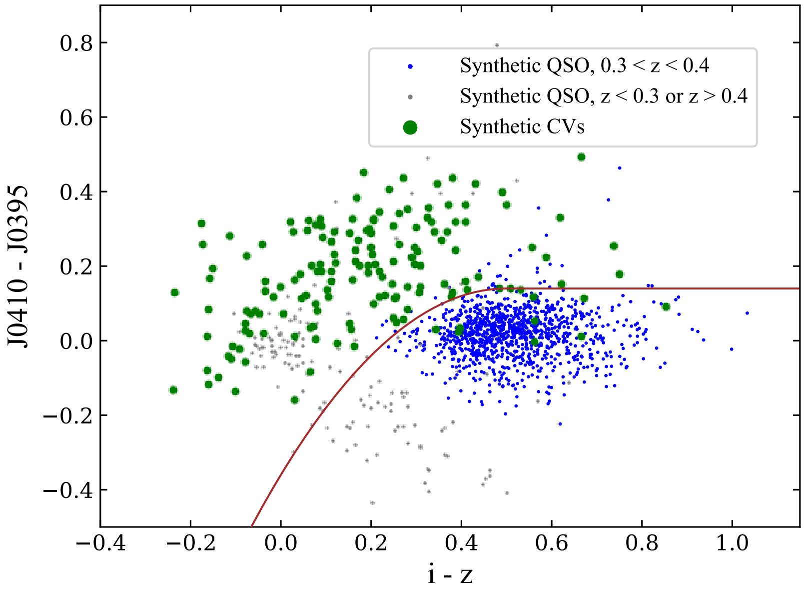

FIGURE 6.9: This diagram aims at discriminating QSO with redshifts within the range 0.3 and 0.4. These objects have Hα shifted to the z band making them distinguishable using the colour i'-z'. As opposed to QSO, the presence of Balmer lines in *J0410* and *J0395* for CVs make their distinction cleaner. A handful of QSO in gray (those around i'-z'=0 and *J0410*-*J0395*=0) remain as contaminants, they are QSO at $z \sim 1.35$. The cuts applied are $y = -0.36 + 2x - 2x^2$ for $x < 0.5$ and $y = 0.14$ for $x > 0.5$.

CVs and make their distinction cleaner. Table 6.1 summarizes the selection criteria results.

Subsequently, we apply these cuts to the whole J-PLUS DR1 after enforcing the quality constrains explained in Section 4.2.1 and we identify 630 CV candidates. From them, 133 have spectra in SDSS of which only 14 are CVs. Moreover, only 10 out of the 32 known CVs already observed in J-PLUS DR1 are recovered which yields a completeness of 43.5% and a purity of 10.5%, see table 6.2.

Investigating in more detail, we see that most of the contaminants are QSOs at redshifts around 1.35, where the magnesium spectral line is shifted to be detected in the *J0660* filter. There is no straightforward way to discriminate this kind of QSO since it does not show other recognizable features located in the J-PLUS filter set.

This methodology has the advantage of using only J-PLUS data. No cross-correlation with other catalogues is needed that might result in losing sources along the way. Thus, the data consistency is guaranteed, as well as the fact

Total number of initial QSOs	9256
of which z < 0.3 or z > 0.4	6712
of which 0.3 < z < 0.4	2544
Total number of initial CVs	343
QSOs after first cut	1142
of which z < 0.3 or z > 0.4	36
of which 0.3 < z < 0.4	1106
CVs after first cut	229
QSOs after second cut	56
of which z < 0.3 or z > 0.4	21
of which 0.3 < z < 0.4	35
CVs after second cut	215

TABLE 6.1: Summary table of method A using J-PLUS only for QSO-CV classification.

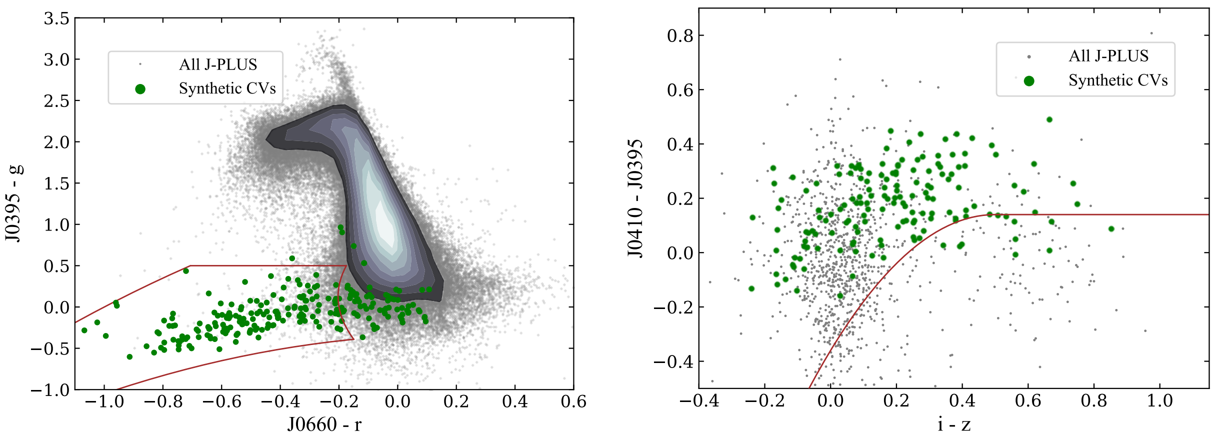

FIGURE 6.10: Method A. CVs in green, other sources in gray. Same diagrams and cuts computed for QSOs but applied to all J-PLUS DR1. Left panel is the equivalent of Figure 6.8 and the right one of Figure 6.9.

that the data for each source have been observed almost at the same time, which is important for variable objects. On the other hand, there is no clear way to get rid of a big majority of the contaminants. Although the colour-colour diagram *i′-z′* vs *J0410-J0395* is a good discriminator of QSOs at particular redshifts, it is not efficient for other QSOs and other point sources with emission at the Hα restframe. This weakness is quite evident when comparing Figure 6.9 showing the cut for QSOs and the right panel of Figure 6.10 where all J-PLUS DR1 sources are evaluated and the cuts barely separate CVs from other sources.

Total number of sources in J-PLUS DR1	$\sim$ 13.4 mill.
Sources after quality filtering	958665
Sources after first colour-colour diagram	922
Sources after second colour-colour diagram	630
of which with SDSS spectra available	133
of which catalogued as CVs by SDSS	14
Observed CVs from Ritter&Kolb / Downes	32
after quality filter	23
after first colour-colour diagram	12
after second colour-colour diagram	10
Completeness of the method	43.5%
Purity of the method	10.5%

TABLE 6.2: Summary table of method A using J-PLUS only and applied to all J-PLUS DR1.

Method B: J-PLUS and WISE

In this section we approach the QSOs distinction by crossing our J-PLUS data with WISE, thus investigating the possibility to improve the method proposed by Scaringi et al. (2013). The purpose of using WISE is due to the presence of dust in QSOs which should appear as an excess of flux in the infrared. In this case therefore, we can afford enlarging our boundaries in the *J0660-r* vs *J0395-g* diagram (Figure 6.8) including a larger sample of CVs. This is particularly useful for those CVs with weak Hα emission that are mixed up with the QSOs in this part of the diagram (*J0660-r* $\sim$ 0.0).

Therefore, we substitute the second diagram in the previous methodology for one based on WISE. For that purpose, we cross the objects passing our first selection criteria with WISE, and compute the diagram *WISE1-WISE2* vs *i-WISE1* which has already been successful discriminating WD-MS stars from QSO (Rebassa-Mansergas et al., 2013), also, a similar combination of colours has been used to distinguish D-type Symbiotic stars and PNe which are also Hα emitters and posses a WD, YSO, and TTauri stars, or hot stars like Be and Wolf-Rayet stars (Akras, Guzman-Ramirez, and Gonçalves, 2019). It is represented in Figure 6.11, for QSOs only (top) and all J-PLUS DR1 (bottom).

The diagram based on WISE discriminates QSOs quite well, including those with redshifts around 1.35 that could not be discarded by the first method. As shown in table 6.3, we obtain 927 candidates, of which 133 have spectra in SDSS and 23 are catalogued as CVs. We also recover 15 CVs from those already observed with J-PLUS yielding a completeness of 65% and a purity of 17%. Therefore, even at the cost of losing 18% of the sources due to

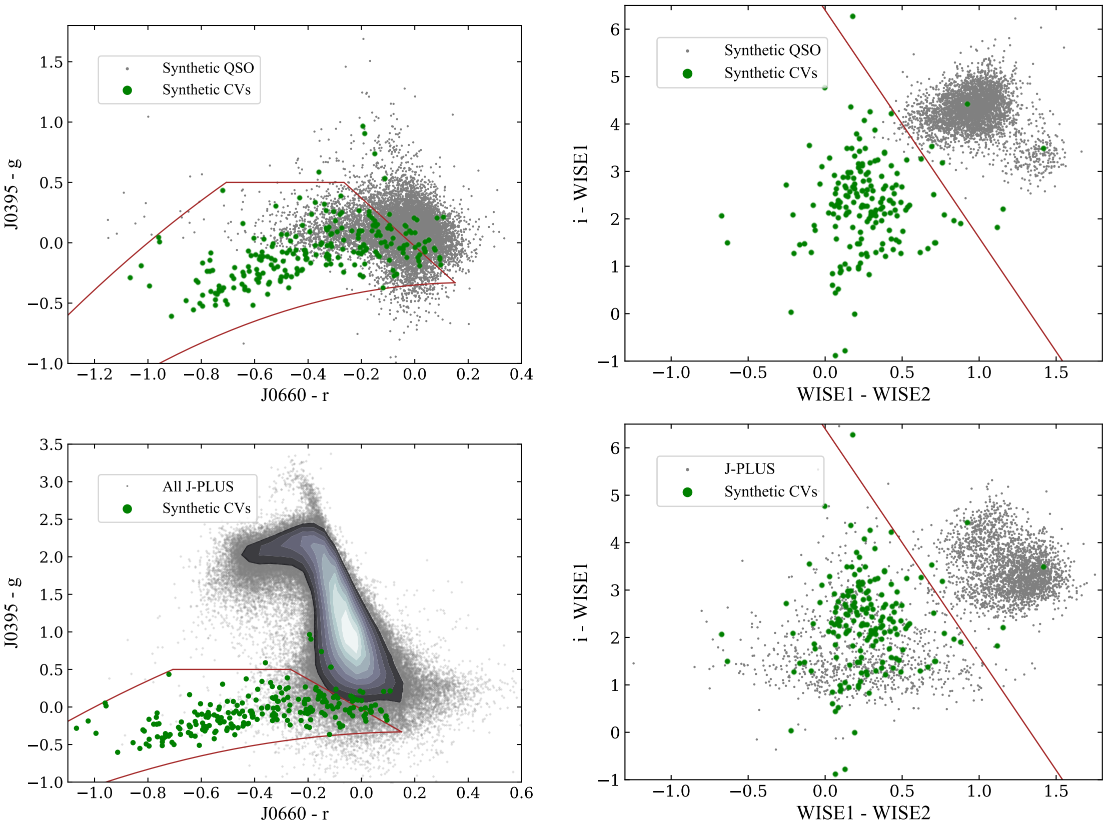

FIGURE 6.11: Method B. At the top the cuts applied to the QSO sample and at the bottom applied to all J-PLUS. The *J0660-r* vs *J0395-g* diagrams include an extra region with respect to the first methodology where CVs with little Hα emission are expected to lie, the cuts applied are $y = -0.35 + 0.2x - 0.5x^2$; $y = 1.35 + 0.85x - 0.5x^2$; $y = -0.03 - 2x$ and $y = 0.5$. *WISE1-WISE2* vs *i-WISE1* diagrams are designed to discriminate QSO by detecting their surrounding dust. The cut used in this case is $y = 6.4 - 4.8x$.

the cross-match with WISE, we improve our completeness and purity with respect to the method presented above.

Unlike with the previous methodology, among our contaminants very few are QSOs. Instead, they mainly comprise WD-MS and hot stars.

Method C: J-PLUS, WISE and Gaia

In this case, Gaia and its derived estimated distances (r_{est}) from Bailer-Jones (see section 5.1.1), serve as a delimiter for Galactic and non Galactic objects and, for our work purpose, as a good discriminator for QSOs. Therefore, we filter our sample by $r_{est} < 1200$pc, this value has been chosen in order to minimise the CV loss while maximising the QSO discrimination. As shown

Total number of sources in J-PLUS DR1	$\sim$ 13.4 mill.
Sources after quality filtering	958665
Sources after first colour-colour diagram	4392
Sources after crossing with WISE	3601
Sources after second colour-colour diagram	927
of which with SDSS spectra available	133
of which catalogued as CV by SDSS	23
Observed CVs from Ritter&Kolb / Downes	32
after quality filter	23
after first colour-colour diagram	18
after crossing with WISE	16
after second colour-colour diagram	15
Completeness of the method	65%
Purity of the method	17%

TABLE 6.3: Summary table of method B using J-PLUS and WISE photometry and applied to all J-PLUS DR1.

in Figure 6.12, 79% of the CVs have $r_{est} < 1200$ pc and only 6% of objects classified as QSOs are below this threshold.

Furthermore, as stated several times, CVs are composed of a WD and a MS star. Hence, CVs are expected to lie somewhere in between the WDs locus and the MS path in the well known H-R diagram, depending on the temperature and size of both WD and MS star. However, in many systems also the accretion disc contributes to, or even dominates, the brightness of binaries. In these cases, the mass-transfer rate, the magnetic activity of the WD, and the inclination of the system will influence their position in the diagram (Warner, 1986).

In this methodology we also use what was learnt from the previous one and we implement the WISE based colour-colour diagram, however we only apply it to the "triangle" at the right of the dashed line within the cuts (what we refer to, in Figure 6.13, as area B) as a middle step towards the H-R diagram using Gaia. We do not apply it to the whole area due to the large loss of sources at the junction with WISE. However, it is efficient for CVs with weak Hα emission (which are expected to lie in this small area) where the higher recovery ratio offsets the loss of sources due to the cross-match with WISE.

This scenario is represented in Figure 6.13. First we test our base-line diagram *J0660-r* vs *J0395-g*, including this added area from the previous methodology which, due to the application of the cut in distance (estimated distance < 1200 pc) is less contaminated. We evaluate only this added area with the

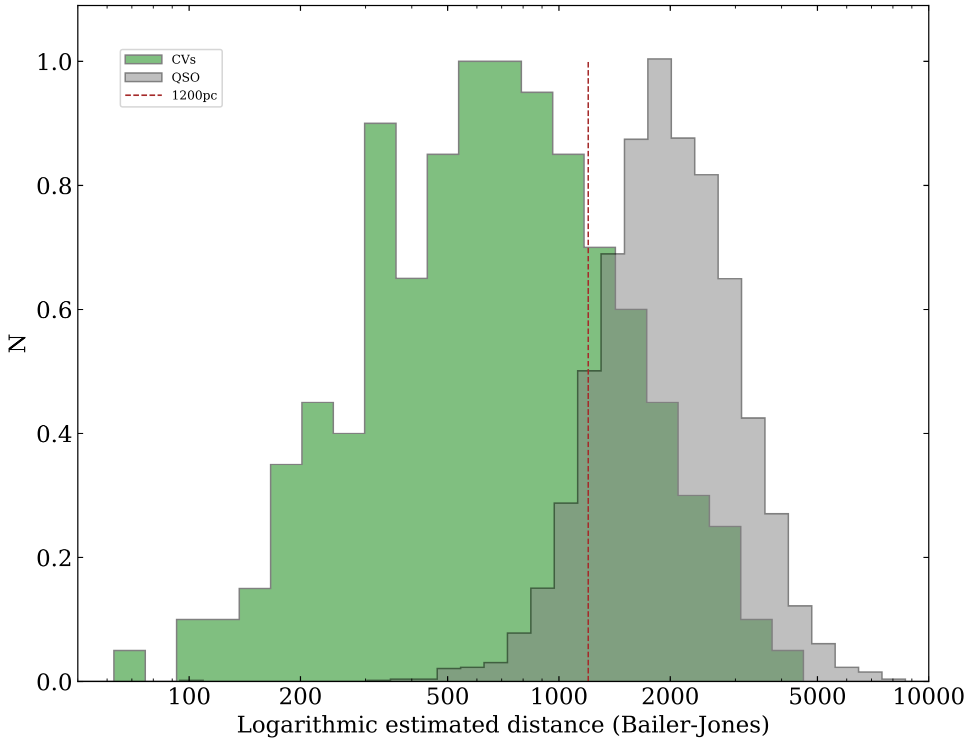

FIGURE 6.12: Histogram showing the proportion of objects classified as QSO and CVs by their estimated distances. The dashed line is at 1200 pc. 79% of the CVs have $r_{est} < 1200$ pc and only 6% of QSOs are below this threshold.

WISE1-WISE2 vs *i-WISE1* diagram. Finally, we verify that our remaining objects lie in the CV locus on the H-R diagram. Obtaining a final sample of 146 candidates, of which 42 already have available spectra in SDSS yielding 104 objects as candidates. As can be seen from Table 6.4, this last methodology has a completeness of 74% and a purity of 31%, representing a significant improvement over the previous exercises.

Follow-up spetroscopic observations of the candidates obtained by this methodology has been done using OSIRIS in the GTC telescope. Appendix B shows the reduced spectra of 12 of the observed sources (those with enough quality).

Total number of sources in J-PLUS DR1	$\sim$ 13.4 mill.
Sources after quality filtering	958665
Sources after first colour-colour diagram	4386
of which in the area A	1123
of which in the area B	3263
Sources from A after crossing with Gaia	1113
with estimated distance < 1200 pc	95
Sources from B after crossing with WISE	2519
after second colour-colour diagram	657
after crossed with Gaia	648
with estimated distance < 1200 pc	69
Total sources within cuts in H-R diagram	146
of which with SDSS spectra available	42
of which catalogued as CV by SDSS	13
Observed CVs from Ritter&Kolb / Downes	32
after quality filter	23
after first colour-colour diagram	18
of which in the area A	13
of which in the area B	5
Total known CVs recovered	17
Completeness of the method	74%
Purity of the method	31%

TABLE 6.4: Summary table of method C using J-PLUS and WISE photometry plus Gaia parallaxes and applied to all J-PLUS DR1. Area A refers to the left side of the dashed line within the cuts on the left panel of Figure 6.13 and area B to the right one.

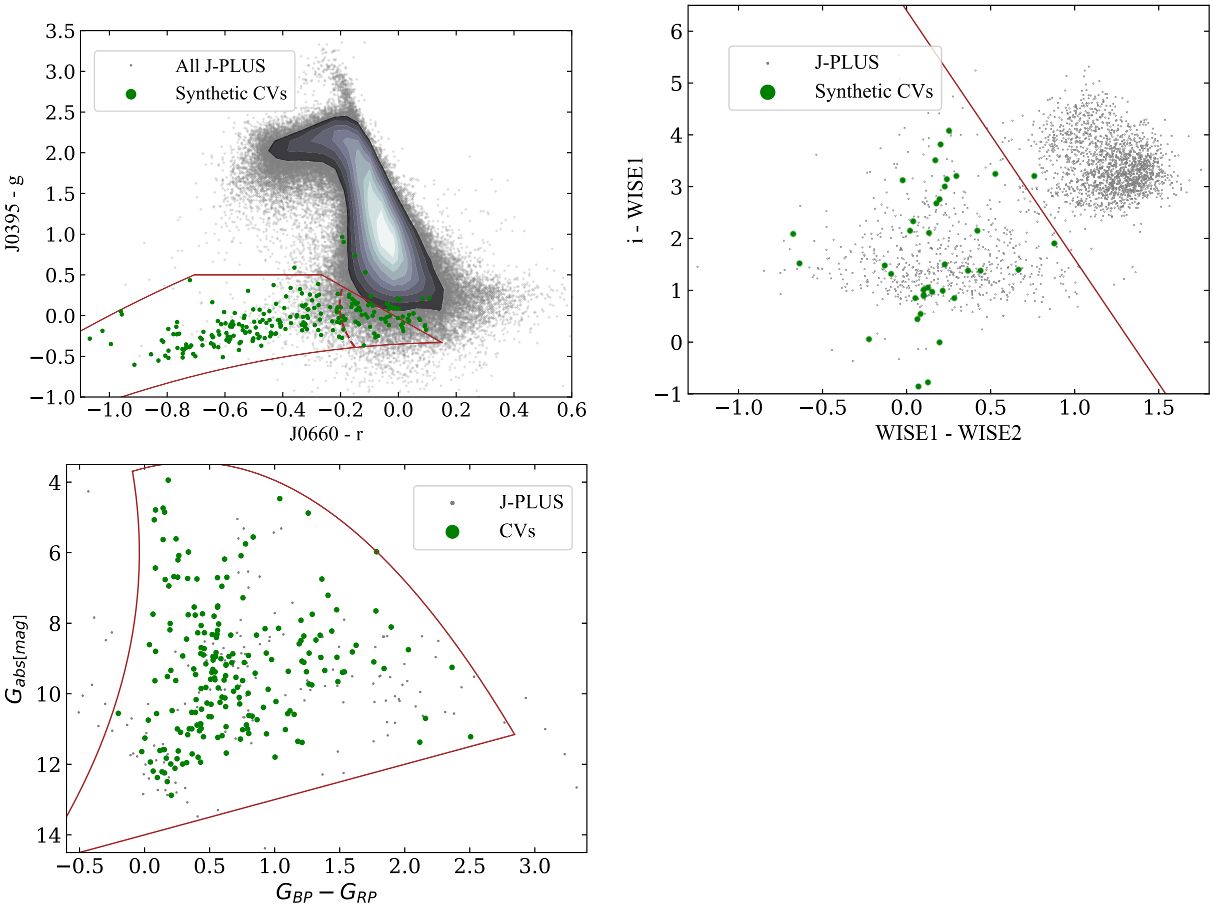

FIGURE 6.13: The methodology C applied to the 1022 deg^2 DR1 of J-PLUS. CVs in green, rest of objects in gray. In the top-left panel the cuts are the same as the equivalent diagrams from the previous methodology (see Figure 6.11) plus the dashed line ($x = -0.2 - 0.05y + 0.2y^2$) that delimits two regions, area A at the left and area B at its right. Here, we look for Hα excesses (*J0660-r*) combined with bluer shapes (*J0395-g*). Those objects with not so strong Hα excess lie in the area B and are evaluated in the top-right panel making use of WISE. The presence of dust in QSO mainly, but also in other objects make them appear with stronger excesses in this range of wavelength compared with CVs. Finally, all objects from area A in the left panel as well as those above the cut ($y > 1.9 + 1.7x$) in the middle one are evaluated in the H-R diagram at the right of the figure. The region within the cuts corresponds to the CV locus, located between the main sequence path and the WDs. The boundaries applied in the H-R diagram are $x = -0.4 + 0.12y - 0.01y^2$; $y = 3.6 - 0.9x + 1.25x^2$ and $y = 14 - x$.

Chapter 7

Machine learning techniques and data imputation

In this chapter we try to solve the problems associated with the more classic methodologies presented in the previous one by using machine learning (ML) techniques. ML algorithms are built based on sample data, known as "the training dataset". It aims at making predictions, classifications or decisions without being explicitly programmed to do so. The training dataset is usually labelled (supervised learning)[1], the algorithm is presented therefore with the sample inputs and their desired outputs, and the goal is to learn a general rule that maps inputs to the outputs to apply on the unlabelled samples to predict or classify.

The colour-colour and colour-magnitude diagrams from previous chapters are not easy to deal with missing data and the typical approach is to discard such data from the trainning, with the consequent loss of information and decrease of completeness. In addition, cutting criteria tend to be subjective and do not usually capture the more subtle patterns that other less obvious colour combinations may provide.

Conversely, if there are no intrinsic biases in the data used, ML techniques can provide objective results by capturing less noticeable patterns. A comparison of different ML techniques to predict missing values mainly derived from cross-matching data between different surveys is presented. Subsequently, this new dataset with the imputed data is used to retrieve CVs from J-PLUS, WISE and Gaia data.

---

[1] There are two more branches of ML techniques; *Unsupervised learning*, which makes use of an unlabelled training dataset and groups samples in clusters with common properties previously unknown, and *Reinforcement learning*, a decision making-oriented set of techniques, which finds patterns through feedback in the form of rewards.

7.1 Imputation of missing values

Dealing with missing values is a field of extensive research in ML. Data in real world are rarely homogeneous and they tend to be incomplete. This is also the case in astronomy where very often different surveys are crossmatched, one containing information of a given source while the other does not, or also within a single survey which lacks values for some of the variables.

Besides, many ML algorithm implementations do not support missing data and a broad approach is ignoring such missing values and only consider observations where all variables are observed. However it comes at the cost of having less data which may be valuable, leading to poorer performance and, depending on the underlying mechanism that generates missing data (see Section 7.1.1), to biased results.

7.1.1 Underlying missing data mechanisms

There are three typical mechanisms causing missing data and deciding how to handle missing data on a particular data-set is highly dependant on the mechanism that generates such missingness.

- *Missingness completely at random (MCAR).* This mechanism occurs when there is no relationship between the missing data and any values. All values have the same probability of missingness. In this case, discarding cases with missing data does not cause biases since the remaining are representative of the entire data-set.
- *Missingness at random (MAR).* There is a systematic relationship between the missing values and the observed data, but has no relationship with unobserved variables.
- *Missingness not at random (MNAR).* In this situation missingness is not only dependant on other observed variables but also on unobserved ones.

MAR and MNAR are typical cases in astronomy where the missingness depends on the faintness of a source which is highly related with other recorded variables such as the flux of observed bands. However, it could also be related with other typically unrecorded variables such as the variability of a source, its type or its state at a given moment. For example, in our case of study we intend to find CVs using the *J-PLUS* photometry as the base-line where we do not have missing values. Nonetheless, we also make use of *WISE* and *Gaia's* photometries which contain missing values. Since *Gaia's* data is derived from its bands that overlap with *J-PLUS's* ones, we can assume that missingness is related with faint fluxes in the *J-PLUS* bands and therefore follow MAR mechanisms. This logic also applies to *WISE*, however, and since these are infrared observations that do not overlap with *J-PLUS*, missingness may also be related to the type of source that might be bright enough for J-PLUS but not enough to be observed in the infrared and thus, following a MNAR mechanism.

7.1.2 Data imputation methods

Although there are countless ways to approach missing data, we here only describe and after compare performances in our data-set for a subset of them:

- *Discarding data.* This is the most common method when using ML algorithm implementations that does not allow missing data, however is only acceptable when the number of observations is large enough so performance is not compromised and missingness is MCAR, otherwise these approaches lead to biased estimates. Main discarding data methods are list-wise deletion; where all observation with missing data are removed completely, pairwise deletion; only the missing values are ignored, this case is less biased and sometimes can be used for MAR mechanisms, however many ML implementations does not support it, dropping variables; when there are too many data missing for a given variable.

- *Univariate imputation.* The imputed values are deduced using only non-missing values of that variable. Examples of univariate methods replace the missing values with the mean, the median or the mode of that variable. For non-MCAR mechanisms, these methods also lead to inconsistent biases, especially in the presence of great inequality missingness among the variables.

- *Multivariate imputation.* Multivariate imputation algorithms use the entire set of variables to estimate the missing values. They often get better guesses if there is a correlation between the missing values and other variables. Besides, several multivariate imputation methods, such as Multiple Imputation and Maximum Likelihood, although assuming MAR mechanisms, are often unbiased with MNAR.

Among the multivariate imputation methods there exist two different approaches, multiple imputation (MI) and single imputation (SI). MI involves filling in the missing values multiple times creating "m complete" data-sets whose missing values estimates differ from each other. Such differences, usually coming from the randomness introduced by the estimator used, allows to account for uncertainties in the imputations whereas SI do not account for the uncertainty in the imputations, leading to overly accurate results and potential incorrect conclusions. In this work we apply MI technique since understanding uncertainties is crucial in order to evaluate its implications and goodness.

7.1.3 Evaluating imputation techniques

Evaluating imputation techniques is not straightforward because very often it is difficult to understand what mechanism controls the absence of data and even knowing it, due to the fact that we do not have such data, it is difficult to know how well they fit the reality.

Our data-set described in section 4.2 has been selected to contain all data in the J-PLUS bands, however their cross-match with Gaia and WISE, yields a considerable amount of missingness on these latter surveys. Table 7.1 shows the amount of missing values on each band[2], pair of bands and the three of them. When a value is missing in $WISE2$ almost always is missing as well on $WISE1$, however there is little overlap between Abs. mag.(r) and the WISE ones, which could mean that the variables related to the missingness mechanism are different and/or are the missingness mechanisms themselves.

The approach we use is selecting a subset containing 200000 random instances where there are no missing values in none of the surveys used. Subsequently, we remove a set of values maintaining the missingness ratio of the complete dataset from Table 7.1. We carried out this process twice, first at random to simulate a MCAR mechanism and then we use the original full data-set to train a Gaussian Naïve Bayes algorithm to predict and after remove the instances which are most likely to contain missing values in one or more variables (in our case $WISE1$, $WISE2$ and Abs. mag.(r)), thus keeping the missingness correlation among variables as in the original data-set and therefore simulating a MAR mechanism.

---

[2] Unlike the datasets used in 5.2 and 6.3.2 where we computed the absolute magnitude for the Gaia G band, in this chapter the J-PLUS r band is computed and used instead, which we refer to as Abs. mag. (r). The variables in our dataset with missing values are $WISE1$, $WISE2$ and Abs. mag. (r) itself.

Band(s)	Total missing values	Proportion from the total (%)
Abs. mag.(r)	8678	0.91
$WISE1$	90664	9.46
$WISE2$	162879	16.99
Abs. mag.(r), $WISE1$	744	0.08
Abs. mag.(r), $WISE2$	1257	0.13
$WISE1$, $WISE2$	90039	9.39
Abs. mag.(r), $WISE1$, $WISE2$	741	0.08

TABLE 7.1: Amount of missing data on each band, each pair of bands and the three of them. The numbers shown are absolute values, it means, if an object has missing data in Abs. mag.(r) and $WISE1$ but not in $WISE2$, it counts for Abs. mag.(r) and $WISE1$ individually but also for the pair Abs. mag. (r), $WISE1$.

We then present the obtained errors with respect to the real values in a comparison of 2 SI estimators, Bayesian Ridge (BR)[3] and K Nearest Neighbors (KNN)[4] and 3 MI estimators with 10 iterations each, K Neighbors Regressor (KNR), Random Forest Regressor (RFR)[5] and Extra Trees Regressor (ETR)[6] for both the MCAR and MAR approaches, and for reference, we also compare the MAR mechanism with an Univariate Imputation method using the mean.

The purpose of applying these two simulations (MCAR and MAR) is to obtain an error estimate to illustrate the importance of choosing the appropriate underlying missingness mechanism and also show the tendency of the errors.

Figures 7.1 and 7.2 show the error distribution of the predictions for each estimator with respect to their magnitudes, both for the MCAR and MAR mechanisms. The former MCAR mechanism simulation shows a uniform distribution of missing data along the magnitude axis, which is expected since the missing values were chosen randomly, whose errors increase as the magnitude gets higher for all estimators used.

In contrast, the latter MAR mechanism simulation whose missing values were predicted by a Gaussian Naïve Bayes algorithm[7] trained in the whole dataset, concentrate the missing values at higher magnitudes for $WISE1$ and

---

[3] BR estimates a probabilistic model of the regression problem. The prior for the coefficient is given by a spherical Gaussian.

[4] A non-parametric method used for classification and regression. In both cases, the input consists of the k closest training examples in the feature space.

[5] A meta estimator that fits a number of classifying decision trees on various sub-samples of the dataset and uses averaging to improve the predictive accuracy and control over-fitting.

[6] Similar to RFR but it uses tree-cuts randomly to improve variance.

[7] Naive Bayes classifiers are a family of simple "probabilistic classifiers" based on applying Bayes' theorem with strong (naïve) independence assumptions between the features.

$WISE2$. This scenario is more realistic since a higher missingness ratio for fainter objects is expected. The errors are centered around Abs. mag. $r \sim 4$, one magnitude brighter than for the MCAR simulation. This can be explained by the fact that such intrinsically brighter objects with high apparent magnitudes are more distant objects, therefore producing larger parallax errors and higher probability of missingness.

Figure 7.3 shows the errors simulating a MCAR mechanism. This can be the case for some sources whose missingness is not related with the source itself or related with a technical issue, for example, the non-overlap between surveys. In other words, that a source was placed within one survey coverage but not in the other can be considered as completely at random. RFR is the algorithm yielding the best results comparing the imputed values with respect to the real, previously extracted ones. Its probability distribution function (PDF) is quite symmetrical with mean errors of -0.00111 mags. ($\sigma = 0.1434$), 0.00091 mags. ($\sigma = 0.0765$) and 0.00281 mags. ($\sigma = 0.1049$) for Abs. mag. r, $WISE1$ and $WISE2$ respectively.

Figure 7.4 shows the errors simulating a MAR mechanism. It is assumed that most of the missing values are caused by this mechanism, which, for example, implies missingness due to their intrinsic brightness or its overlap with other sources. In this case ETR provides the more accurate results. $WISE1$ and $WISE2$ PDFs are quite symmetrical, Abs. mag.(r) PDF has positive skewness and their errors much larger than for MCAR. They have mean errors of 0.14341 mag. ($\sigma = 0.2759$), 0.01982 mag. ($\sigma = 0.2134$) and -0.04955 mag. ($\sigma = 0.2909$) for Abs. mag.(r), $WISE1$ and $WISE2$ respectively. Since this last mechanism is the one closer to the real scenario, the ETR is the algorithm applied to the whole dataset which will be used to find CVs by applying ML techniques, more concretely, a Neural Network.

Furthermore, for the MI approaches, further analysis can be run. Rubin's rule (Rubin DB. Multiple Imputation for Nonresponse in Surveys. New York: John Wiley and Sons; 2004.) combines each imputed dataset into an overall MI estimate and associated Standard Error (SE). After obtaining the mean over all the imputations as the overall MI estimate, $\bar{Q} = \frac{1}{m}\sum_{i=1}^{m}\hat{Q}$, the overall variance of the point estimate is a combination of within-imputation and between-imputation variances (Marshall et al. 2009). The associated total variance for this overall MI estimate is

$$T = \bar{U} + (1 + \frac{1}{m})B \tag{7.1}$$

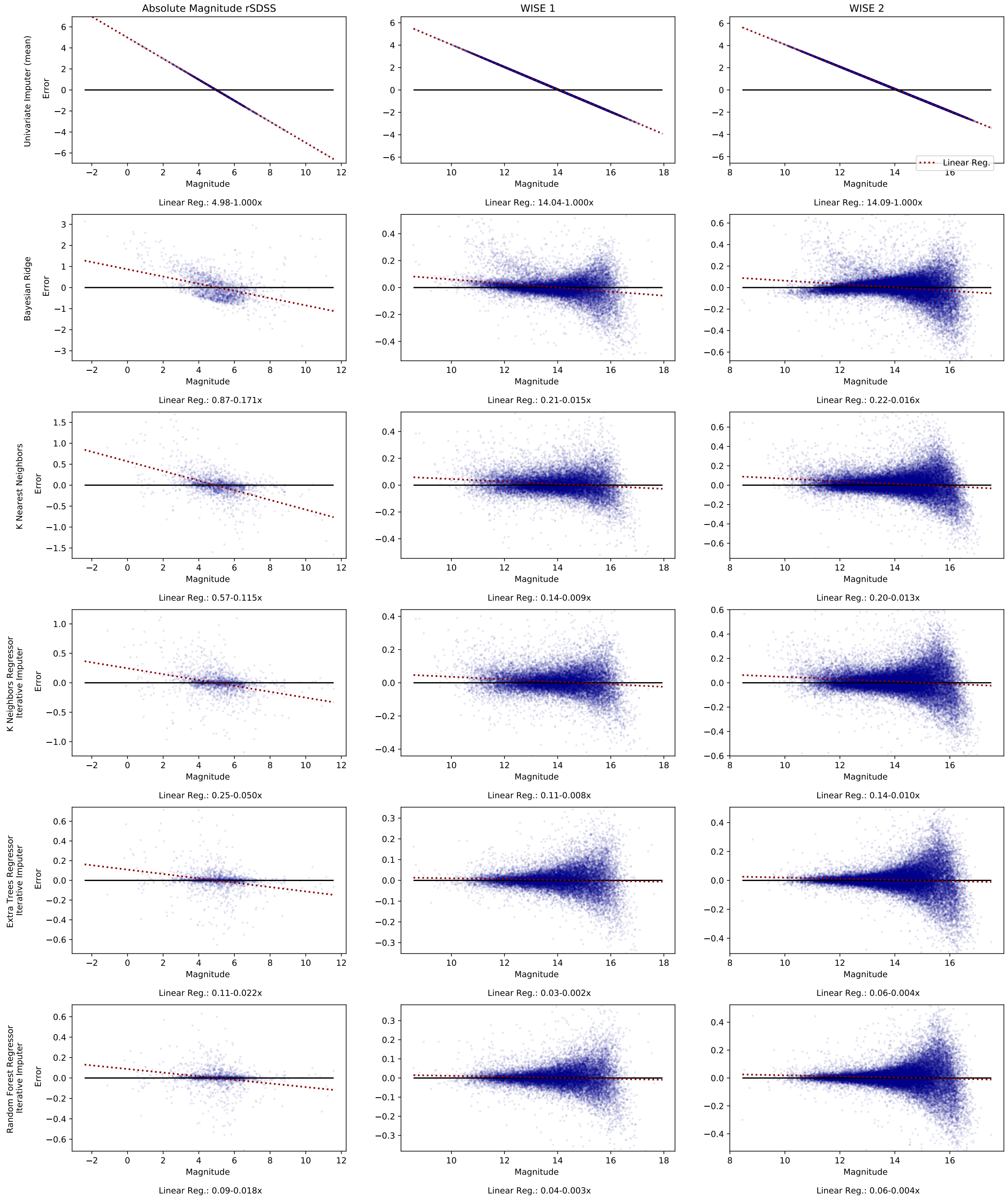

FIGURE 7.1: The error distribution with respect to the magnitude. Errors (predictions substracted from the real values) and their standard deviation for the MCAR mechanism simulation.

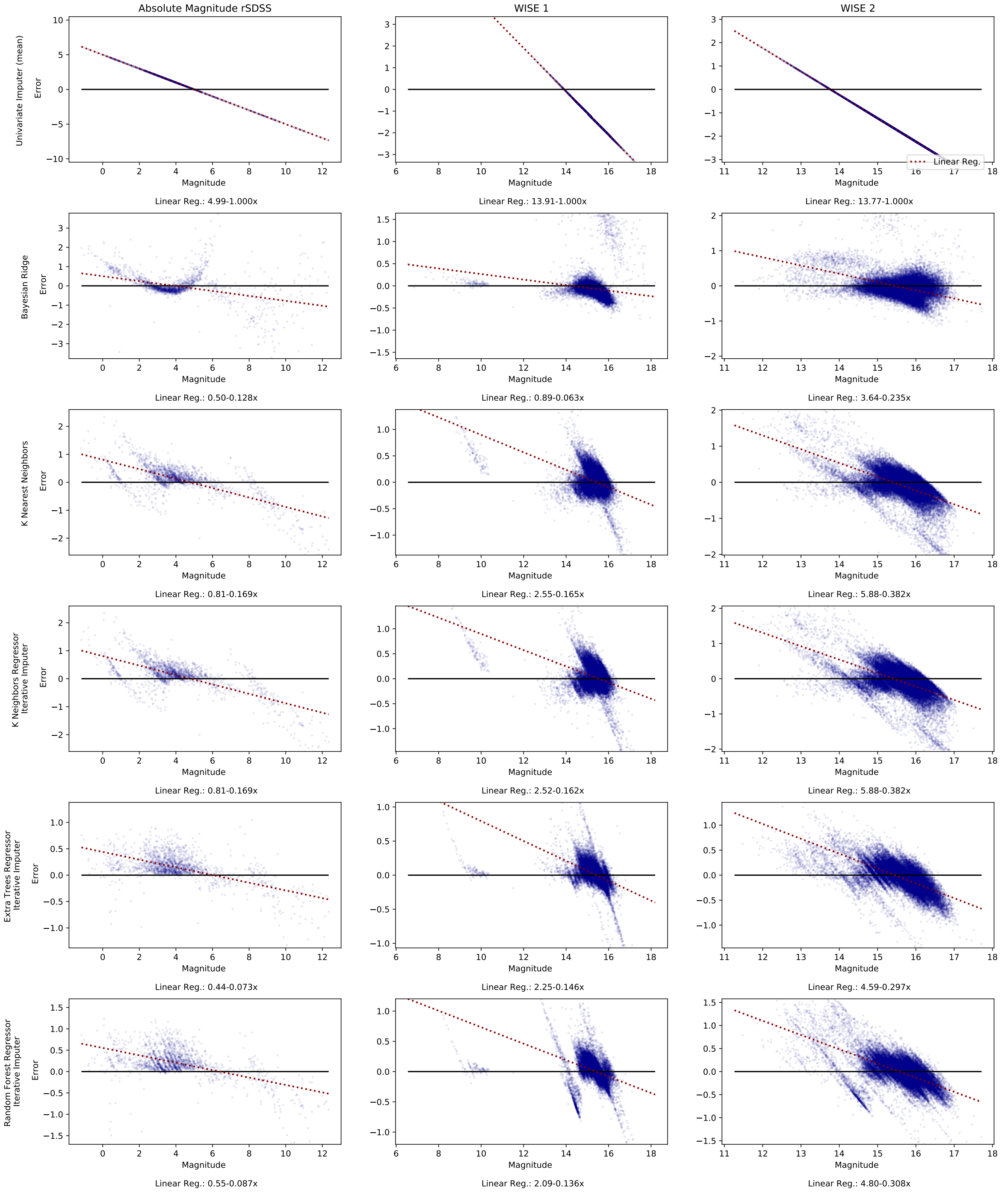

FIGURE 7.2: The error distribution with respect to the magnitude. Errors (predictions substracted from the real values) and their standard deviation for the MAR mechanism simulation.

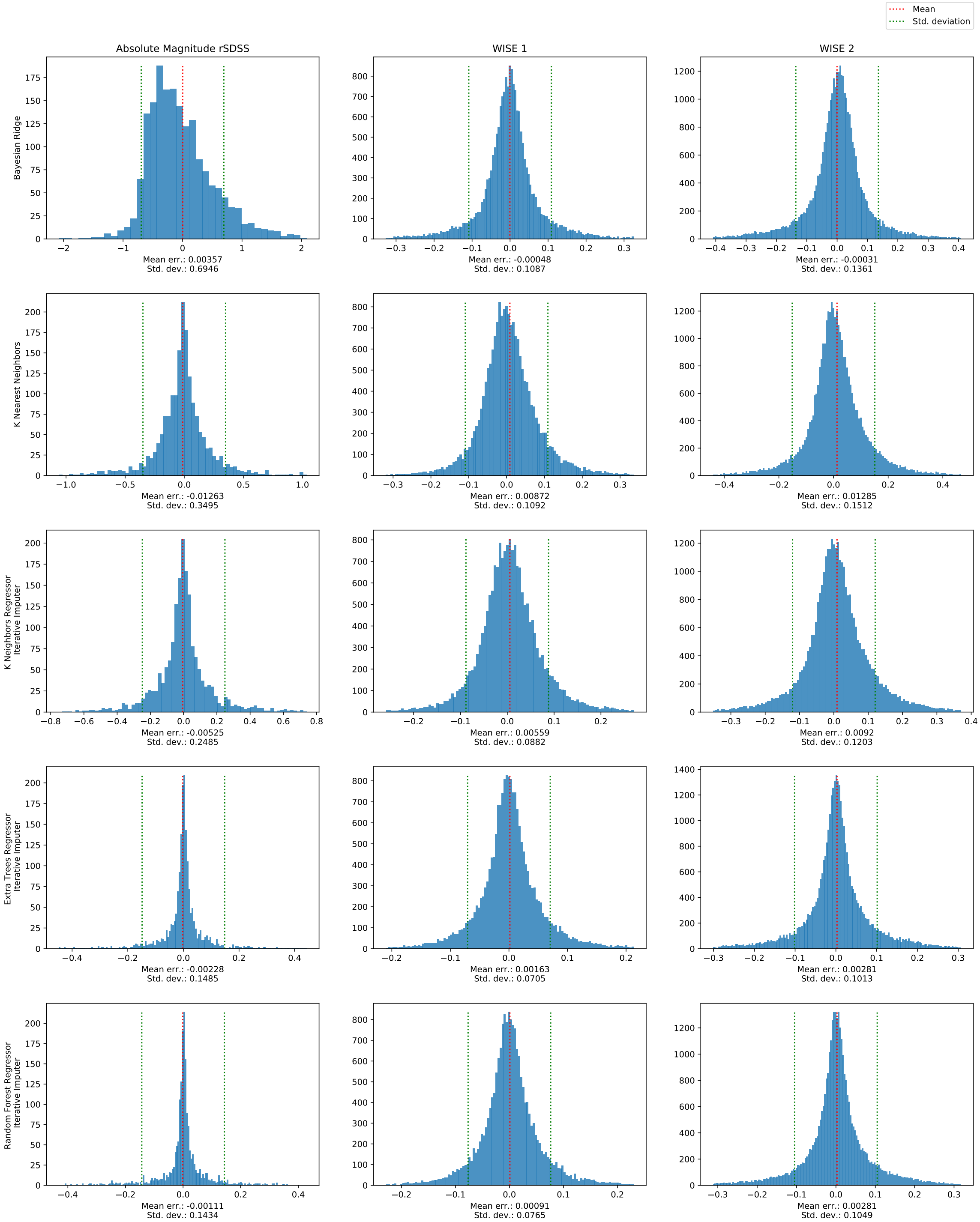

FIGURE 7.3: Errors (predictions substracted from the real values) and their standard deviation for the MCAR mechanism simulation.

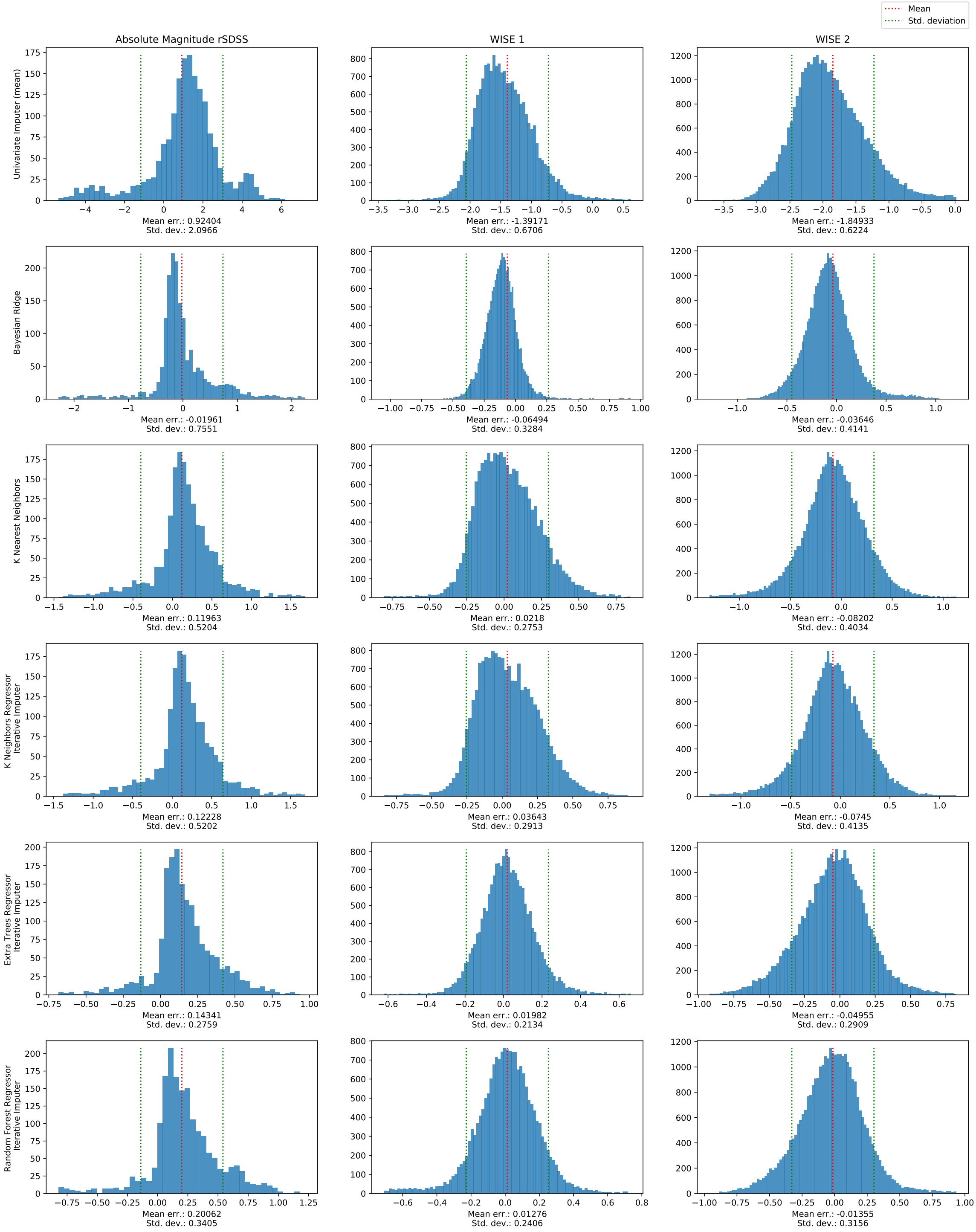

FIGURE 7.4: Errors (predictions substracted from the real values) and their standard deviation for the MAR mechanism simulation.

	Abs. mag. (r)			
Estimator	Variance	Std. deviation	$\bar{U}$	B
Extra Trees Regressor	0.01701	0.13041	0.01699	2e-05
Random Forest Regressor	0.0098	0.09899	0.0098	0.0
	$WISE1$			
Extra Trees Regressor	0.01968	0.14027	0.01967	0.0
Random Forest Regressor	0.03994	0.19984	0.03993	1e-05
	$WISE2$			
Extra Trees Regressor	0.02562	0.16005	0.0256	1e-05
Random Forest Regressor	0.05048	0.22467	0.05047	1e-05

TABLE 7.2: Variance, Standard deviation, the between imputation variance B and the within imputation variance $\bar{U}$ estimations using Rubin's rule for the ETR and RFR estimators and for the three variables with missing values, Abs. mag. (r), $WISE1$ and $WISE2$ in the 200000 subset.

where

$$\bar{U} = \frac{1}{m} \sum_{i=1}^{m} U_i \tag{7.2}$$

is the estimated within imputation variance and

$$B = \frac{1}{m-1} \sum_{i=1}^{m} (\hat{Q} - \bar{Q})^2 \tag{7.3}$$

is the between imputation variance. When B dominates $\bar{U}$, greater efficiency, hence more accurate estimates, can be obtained by increasing m. Conversely, when $\bar{U}$ dominates B, little is gained from increasing m. Table 7.2 shows Variance, Standard deviation, the between imputation variance B and the within imputation variance $\bar{U}$ for the two best estimators, ETR and RFR, using Rubin's rule. For all the Abs. mag.(r), $WISE1$ and $WISE2$, $\bar{U}$ dominates B over $\bar{U}$ so increasing m beyond the 10 current iterations does not provide higher accuracy.

Standard deviations from Rubin's rule are comparable but lower than those computed from Figure 7.4. It might be explained by the contribution of MNAR mechanisms in the underlying missingness which could be captured by our simulations but not by Rubin's rule.

As stated previously, all these evaluations are carried out on a 200000 subset whose real values are known and with two main objectives; understanding the errors produced by the different Imputation techniques and selecting

	Abs. mag. (r)			
Estimator	Variance	Std. deviation	$\bar{U}$	B
ETR	0.01834	0.13543	0.01825	1e-05
	$WISE1$			
ETR	0.01873	0.13686	0.01872	0.0
	$WISE2$			
ETR	0.02376	0.15414	0.02365	1e-05

TABLE 7.3: Same as 7.2 but only for the ETR and applied to the whole dataset.

the best estimator. Both ETR and RFR work the best, but due to a balance between errors and variances among the three variables, the ETR is chosen. Therefore a MI using this estimator is applied to the whole dataset to predict its missing values. A similar error study to this from Figure 7.4 is not possible since their real values are not known. Therefore, only Rubin's rule, which is shown in Table 7.3, can be used. It shows comparable results to those applied to the 200000-sources dataset. Although these missing values should be more error-prone as they are real rather than simulated missing values, this effect is at least partially offset by the increased number of sources ($\sim$ 960000) used to train the imputations.

7.2 Classification algorithm

The resulting imputed dataset contains 958665 samples and no missing values. The purpose now is to train a ML algorithm to identify CVs as the J-PLUS survey progresses. There are several ML algorithms for classification problems, including some adaptations of those used for imputations in the previous section. However, when entering the range of several hundreds of thousands of samples for training, the most appropriate group of algorithms are those belonging to the artificial neural networks (ANNs) family, in this case, a Dense Neural network is trained.

7.2.1 Multilayer Perceptron

ANNs were first proposed in the form of Perceptrons in 1944 by Warren McCullough and Walter Pitts. They were after developed in the 1950s and 1960s by Frank Rosenblatt. Today, it's more common to use more complex models within the Multilayer Perceptron (MLP) theory.

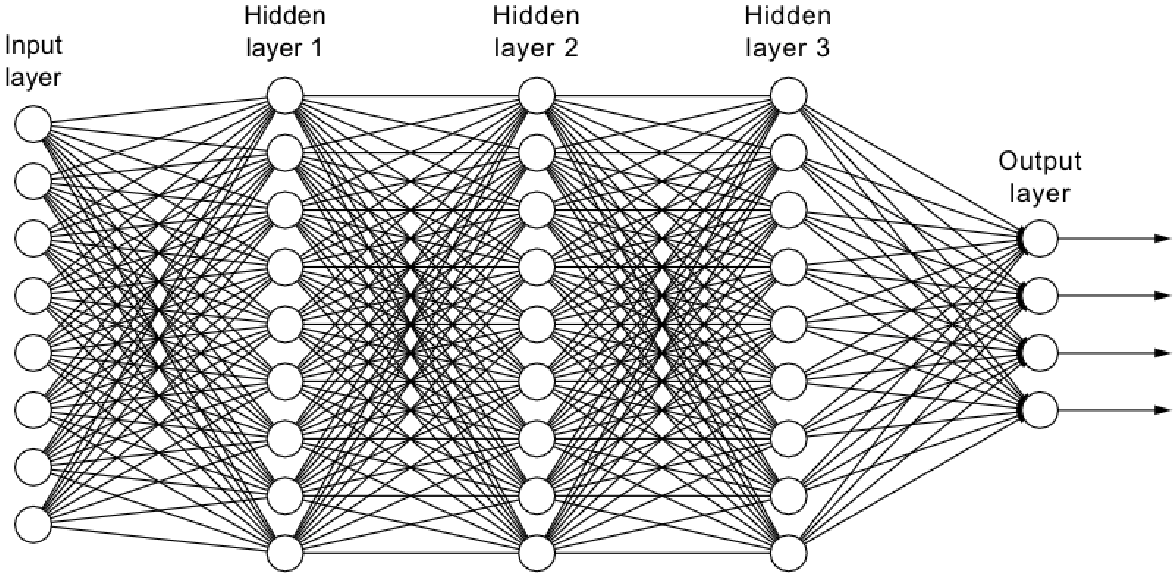

FIGURE 7.5: Multilayer Perceptron representation. This ANN is a generic case for multiclass classification with an input layer, 3 hidden layers and an output layer. The ouput layer is comprised of a number of neurons equal to the number of classes. For the binary classification case, one neuron in the last layer is enough and the choice of a threshold will discriminate between classes.

A MLP is comprised of elemental units called neurons (Haykin 1994) and corresponds to an ANN whose neurons or units are structured in layers. All neurons belonging to a given layer receive the same input vector and each unit processes this vector independently according to its own parameters. The outputs of each neuron in the same layer are grouped to form the input vector for the next layer. This process continues in this way until reaching the output layer. For binary classification tasks, the output layer is ususally a single neuron with a sigmoid activation function, which returns predictions in the form of probabilities that a given sample belongs to the class tested. The choice of a threshold will determine the class of the object and can be used as a tool to obtain a trade-off between purity and completeness depending on the task.

7.2.2 More considerations

In the common classification problems with ML, usually there is a well labelled training dataset and a set of observations to be classified. The training dataset is divided into 'training set', 'validation set' and 'test set' (with usual proportions of 70-15-15%, 80-10-10% or similar, depending on the total number of samples). The algorithm is trained with the training set and, simultaneously, the hyperparameters are configured (in the case of an ANN, the learning rate, optimizers, loss function, number of layers and units per layer, dropout etc...), the configuration that gives the best results applied in the validation set is selected and the errors obtained from applying it in the test set are those to consider. Finally, the algorithm obtained is applied in the set of observations to be classified, obtaining the desired class for each of them.

In this case we have a training dataset in which is assumed that there are misclassified CVs and we want to detect them, that is, we do not have a set of observations to classify, but the samples in our training dataset are our observations to be classified. This is a great disadvantage because we want to obtain an algorithm from this dataset and apply it to the same. This process would lead to overfitting, it learns the training samples very well but is not able to generalize correctly and obtains poor results in unknown samples. To solve the problem of overfitting, the approach followed is to split our dataset into 10 parts, each with 10% of the observations in the dataset. Each of these parts will be the sample to be classified. The remaining 90% of the dataset in each case will be used as training, validation and test sets (with the proportion 80-10-10%) to generate 10 independent algorithms. Therefore, after applying each of the algorithms to the corresponding sample to be classified, we will obtain a probability of being CV for each of the objects in our initial dataset. Finally we select a threshold from which we will consider an object classified as CV and all the resulting 'mistakes' or contaminants will be our CV candidates.

Nonetheless, the architecture used is the same for all the 10 algorithms (see Figure 7.6) as several preliminary tests changing the number of layers and neurons per layer showed to work notably well. The *Keras API* provided by the Python version of *TensorFlow 2.0*[8] was used.

As explained in Section 6.1, from our 958665 samples dataset, only 343 are known CVs. In order to deal with the high imbalance, we computed the class weights using the *compute_class_weight* function[9] provided by the sklearn Python package.

---

[8] `https://www.tensorflow.org`

[9] `https://scikit-learn.org/stable/modules/generated/sklearn.utils.class_weight.compute_class_weight.html`

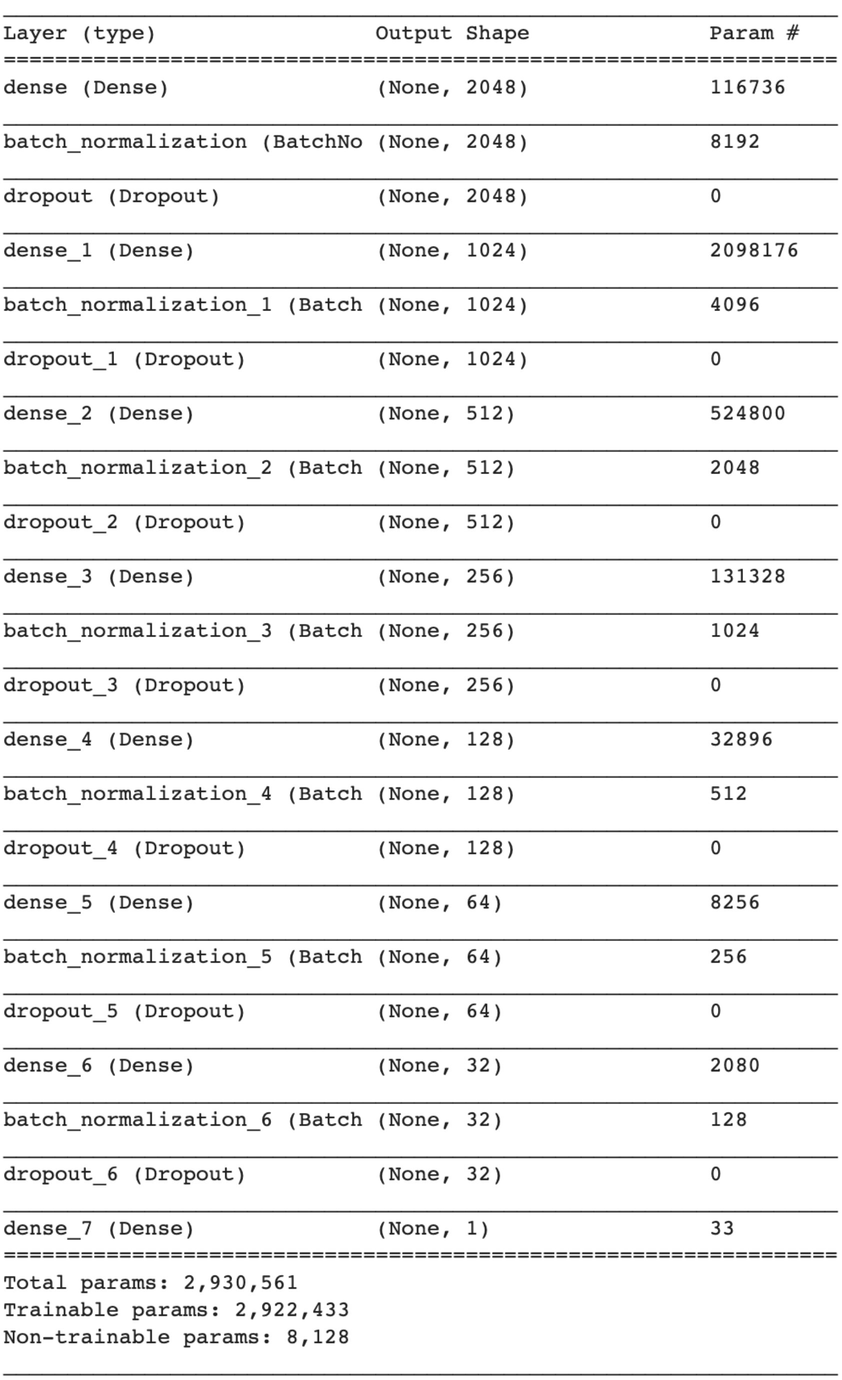

```
_________________________________________________________________
Layer (type)                 Output Shape              Param #
=================================================================
dense (Dense)                (None, 2048)              116736
_________________________________________________________________
batch_normalization (BatchNo (None, 2048)              8192
_________________________________________________________________
dropout (Dropout)            (None, 2048)              0
_________________________________________________________________
dense_1 (Dense)              (None, 1024)              2098176
_________________________________________________________________
batch_normalization_1 (Batch (None, 1024)              4096
_________________________________________________________________
dropout_1 (Dropout)          (None, 1024)              0
_________________________________________________________________
dense_2 (Dense)              (None, 512)               524800
_________________________________________________________________
batch_normalization_2 (Batch (None, 512)               2048
_________________________________________________________________
dropout_2 (Dropout)          (None, 512)               0
_________________________________________________________________
dense_3 (Dense)              (None, 256)               131328
_________________________________________________________________
batch_normalization_3 (Batch (None, 256)               1024
_________________________________________________________________
dropout_3 (Dropout)          (None, 256)               0
_________________________________________________________________
dense_4 (Dense)              (None, 128)               32896
_________________________________________________________________
batch_normalization_4 (Batch (None, 128)               512
_________________________________________________________________
dropout_4 (Dropout)          (None, 128)               0
_________________________________________________________________
dense_5 (Dense)              (None, 64)                8256
_________________________________________________________________
batch_normalization_5 (Batch (None, 64)                256
_________________________________________________________________
dropout_5 (Dropout)          (None, 64)                0
_________________________________________________________________
dense_6 (Dense)              (None, 32)                2080
_________________________________________________________________
batch_normalization_6 (Batch (None, 32)                128
_________________________________________________________________
dropout_6 (Dropout)          (None, 32)                0
_________________________________________________________________
dense_7 (Dense)              (None, 1)                 33
=================================================================
Total params: 2,930,561
Trainable params: 2,922,433
Non-trainable params: 8,128
_________________________________________________________________
```

FIGURE 7.6: The ANN architecture used. It is comprised of 7 hidden layers with 2048, 1024, 512, 256, 128, 64 and 32 neurons respectively. A normalization of the data is applied on each layer, as well as a dropout of 0.2. RELU is used as activation function in all hidden layers and a sigmoid one in the output one. Other hyperparameters; Learning rate of 0.01, batch size of 128, ADAM optimizer and binary cross entropy as the loss function.

Also, the data first are manipulated to feed them in the most suitable form into the network. For each sample, the data point before any manipulation contains its coordinates (R.A. and Dec), $Abs.mag.(r)$ obtained from *Gaia*, the bands from J-PLUS, $J0395$, $J0410$, $J0430$, g, $J0515$, r, $J0660$, i, $J0861$, those from WISE, $WISE1$ and $WISE2$ and the class of the source, 1 for CVs, 0 otherwise. The coordinates are not used for the training since they do not add relevant information and the class is the target to predict. Instead of using the photometry directly, and leaving aside the Abs. mag.(r), the bands are transformed to colours, and all possible combinations of colours are computed[10]. Subsequently all the data are re-scaled in the range (-1, 1). In theory, if the input variables are combined linearly, as in an MLP, then it is rarely strictly necessary to standardize the inputs. The reason is that any re-scaling of an input vector can be effectively undone by changing the corresponding weights and biases, leaving the exact same outputs as if no re-scaling were done. However, there are a variety of practical reasons why standardizing the inputs can make training faster and reduce the chances of getting stuck in local optima.

7.2.3 The candidates and final results

Due to the imbalance in the number of CVs with respect to the total number of observations in the dataset, a metric is needed to measure the performance of the algorithm capable of taking this into consideration. A metric of general accuracy may lead to undesirable results since an algorithm that classified all objects as non-CVs would obtain an amazing accuracy of 99.964% but would not be an acceptable result since it would not detect any CVs. To measure the performance of the algorithm, in this work we use the measures of purity and completeness.

The result after applying the model obtained on the imputed dataset, returns the probability of an object of being a CV. The selection of a probability threshold above which an object is classified as a CV allows us to control the

---

[10] The final features are: $Abs.mag.(r), J0395 - J0410, J0395 - J0430, J0395 - g, J0395 - J0515, J0395 - r, J0395 - J0660, J0395 - i, J0395 - J0861, J0395 - WISE1, J0395 - WISE2, J0410 - J0430, J0410 - g, J0410 - J0515, J0410 - r, J0410 - J0660, J0410 - i, J0410 - J0861, J0410 - WISE1, J0410 - WISE2, J0430 - g, J0430 - J0515, J0430 - r, J0430 - J0660, J0430 - i, J0430 - J0861, J0430 - WISE1, J0430 - WISE2, g - J0515, g - r, g - J0660, g - i, g - J0861, g - WISE1, g - WISE2, J0515 - r, J0515 - J0660, J0515 - i, J0515 - J0861, J0515 - WISE1, J0515 - WISE2, r - J0660, r - i, r - J0861, r - WISE1, r - WISE2, J0660 - i, J0660 - J0861, J0660 - WISE1, J0660 - WISE2, i - J0861, i - WISE1, i - WISE2, J0861 - WISE1, J0861 - WISE2, WISE1 - WISE2$

purity-completeness trade-off. A very low threshold obtains very high completeness (all CVs are retrieved) at the cost of very low purity (among the candidates, there will be a large majority of contaminants). On the contrary, a too high threshold will have hardly any contaminants and therefore a high purity, but will miss a high percentage of the CVs, leading to low completeness.

- True positive (tp): CVs correctly identified as CVs.
- False positive (fp): Non-CVs incorrectly identified as CVs.
- True negative (tn): Non-CVs correctly identified as Non-CVs
- False negative (fn): CVs incorrectly identified as Non-CVs
- Purity or True Positive Rate (tpr): $\frac{\text{tp}}{\text{tp} + \text{fp}}$
- False Positive Rate (fpr): $\frac{\text{fp}}{\text{fp} + \text{tn}}$
- Completeness or Sensitivity :$\frac{\text{tp}}{\text{tp} + \text{fn}}$

The threshold has been chosen by analyzing the tpr and fpr. Figure 7.7 shows the evolution of tpr and fpr with respect to the threshold. A slightly different way of understanding it is that the tpr determines the amount of CVs recovered and the fpr, the amount of contaminants. Since the number of potential contaminants is enourmous compared with the number of CVs, the threshold is adjusted to maximize the discarding of contaminants with no substantial loss in CVs.

Another tool that allows visualization of the performance of an algorithm is the confusion matrix. Each row of the matrix represents the instances in an actual class while each column represents a predicted class. Figure 7.8 shows the confusion matrix with absolute numbers and standardized.

Results

The algorithm is able to retrieve 299 out of the 343 CVs included in the dataset. 624 more objects which were not classified as CV, are classified by the algorithm as such. Those are our candidates. A full list of these candidates is shown in Appendix D. Table 7.4 shows the general results in the same format as in the colour-colour and colour-magnitude methodologies presented in Section 6.3.2 for comparative purposes.

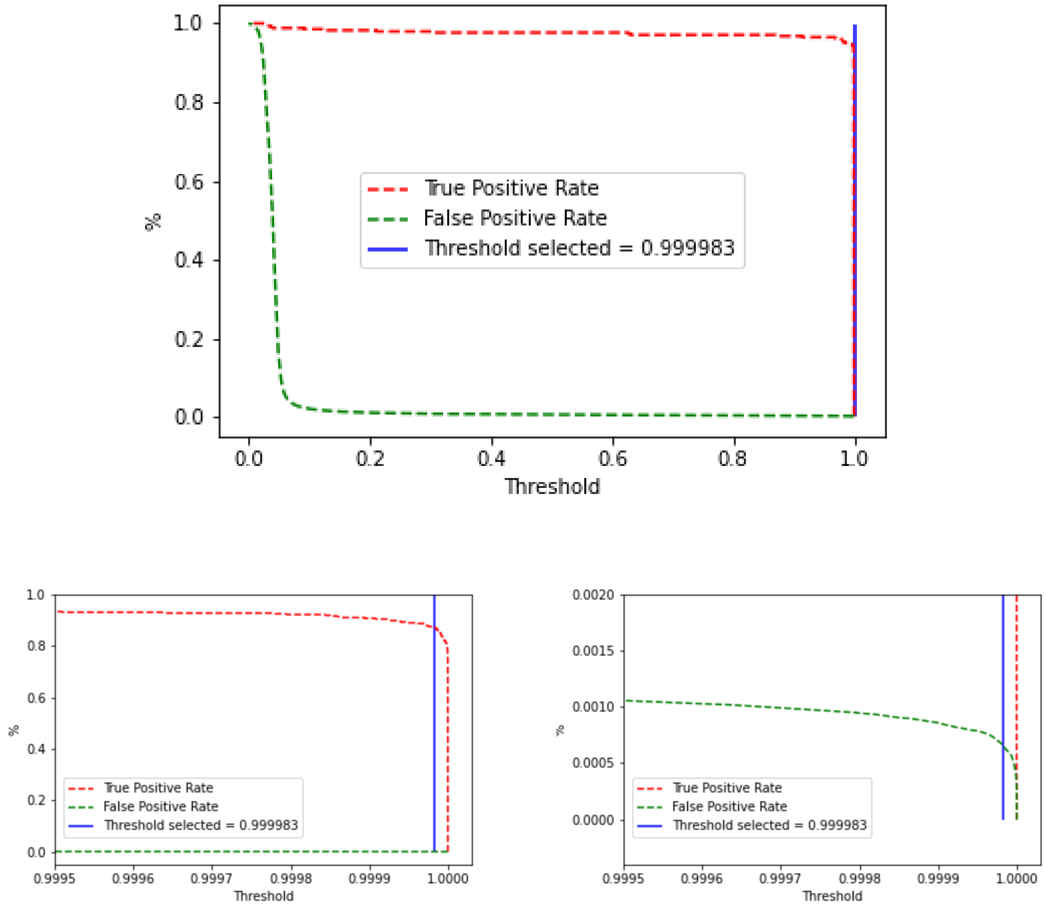

FIGURE 7.7: The evolution of tpr and fpr with respect to the threshold. At the top, the whole picture, at the bottom, zooms-in of the same figure to make it legible. The selected threshold is located just before the big drop in true positive rates taking advantage of part of the drop in fpr.

Figure 7.9 shows the location of the 624 candidates in the H-R diagram. It uses the same format and axis than those from Chapter 5. The candidates are mainly located below the main sequence path. A considerable amount of them are within the WDs locus, which either means there are WDs contaminants among our candidates or some CVs share their locus with them[11].

Appendix C shows a sample of the candidates contained within the SDSS spectral database. Main contaminants are WDs as stated previously. There are also a considerable amount of M4 – 5 systems and hot stars.

---

[11] From Figure 5.2 in Section 5.2.2, WZ Sge systems got into the WDs locus. Objects with great outburst amplitudes, slow declines and long intervals between outbursts which have been considered as period bouncer candidates

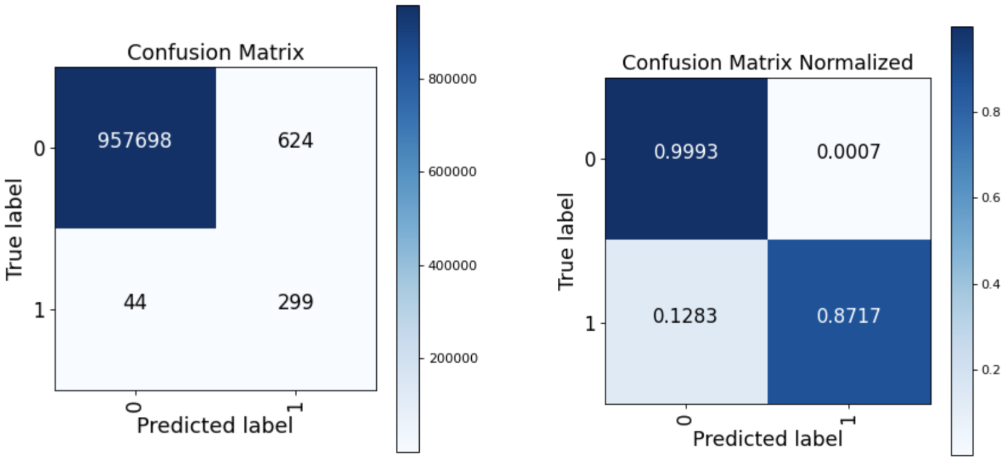

FIGURE 7.8: On the left, the confusion matrix with absolute values, on the right, the same confusion matrix but standardized. 1 stands for CVs and 0 for non-CVs.

Total number of sources in J-PLUS DR1	$\sim$ 13.4 mill.
Sources after quality filtering	958665
Sources classified as CV	923
of which with SDSS spectra available	477
of which catalogued as CV by SDSS	283
Total known CVs in the dataset	343
Total known CVs recovered	299
Completeness of the method	87.17%
Purity of the method	59.33%

TABLE 7.4: Summary table of the Machine learning methodology applied to all J-PLUS DR1.

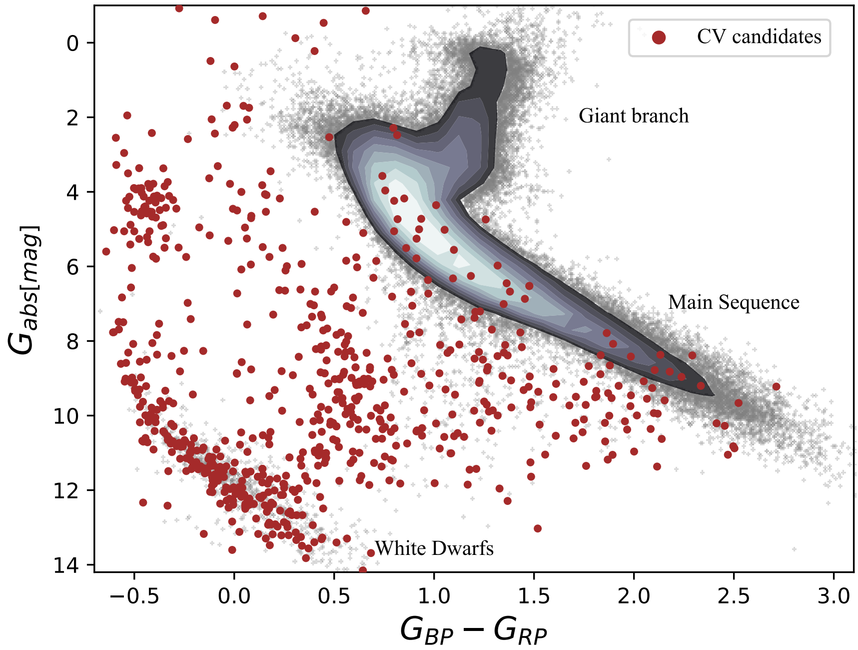

FIGURE 7.9: Distribution of the 624 CV candidates in the H-R diagram.

Chapter 8

Conclusions and future work

With the increase in detector efficiency and power of computing, wide-field surveys are increasing in number, multiplying the data generated. Such large datasets of different nature allow synergies that can lead to a better understanding of the study carried out. The main challenge we are currently facing is how to handle, process, standardize and analyze this continuous increasing information. The combination presented here of the J-PLUS, SDSS, WISE and *Gaia* surveys, and the different techniques to find CVs are good examples of this.

8.1 Conclusions

In this thesis I have set out the results of my research into two main aspects; the study of the CV evolutionary cycle, both as a whole group and by their CV subtype, using *Gaia* DR2 data and the identification of CVs using different techniques and data surveys combinations.

8.1.1 CV evolutionary cycle in *Gaia's* HR-Diagram

Some deductions have been made from the distribution of CVs in the H-R diagram. The *Gaia* space mission has allowed, for the first time, the analysis of the distribution of these objects with respect to their absolute magnitudes. Through the statistical study of these data, it has been reported the discovery of a trend of the orbital period and mass accretion based on their colours and absolute magnitudes. The CV population density has also been studied with respect to their absolute magnitudes, with a peak in $G_{abs} \sim 10.15$. The contribution of the different subtypes of CVs has been described, including the WZ Sge systems among the DNe, well placed candidates for period bouncers. The respective distributions occupy different positions in the H-R diagram, and thus serve as an approximate diagnostic for the orbital periods and the CV subtype parameters. To conclude this section, this work has also identified the location of the dCVs, CVs across the period gap, and composed of a WD and secondaries in the range M4 – M6. Due to the small number of dCVs, there is great uncertainty in the behaviour of these systems and the evolution of the CVs in this phase, therefore, this result allows to narrow the search for dCVs important for the understanding of CV evolution as a whole.

8.1.2 Identification of CVs

Historically, CVs have been found as byproducts of other searches, mainly for QSOs. In the last years several attempts focused on their search have been made (Gentile Fusillo, Gänsicke, and Greiss 2015, Scaringi et al. 2013, Szkody et al. 2002). Still, with relative success, the biases of these searches are not well understood and their values of purity and completeness are relatively low. It shows the difficulties in identifying these systems.

Based on data from J-PLUS, a wide-field, narrow-band survey that allows the location of specific features, this document shows the process and obstacles encountered in detecting CVs in the attempt to overcome the limitations of previous searches.

Applying a methodolgy based exclusively on the J-PLUS survey, in spite of its diverse filter set, is not successful in defining a CV sample with a satisfactory purity coefficient, there is a strong contamination by QSOs at particular redshifts. In a second phase, we added WISE photometry which, although improving the previous results on QSOs, does not provide an effective way to exclude hot stars and non-CV WD-MS stars. The inclusion of *Gaia* parallaxes determining the CV locus in the H-R diagram and the cut in the derived distances refines the search removing a substantial amount of QSO, hot stars and other point sources with Hα emission, yielding a set of 104 candidates in the first 1022 deg^2 of J-PLUS. However, GTC spectroscopic observations have shown a larger amount of contaminants. Along with this, the low amount of candidates demonstrates that completeness is still far from being achieved.

Several data imputation techniques, a tool that has permitted the use of all available observations with no loss of consistency, have subsequently been presented in order to fill all missing data derived from the cross-match among surveys. And finally, the resulting dataset has fed a neural network to separate CVs from other objects allowing to probe an even broader parameter space. Comparison with SDSS spectra yields a completeness of 87% and a purity of 59%, although, from past experiences, these numbers should be taken with caution until follow-up observations are made.

In general terms and awaiting follow-up observations, J-PLUS data are able to improve results of previous searches based on other surveys. However, the J-PLUS filter set has some limitations regarding CV searches and would benefit from a wider range of narrow filters as those from the J-PAS project.

8.2 Future work

The resulting candidates of the Artificial Neural Network methodology will be the targets of a spectroscopic follow-up in order to confirm them as CVs. It is expected therefore, to enlarge the existent CV sample. It will facilitate the application of similar methodologies as those presented in this work using the J-PAS filter set. Thus, likely will find further correlations and patterns that will allow a more successful identification of CVs and a better understanding of the completeness. Also, this work is the base to find WD-M(4 – 6) binary systems or binaries with fainter companions such as WD-BDs, which could potentially be period gap and period bouncer CVs respectively.

Appendix A

ADQL Query

This is the ADQL query used for data cleansing as indicated in Section 4.2.1 through the VO Asynchronous Queries for J-PLUS data. It is the one applied for the initial data of the ML methodology presented in Section 7.2 and for methodologies B and C presented in Section 6.3.2. For method A, it is exactly the same query but excluding the *i*-band as it is not utilized.

```
SELECT
jplus_.TILE_ID, jplus_.NUMBER, jplus_.ALPHA_J2000,
jplus_.DELTA_J2000, jplus_.FWHM_WORLD as FWHM, jplus_.MAG_AUTO,
jplus_.MAG_ERR_AUTO, jplus_.FLAGS, jplus_.NORM_WMAP_VAL,
jplus_.MASK_FLAGS, jplus_.SINGLE_DETECT, jplus_.CLASS_STAR
FROM
jplus.CalibratedMagABDualObj as jplus_
WHERE
jplus_.MAG_ERR_AUTO[jplus::J0395] < 0.2 AND
jplus_.NORM_WMAP_VAL[jplus::J0395] > 0.8 AND
jplus_.MASK_FLAGS[jplus::J0395] = 0 AND
jplus_.SINGLE_DETECT[jplus::J0395] > 0 AND
jplus_.MAG_ERR_AUTO[jplus::gSDSS] < 0.2 AND
jplus_.NORM_WMAP_VAL[jplus::gSDSS] > 0.8 AND
jplus_.MASK_FLAGS[jplus::gSDSS] = 0 AND
jplus_.SINGLE_DETECT[jplus::gSDSS] > 0 AND
jplus_.MAG_ERR_AUTO[jplus::rSDSS] < 0.2 AND
jplus_.NORM_WMAP_VAL[jplus::rSDSS] > 0.8 AND
jplus_.MASK_FLAGS[jplus::rSDSS] = 0 AND
jplus_.SINGLE_DETECT[jplus::rSDSS] > 0 AND
jplus_.MAG_ERR_AUTO[jplus::J0660] < 0.2 AND
jplus_.NORM_WMAP_VAL[jplus::J0660] > 0.8 AND
```

```
jplus_.MASK_FLAGS[jplus::J0660] = 0 AND
jplus_.SINGLE_DETECT[jplus::J0660] > 0 AND
jplus_.MAG_ERR_AUTO[jplus::iSDSS] < 0.2 AND
jplus_.NORM_WMAP_VAL[jplus::iSDSS] > 0.8 AND
jplus_.MASK_FLAGS[jplus::iSDSS] = 0 AND
jplus_.SINGLE_DETECT[jplus::iSDSS] > 0 AND
(jplus_.FLAGS[jplus::rSDSS] < 4 OR (jplus_.FLAGS[jplus::rSDSS] >
2047 AND jplus_.FLAGS[jplus::rSDSS] < 2052)) AND
jplus_.CLASS_STAR > 0.8
```

Appendix B

GTC spectroscopic follow-up

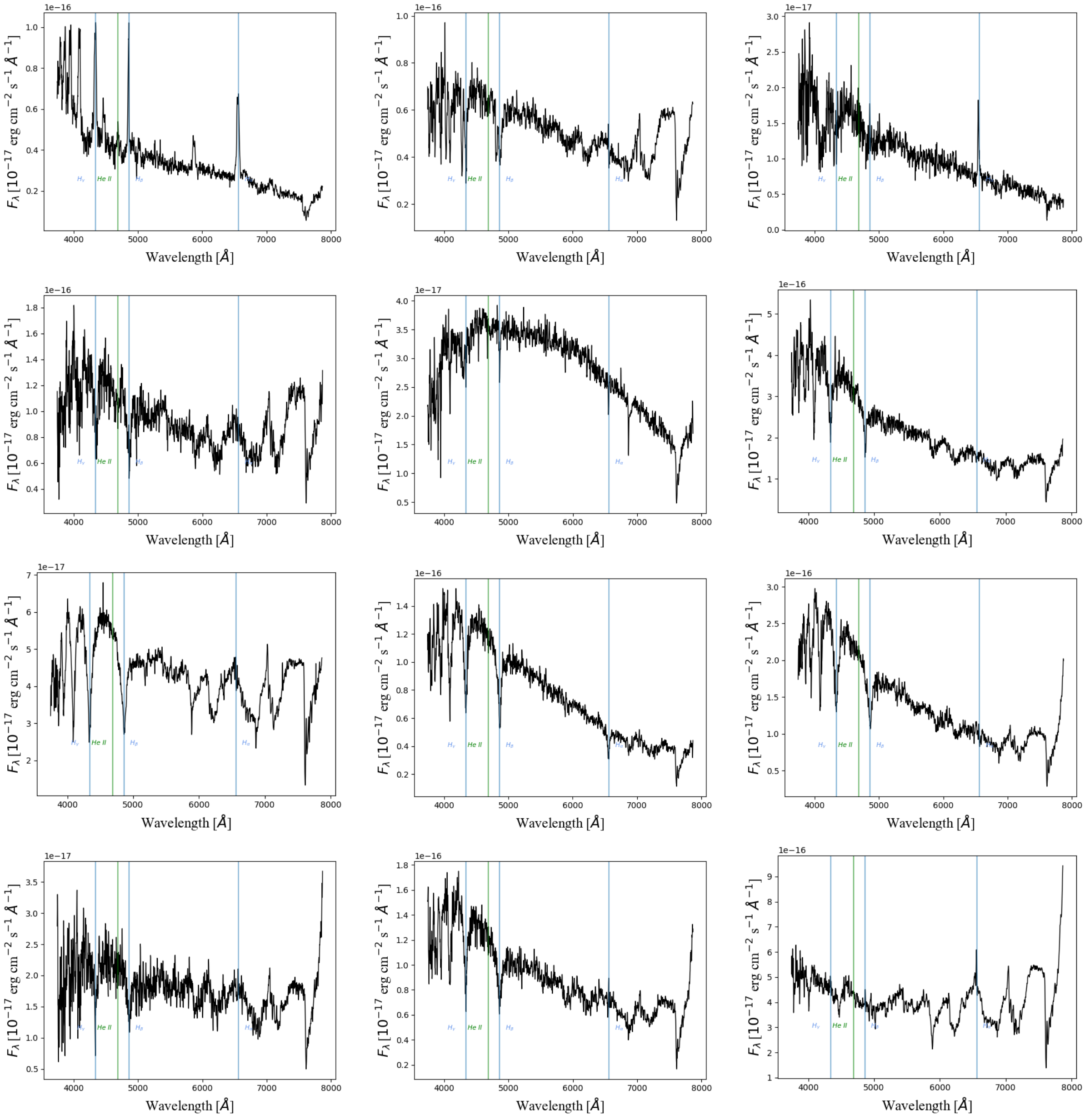

Appendix C

ANN candidates spectra

A sample of the candidates from the Artificial Neural Network algorithm contained in the SDSS spectral database. The first three are catalogued as CV by SDSS.

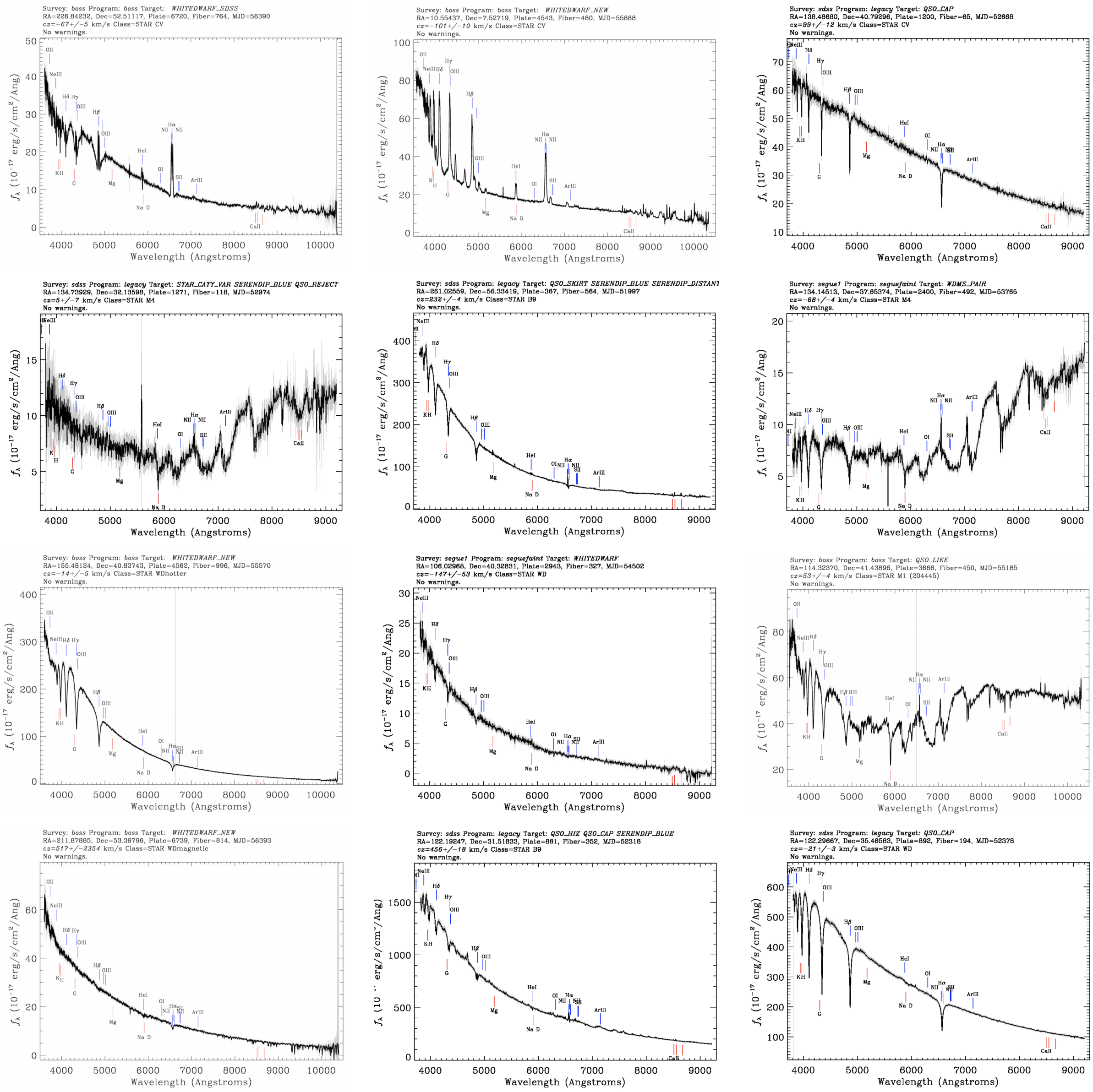

Appendix D

Full list of candidates

The full list of candidates obtained from the Neural Network. For legibility, only a subset of J-PLUS bands are shown. In order to give an idea of how many objects would be missing if no imputation was applied, the WISE bands and Abs. Magnitude (r) are in the original form and 'nan' is shown when missing.

R.A.	Dec	Abs. mag (r)	$J0395$	r	$J0660$	i	$WISE1$	$WISE2$
238.89	50.43	13.95	17.18	16.37	16.39	16.27	nan	nan
28.8	1.84	6.42	16.86	17.69	17.91	18.1	nan	nan
215.14	53.27	13.27	19.47	19.33	19.34	19.3	nan	nan
142.68	30.73	11.58	18.51	18.41	18.52	18.86	nan	nan
134.29	41.83	14.05	18.94	18.73	18.75	18.74	nan	nan
35.35	29.61	11.57	17.07	17.22	17.55	17.52	nan	nan
279.18	41.51	4.32	15.56	15.68	15.76	15.74	14.71	14.87
1.07	2.19	12.86	18.62	18.74	18.74	18.93	nan	nan
263.81	57.5	11.61	16.84	16.68	16.97	16.93	16.89	nan
244.44	53.05	9.55	19.32	17.65	17.36	16.46	13.48	13.37
207.43	27.92	13.94	16.92	16.33	16.4	16.32	nan	nan
187.64	55.19	9.57	18.34	16.89	16.59	16.0	13.34	13.23
28.96	4.53	11.44	16.95	16.9	17.22	17.14	16.93	nan
340.49	13.54	14.37	17.97	17.13	17.1	17.01	nan	nan
280.25	39.83	11.45	15.62	15.49	15.84	15.73	15.86	15.76
222.32	56.58	9.39	19.7	19.3	19.08	18.5	nan	nan
109.17	39.75	11.23	19.62	18.41	18.07	17.38	14.6	14.38
130.76	33.21	10.64	17.3	17.19	17.35	17.22	nan	nan
124.49	31.8	10.02	17.74	18.47	18.73	18.75	nan	nan
332.74	29.97	11.41	18.4	18.63	18.95	19.07	nan	nan
202.91	55.9	6.87	19.42	19.13	18.75	18.78	nan	nan
139.76	30.65	9.36	19.21	17.72	17.36	16.7	14.1	13.99
22.44	41.28	11.51	19.36	19.43	19.44	18.86	15.79	15.68
23.06	5.44	11.38	16.5	16.41	16.72	16.68	nan	nan
282.31	41.54	5.72	17.74	18.35	18.55	18.62	17.95	nan

R.A.	Dec	Abs. mag (r)	$J0395$	r	$J0660$	i	$WISE1$	$WISE2$
20.5	5.17	13.44	18.18	17.95	18.11	18.07	nan	nan
241.33	55.95	12.72	18.12	17.49	17.54	17.24	nan	nan
280.98	40.44	8.49	17.98	16.48	16.17	15.52	12.81	12.73
39.58	29.42	13.64	19.31	19.02	19.18	19.07	nan	nan
137.72	39.53	12.69	18.81	18.55	18.69	18.7	nan	nan
130.19	37.24	14.14	19.16	18.51	18.48	18.43	nan	nan
140.65	40.35	11.8	18.22	18.48	18.67	18.83	nan	nan
273.82	40.9	14.26	18.41	17.58	17.55	17.44	nan	nan
121.49	31.95	2.47	12.85	13.05	13.2	13.26	12.99	13.02
10.8	5.68	7.79	19.14	19.16	18.76	19.07	15.84	14.6
26.81	2.63	4.8	15.57	15.79	15.85	15.88	15.0	15.0
128.44	29.96	10.45	18.09	18.8	18.95	18.84	nan	nan
8.61	5.12	11.02	17.92	18.09	18.38	18.33	nan	nan
236.12	54.93	13.53	19.19	19.06	19.13	19.14	nan	nan
337.24	9.62	4.3	13.97	14.03	14.04	14.04	12.83	12.89
123.24	30.34	8.02	19.39	19.27	19.11	19.09	15.89	14.84
278.89	39.61	10.01	17.73	17.88	18.03	18.25	nan	nan
130.9	34.2	12.01	17.32	17.07	17.25	17.12	nan	nan
285.08	40.78	5.58	19.17	17.2	17.18	17.02	15.38	15.73
106.48	38.28	10.21	18.23	18.06	18.03	17.48	14.92	14.82
150.03	39.5	13.95	19.55	18.67	18.63	18.58	nan	nan
129.14	37.72	13.08	19.0	18.69	18.75	18.57	16.76	nan
332.14	9.56	8.32	17.35	17.84	17.93	17.97	nan	nan
347.92	23.45	11.52	18.79	19.28	19.31	19.51	nan	nan
331.97	34.48	12.25	15.43	15.24	15.46	15.39	15.07	15.15
332.69	34.03	6.5	19.13	19.03	18.94	18.87	nan	nan
228.66	53.49	3.51	16.62	16.71	16.84	16.88	16.3	16.67
182.8	56.81	8.01	18.98	19.13	18.68	18.8	nan	nan
239.18	50.26	3.65	15.52	16.36	16.53	16.74	17.2	nan
35.5	44.45	2.83	15.39	15.7	15.81	15.94	15.93	15.99
123.71	40.99	11.9	19.09	19.25	19.45	19.1	16.32	16.06
258.7	56.32	10.59	18.16	18.59	18.78	18.76	nan	nan
150.06	30.73	10.79	19.64	18.91	18.66	17.79	14.4	14.29
336.69	11.18	11.69	17.89	17.28	17.14	16.38	13.19	13.06
182.59	56.58	11.01	18.22	18.59	18.84	18.9	nan	nan
28.43	4.42	10.79	17.13	17.2	17.42	17.38	nan	nan
138.43	41.55	9.19	19.48	17.95	17.55	16.79	14.0	13.93
153.94	40.04	11.19	18.56	18.87	18.95	19.1	nan	nan
224.92	53.32	10.31	19.51	17.95	17.61	16.87	14.04	13.92
133.13	32.16	14.08	18.76	17.99	17.97	17.85	nan	nan
256.05	26.83	11.47	19.23	19.6	19.76	19.83	nan	nan
127.2	31.53	14.09	18.76	18.2	18.19	18.04	16.92	nan
168.06	39.73	13.24	18.73	18.72	18.67	18.83	nan	nan
243.6	53.23	3.89	16.87	17.36	17.48	17.64	18.04	nan
256.2	24.41	3.06	16.12	16.25	16.37	16.46	16.04	16.14
134.05	30.58	10.75	18.32	17.75	17.6	17.01	14.21	13.94
3.69	7.04	10.33	19.0	19.62	19.53	19.59	16.48	15.66
7.29	4.94	4.87	14.5	15.21	15.35	15.52	15.61	15.63
276.29	43.11	13.4	19.41	19.02	19.09	18.95	nan	nan
1.61	3.69	12.65	18.87	18.55	18.61	18.59	nan	nan

R.A.	Dec	Abs. mag (r)	$J0395$	r	$J0660$	i	$WISE1$	$WISE2$
338.22	32.09	13.68	18.29	17.79	17.75	17.65	nan	nan
273.7	40.9	8.26	18.98	19.58	19.78	20.09	nan	nan
37.53	29.38	8.35	17.07	17.86	17.96	18.2	nan	nan
182.88	57.4	14.08	16.46	15.58	15.57	15.44	nan	nan
241.16	49.14	13.22	17.94	17.88	17.96	18.01	17.74	nan
204.41	55.91	8.17	18.92	19.03	18.88	18.92	17.4	nan
40.39	45.2	4.84	16.44	17.04	17.01	16.86	15.65	15.64
130.58	37.82	11.27	16.25	16.46	16.74	16.74	nan	nan
130.96	36.24	10.95	16.96	17.44	17.52	17.67	nan	nan
151.77	32.5	12.82	18.05	17.8	17.93	17.97	nan	nan
268.15	31.56	10.91	18.71	18.81	18.98	18.94	nan	nan
120.64	40.84	11.61	17.69	18.07	18.21	18.28	nan	nan
127.45	31.65	2.66	15.08	15.24	15.39	15.46	15.2	15.4
0.18	1.54	12.15	16.54	16.28	16.53	16.42	nan	nan
133.96	37.0	13.88	18.64	17.48	17.5	17.28	nan	nan
275.87	30.05	6.24	18.25	18.91	18.79	19.02	nan	nan
236.11	54.83	nan	18.21	17.7	17.51	16.82	14.1	13.91
1.41	37.02	11.84	18.03	17.97	18.19	18.31	nan	nan
37.07	32.4	8.56	19.16	17.5	17.15	16.62	13.98	13.93
126.03	33.71	6.79	18.22	17.83	17.34	17.83	13.97	13.04
8.37	5.68	13.53	18.42	17.92	17.94	17.85	nan	nan
121.12	42.22	12.55	17.16	16.9	17.03	16.94	nan	nan
273.17	30.61	9.26	17.47	18.15	18.23	18.47	nan	nan
148.55	30.77	14.16	19.61	19.1	19.01	19.1	nan	nan
117.16	38.69	14.03	19.42	18.67	18.64	18.47	nan	nan
128.23	31.65	14.16	18.42	17.7	17.6	17.45	nan	nan
238.3	56.64	12.22	18.64	18.74	18.94	18.94	nan	nan
124.9	35.49	11.33	19.81	19.21	18.95	18.56	15.72	15.58
330.93	34.12	7.95	19.33	18.68	18.52	18.23	15.6	15.51
151.92	40.69	10.6	18.75	17.6	17.36	16.64	14.01	13.83
135.94	55.28	0.75	13.4	13.91	14.07	14.22	14.18	14.12
140.53	41.42	13.71	19.2	18.62	18.59	18.5	nan	nan
38.13	45.17	7.0	19.64	17.04	16.95	16.67	14.73	14.92
215.03	53.38	12.8	17.21	16.8	16.89	16.8	16.1	16.18
330.22	32.3	10.62	18.8	16.96	16.64	16.03	13.25	13.18
334.38	13.55	8.49	18.83	19.6	19.3	19.48	nan	nan
200.27	56.17	7.75	17.53	17.27	17.46	17.41	16.62	nan
335.46	32.4	13.38	19.57	19.5	19.5	19.6	nan	nan
222.29	56.62	10.81	20.07	19.85	19.46	19.27	nan	nan
158.81	39.8	8.92	19.76	18.71	18.66	18.2	14.99	14.96
2.23	1.4	nan	18.47	18.12	17.96	17.24	14.31	14.2
119.83	39.98	8.65	18.78	19.69	19.76	19.56	16.23	15.85
3.58	1.2	9.12	19.09	19.7	19.38	19.46	16.59	15.81
242.42	47.59	11.63	16.8	16.67	16.95	16.87	nan	nan
37.96	29.09	10.62	18.55	18.56	18.58	18.62	nan	nan
331.36	30.87	10.9	17.38	17.51	17.74	17.73	nan	nan
337.29	11.31	9.75	17.55	18.14	18.24	18.46	nan	nan
239.18	48.38	9.65	19.45	17.98	17.62	16.93	14.22	14.04
12.11	7.99	10.37	19.59	19.43	19.42	18.86	15.85	15.71
338.95	11.84	5.85	16.67	16.99	17.06	17.12	16.73	nan

R.A.	Dec	Abs. mag (r)	$J0395$	r	$J0660$	i	$WISE1$	$WISE2$
14.71	6.65	12.67	18.0	17.65	17.71	17.62	nan	nan
113.43	39.17	12.85	17.98	17.86	18.04	18.05	nan	nan
120.99	33.92	13.65	19.53	18.5	18.35	18.26	nan	nan
334.62	31.86	7.33	18.48	17.53	17.36	17.07	14.76	14.72
216.27	54.61	8.83	18.23	18.7	18.89	18.95	nan	nan
28.88	4.74	9.0	19.49	18.07	17.81	17.08	14.25	14.08
120.97	32.23	12.65	18.83	18.57	18.72	18.69	nan	nan
116.81	79.34	9.06	19.27	17.55	17.21	16.48	13.65	13.5
243.37	54.34	11.45	19.65	19.62	19.75	19.28	16.84	16.92
344.07	32.22	2.59	14.62	14.96	15.09	15.23	15.09	15.07
237.76	47.46	4.53	15.66	16.18	16.33	16.48	nan	nan
339.75	11.57	9.51	18.54	16.77	16.4	15.82	13.15	12.98
139.04	54.63	10.19	16.84	17.43	17.69	17.81	17.75	nan
237.31	44.36	10.16	17.55	18.09	18.35	18.35	nan	nan
108.79	38.11	9.15	18.3	18.83	18.72	18.38	16.43	nan
36.41	33.31	11.21	18.38	17.37	17.13	16.26	13.09	12.9
169.38	39.58	8.88	18.67	19.5	19.53	19.19	16.44	15.71
28.37	5.76	9.69	15.79	16.41	16.6	16.78	17.39	nan
13.7	6.09	4.63	15.97	16.15	16.23	16.27	15.31	15.39
1.49	34.86	12.35	17.0	17.12	17.16	17.33	17.47	nan
258.16	56.42	4.26	15.63	16.24	16.37	16.48	15.96	15.98
39.06	30.72	12.58	19.06	18.91	19.06	19.04	nan	nan
134.74	30.21	11.25	17.83	17.97	18.14	18.17	nan	nan
7.18	5.99	13.46	18.72	18.43	18.38	18.34	nan	nan
237.59	56.83	4.02	17.18	17.12	17.06	17.19	16.36	16.5
138.6	29.86	7.97	19.41	19.04	18.82	18.8	16.11	15.25
135.83	53.63	nan	19.5	18.63	18.43	17.72	14.97	14.8
11.05	3.31	13.49	18.21	17.66	17.64	17.6	nan	nan
343.59	10.53	5.83	17.45	18.19	18.43	18.65	nan	nan
36.71	30.65	10.61	18.47	18.21	18.16	17.7	14.93	14.81
238.61	46.29	11.97	16.43	16.65	16.75	16.85	17.01	nan
333.7	30.93	8.31	17.22	17.79	17.9	18.22	nan	nan
330.4	32.39	11.05	16.93	16.93	17.2	17.2	nan	nan
227.21	53.03	12.7	18.14	17.85	18.01	17.85	nan	nan
352.08	33.32	10.32	15.84	14.96	14.73	13.99	nan	nan
144.69	31.36	5.09	16.9	16.95	16.63	17.02	16.25	15.98
223.57	55.2	10.91	15.73	16.23	16.46	16.58	17.11	nan
16.7	1.81	12.29	17.58	17.25	17.4	17.31	nan	nan
121.04	31.98	9.14	19.4	17.93	17.57	17.04	14.36	14.3
114.06	79.68	11.04	15.76	16.01	16.26	16.3	16.44	16.73
160.05	39.72	12.96	17.94	17.7	17.82	17.71	17.14	nan
8.16	7.79	11.88	18.53	18.74	18.86	18.87	nan	nan
186.9	56.0	8.39	19.11	18.0	17.67	17.13	14.58	14.24
138.49	40.79	13.45	17.7	17.18	17.17	17.08	nan	nan
39.64	7.14	12.06	16.71	16.55	16.82	16.75	nan	nan
245.0	49.65	10.9	18.51	18.95	18.95	19.29	nan	nan
143.62	32.18	11.98	18.62	18.42	18.5	18.36	nan	nan
244.25	53.71	12.82	19.22	19.24	19.34	19.48	nan	nan
258.6	57.42	11.54	19.1	17.6	17.2	16.17	12.93	12.73
241.69	43.62	10.63	19.37	18.54	18.33	17.46	14.43	14.29

R.A.	Dec	Abs. mag (r)	$J0395$	r	$J0660$	i	$WISE1$	$WISE2$
233.27	50.55	12.15	18.88	19.04	19.06	19.14	nan	nan
233.37	52.11	5.33	13.57	14.22	14.4	14.57	15.01	15.07
339.06	31.99	9.24	19.07	19.52	19.48	19.72	nan	nan
339.82	33.7	14.07	18.76	18.38	18.33	18.32	nan	nan
22.87	40.35	9.02	19.14	18.97	18.9	18.59	15.9	16.04
154.19	32.08	13.61	19.23	18.93	18.99	18.91	nan	nan
29.42	7.2	10.45	15.1	15.44	15.71	15.8	15.91	nan
227.86	53.44	11.63	16.12	16.09	16.41	16.37	nan	nan
352.39	33.78	4.77	15.62	16.18	16.31	16.49	16.82	nan
236.54	49.19	13.7	18.55	18.06	18.1	18.0	nan	nan
150.59	32.42	nan	19.61	18.64	18.4	17.87	15.27	15.08
37.56	35.74	5.26	18.33	17.12	17.14	18.7	15.77	15.9
135.72	32.22	6.74	17.71	18.34	18.52	18.83	nan	nan
1.32	7.22	11.07	17.89	18.33	18.39	18.53	nan	nan
241.75	42.29	7.93	18.39	18.62	18.52	17.97	15.3	15.06
188.41	55.86	7.03	19.48	19.15	18.8	19.18	15.88	15.17
111.78	30.28	4.38	16.89	17.07	17.09	17.2	16.58	nan
333.78	31.98	13.46	17.48	16.98	17.02	16.96	nan	nan
129.96	39.22	10.69	18.83	17.8	17.61	17.43	15.48	15.77
134.05	36.98	9.62	19.25	17.75	17.39	16.47	13.45	13.27
148.7	31.5	13.47	18.65	18.29	18.15	18.1	nan	nan
226.57	54.09	14.35	19.48	18.87	18.69	18.71	nan	nan
132.21	35.82	13.41	18.45	18.16	18.21	18.19	nan	nan
25.47	7.72	12.21	18.43	18.68	18.79	18.92	nan	nan
19.34	6.27	11.64	18.29	18.63	18.75	18.85	nan	nan
145.17	30.36	11.9	17.7	17.62	17.78	17.84	nan	nan
273.59	41.86	4.77	14.97	15.1	15.01	15.26	14.37	14.25
245.4	50.14	6.14	17.06	17.58	17.7	17.81	nan	nan
15.32	1.19	3.86	16.22	16.44	16.55	16.62	16.31	nan
105.99	78.08	14.36	17.46	16.26	16.19	16.05	14.61	14.58
215.36	53.08	13.18	19.19	18.87	18.77	18.73	nan	nan
35.84	29.38	12.23	18.09	17.8	17.86	17.86	nan	nan
123.06	36.61	8.67	18.56	17.22	16.9	16.34	13.72	13.61
129.69	33.83	11.17	17.43	17.91	18.1	18.17	nan	nan
239.37	48.84	4.78	16.01	16.74	16.91	17.13	nan	nan
127.14	34.87	13.6	19.17	18.99	19.12	19.21	nan	nan
123.49	32.32	11.14	16.93	17.09	17.33	17.35	nan	nan
0.27	35.46	10.92	18.72	18.08	17.93	17.16	14.08	13.85
28.56	2.02	11.69	15.3	15.09	15.4	15.3	nan	nan
234.07	50.23	11.65	16.16	15.83	15.98	15.9	nan	nan
345.99	33.99	3.24	15.72	15.52	15.23	15.4	14.17	14.25
132.12	52.24	13.05	18.48	18.17	18.24	18.22	nan	nan
197.4	55.96	13.59	19.1	18.92	19.1	19.0	nan	nan
138.35	32.04	6.82	17.18	18.29	18.25	18.07	15.16	14.37
24.74	6.09	9.21	19.24	18.47	18.21	17.61	14.88	14.8
12.06	5.08	9.56	17.37	17.98	18.13	18.22	nan	nan
283.88	38.68	6.01	16.17	16.12	16.06	16.23	14.92	14.81
339.75	32.86	9.31	19.55	18.06	17.74	17.23	14.62	14.61
38.13	35.48	nan	16.95	16.92	16.9	17.25	nan	nan
23.62	2.07	11.45	14.89	14.76	15.09	15.01	14.82	14.72

R.A.	Dec	Abs. mag (r)	$J0395$	r	$J0660$	i	$WISE1$	$WISE2$
245.42	48.21	13.51	18.94	18.7	18.79	18.71	nan	nan
133.04	33.6	7.71	19.3	19.01	18.64	19.13	nan	nan
183.6	55.04	5.7	16.31	17.13	17.3	17.63	nan	nan
37.82	28.99	12.91	15.44	14.98	15.03	14.96	14.15	14.13
121.22	30.27	5.99	17.06	17.81	17.95	18.1	nan	nan
25.01	6.66	8.53	19.77	19.02	18.88	18.86	16.0	15.99
114.28	41.21	11.99	16.07	15.89	16.15	16.06	nan	nan
222.92	46.63	12.08	19.09	19.19	19.11	19.03	nan	nan
109.14	39.6	11.72	18.5	18.65	18.78	19.11	nan	nan
341.13	13.58	11.53	18.67	18.75	18.89	19.15	nan	nan
333.33	29.43	14.38	18.74	18.16	18.15	18.1	nan	nan
331.09	32.64	7.8	16.57	17.28	17.45	17.58	nan	nan
112.37	39.17	11.62	16.11	15.96	16.27	16.2	16.23	16.21
339.41	32.11	14.11	19.28	18.66	18.68	18.69	nan	nan
342.4	33.62	11.47	20.34	19.11	18.78	17.85	14.59	14.4
238.81	56.79	8.51	16.83	17.47	17.61	17.63	nan	nan
244.44	42.97	8.43	19.61	18.93	18.69	18.52	nan	nan
31.67	7.1	6.74	17.53	18.17	18.24	18.55	nan	nan
5.68	6.17	6.65	17.26	17.55	17.56	17.65	nan	nan
131.48	39.25	2.72	15.16	15.81	15.47	16.13	14.89	14.84
112.43	39.44	8.81	17.93	18.57	18.73	18.96	nan	nan
136.0	37.67	9.29	17.03	17.73	17.98	18.07	nan	nan
340.97	33.82	2.39	15.24	15.6	15.74	15.86	15.8	16.0
117.18	38.71	10.76	19.61	17.8	17.33	16.49	13.43	13.24
109.38	41.85	9.76	19.77	18.09	17.8	17.12	14.3	14.24
123.97	32.81	6.94	17.64	17.92	17.88	17.74	16.29	nan
1.43	36.83	7.03	17.79	18.08	18.15	18.33	nan	nan
22.75	40.09	nan	16.46	16.98	16.98	16.88	15.81	15.71
256.47	26.1	14.12	17.87	16.82	16.74	16.53	nan	nan
130.08	40.46	10.14	17.71	18.27	18.52	18.69	nan	nan
282.74	39.49	12.37	19.26	19.27	19.32	19.59	nan	nan
23.3	5.65	12.11	19.43	18.73	18.67	17.95	15.02	14.82
284.43	39.52	3.71	15.13	15.77	15.92	16.13	nan	nan
31.65	34.3	8.09	15.85	16.57	16.67	16.9	17.02	nan
123.48	33.28	11.14	17.36	17.42	17.65	17.73	nan	nan
1.31	2.86	12.45	18.12	18.27	18.42	18.39	nan	nan
223.84	56.93	11.39	14.98	14.97	15.29	15.23	15.34	15.26
236.53	56.85	12.0	18.33	18.36	18.4	18.55	nan	nan
120.39	36.3	13.25	18.19	17.85	17.82	17.59	nan	nan
122.46	31.11	11.82	18.43	18.62	18.8	18.97	nan	nan
39.28	6.92	12.98	18.89	16.65	15.98	14.77	11.2	10.99
255.32	24.06	5.56	17.48	18.11	18.25	18.4	nan	nan
31.89	33.52	14.28	18.62	17.52	17.49	17.39	nan	nan
277.41	42.25	12.41	18.75	18.66	18.76	18.81	nan	nan
332.2	12.36	7.55	17.77	17.12	16.94	16.69	14.44	14.37
16.35	1.44	11.0	17.57	17.98	18.07	18.28	nan	nan
331.17	9.9	11.25	17.32	17.41	17.62	17.56	nan	nan
229.93	53.46	9.85	18.5	17.45	17.1	16.47	13.77	13.6
5.9	6.72	13.28	18.95	18.54	18.54	18.55	nan	nan
119.76	31.01	8.98	18.56	19.03	18.81	19.01	nan	nan

R.A.	Dec	Abs. mag (r)	$J0395$	r	$J0660$	i	$WISE1$	$WISE2$
116.93	40.02	13.0	18.99	18.89	18.91	19.06	nan	nan
239.68	49.67	6.31	19.03	18.82	18.64	18.91	nan	nan
116.1	78.61	13.21	18.74	18.79	18.83	18.92	nan	nan
1.52	7.92	13.04	18.09	17.99	17.99	18.07	nan	nan
122.41	31.27	7.66	19.06	18.54	18.27	17.45	14.2	14.11
14.43	4.6	11.03	18.16	17.2	17.01	16.22	13.24	13.06
125.07	32.03	9.45	19.8	19.36	19.18	19.16	15.95	15.8
206.84	27.12	10.02	17.89	16.62	16.35	15.93	13.4	13.29
256.41	24.33	11.34	17.89	18.26	18.36	18.55	nan	nan
127.37	30.32	12.57	18.63	18.83	18.83	19.03	nan	nan
274.77	42.26	11.6	18.96	19.22	19.33	19.35	nan	nan
152.77	30.26	8.51	18.8	18.66	18.44	18.61	nan	nan
128.09	33.27	13.33	19.32	19.04	18.97	19.06	nan	nan
349.04	23.13	7.07	18.14	18.89	18.99	19.25	nan	nan
280.1	29.88	11.39	18.67	19.03	19.25	19.32	nan	nan
278.22	42.26	11.04	17.62	18.15	18.28	18.32	nan	nan
236.18	52.12	10.0	19.28	18.26	17.91	17.24	14.47	14.34
241.29	50.0	13.25	18.42	18.47	18.5	18.59	nan	nan
5.32	7.94	9.21	19.53	19.61	19.28	19.54	15.56	14.85
281.34	40.93	10.82	15.85	16.28	16.51	16.52	nan	nan
20.96	4.77	9.89	17.94	18.29	18.45	18.59	nan	nan
18.47	3.21	5.49	17.14	17.21	17.03	17.46	16.01	16.07
36.15	37.34	9.2	18.2	18.42	18.32	18.38	nan	nan
336.18	11.25	9.92	18.18	16.96	16.6	15.93	13.0	12.94
8.03	3.39	12.3	19.31	17.87	17.52	16.56	13.38	13.21
17.22	5.72	10.49	18.75	17.48	17.12	16.3	13.27	13.05
11.61	1.77	11.23	18.45	18.62	18.71	18.84	nan	nan
337.66	12.94	13.9	17.36	17.03	17.18	17.04	16.39	nan
241.73	42.76	8.45	18.1	18.29	18.28	18.04	15.54	15.31
39.55	45.15	8.8	19.39	17.85	17.6	17.16	14.58	14.65
39.53	33.03	11.48	16.96	17.22	17.33	17.48	nan	nan
254.94	22.94	2.74	14.64	14.94	15.06	15.17	15.08	15.44
278.38	41.65	6.81	18.78	19.2	19.09	18.96	17.69	nan
237.36	48.04	14.02	17.75	17.13	17.12	17.1	nan	nan
330.8	29.65	11.24	17.38	17.79	17.89	17.9	nan	nan
142.98	39.77	10.41	17.27	17.37	17.32	16.79	14.01	13.9
266.04	31.91	11.59	18.62	18.86	18.95	18.95	nan	nan
122.11	32.04	4.32	13.31	13.9	14.03	14.21	14.46	14.59
131.35	38.03	12.94	16.25	15.97	16.07	15.99	nan	nan
283.73	38.31	9.73	19.05	18.04	17.71	17.07	14.2	14.15
340.33	9.82	10.44	17.62	18.12	18.18	18.36	nan	nan
36.93	44.41	11.52	16.05	15.99	16.34	16.27	nan	nan
123.4	32.1	9.68	18.68	17.36	17.02	16.38	13.66	13.5
343.14	10.34	7.15	18.15	17.31	16.92	17.0	14.91	14.77
183.25	43.23	10.46	17.89	17.48	17.34	16.72	14.0	13.88
127.73	31.99	9.54	19.31	19.07	18.91	18.36	15.68	15.57
260.0	33.27	10.36	16.92	17.41	17.62	17.72	nan	nan
123.74	34.63	13.92	18.44	18.08	18.09	18.04	nan	nan
335.07	12.92	4.73	16.8	17.07	17.22	17.33	nan	nan
133.62	38.14	11.7	18.48	18.72	18.73	18.85	nan	nan

R.A.	Dec	Abs. mag (r)	$J0395$	r	$J0660$	i	$WISE1$	$WISE2$
151.84	30.15	11.48	19.42	18.31	18.06	17.06	14.1	13.96
149.41	30.03	9.57	18.59	18.78	18.7	18.37	15.7	15.59
116.38	45.64	11.04	18.94	18.92	18.48	18.79	nan	nan
244.14	54.17	13.47	18.69	18.33	18.35	18.22	16.58	16.47
340.09	12.09	6.1	16.33	16.95	17.07	17.3	nan	nan
244.64	54.0	9.37	17.93	18.49	18.73	18.81	nan	nan
18.43	3.55	10.77	18.02	17.59	17.34	16.61	13.51	13.33
33.69	44.87	13.01	19.26	19.08	19.04	18.98	nan	nan
153.63	40.85	7.45	19.39	18.34	18.07	17.49	14.88	14.77
130.8	39.75	4.21	13.77	14.52	14.67	14.87	15.27	15.24
26.23	1.62	9.37	17.24	17.9	18.08	18.26	nan	nan
136.43	30.72	10.36	17.63	16.43	16.02	15.26	12.34	12.23
138.98	53.42	13.69	14.14	13.75	13.76	13.8	nan	nan
284.9	40.57	3.92	17.6	17.56	17.31	17.41	16.4	16.49
154.91	31.65	14.01	18.99	18.56	18.44	18.28	nan	nan
239.81	48.39	12.56	18.33	18.5	18.55	18.65	nan	nan
331.64	12.99	11.35	18.4	18.7	18.87	18.9	nan	nan
277.88	42.04	6.92	17.11	17.53	17.62	17.7	nan	nan
19.24	7.52	11.14	17.3	17.65	17.74	17.86	nan	nan
257.73	32.33	12.9	18.13	18.07	18.1	18.12	nan	nan
188.64	56.11	12.0	18.07	18.19	18.25	18.49	16.73	15.92
255.44	22.89	10.21	17.09	17.6	17.82	17.94	nan	nan
30.1	7.25	13.66	19.04	18.61	18.66	18.77	nan	nan
280.5	30.81	9.94	18.3	18.94	19.17	19.62	nan	nan
332.09	29.04	5.13	14.84	15.43	15.59	15.73	nan	nan
151.14	40.24	12.37	18.16	18.42	18.54	18.5	nan	nan
241.42	46.18	7.91	17.9	16.59	16.36	16.0	13.64	13.6
273.52	30.83	3.26	17.23	17.28	17.06	16.95	16.48	nan
133.09	33.02	4.85	16.57	16.9	17.04	17.15	nan	nan
10.61	4.5	12.45	18.65	18.51	18.55	18.72	nan	nan
1.31	35.28	10.08	17.93	18.58	18.75	19.0	nan	nan
239.54	48.94	12.89	19.11	18.92	18.74	19.0	nan	nan
243.22	42.82	10.83	17.7	18.03	18.17	18.34	nan	nan
130.91	36.57	9.78	19.16	17.85	17.51	16.86	14.02	13.85
227.96	56.41	12.54	16.59	16.33	16.5	16.39	nan	nan
120.56	40.18	6.19	16.55	16.64	16.56	16.63	nan	nan
278.41	40.67	9.15	18.08	18.64	18.77	18.57	nan	nan
6.76	4.12	9.94	18.48	17.65	17.32	16.69	13.84	13.66
127.66	40.85	11.02	16.04	16.07	16.35	16.33	nan	nan
201.8	57.14	8.38	19.04	19.29	19.12	19.23	16.47	15.55
224.78	55.52	11.71	18.51	18.84	18.65	18.94	nan	nan
40.28	34.63	9.24	17.17	17.88	18.12	18.26	nan	nan
15.24	3.06	10.71	17.72	18.1	18.27	18.41	nan	nan
39.67	28.15	13.25	18.34	18.15	18.17	18.24	nan	nan
7.16	6.92	10.01	17.53	18.06	18.19	18.41	nan	nan
36.99	33.98	12.16	17.91	18.04	18.06	18.19	nan	nan
37.53	32.24	12.76	16.77	16.61	16.74	16.64	nan	nan
28.98	1.59	13.87	18.89	18.5	18.49	18.57	nan	nan
8.0	4.04	12.05	18.0	18.18	18.25	18.32	nan	nan
130.1	34.53	14.08	18.84	18.45	18.4	18.43	nan	nan

R.A.	Dec	Abs. mag (*r*)	*J*0395	*r*	*J*0660	*i*	*WISE*1	*WISE*2
131.34	55.82	9.44	17.44	18.09	18.28	18.56	nan	nan
239.1	57.53	6.66	19.07	18.36	17.42	18.23	nan	nan
273.41	41.97	10.99	20.0	18.62	18.33	17.91	15.34	15.21
35.28	33.88	10.26	17.49	17.45	17.26	16.9	14.51	14.47
113.73	41.09	10.18	17.72	17.17	16.96	16.25	13.45	13.32
13.31	39.45	13.2	16.97	16.59	16.64	16.53	nan	nan
130.6	37.98	8.19	17.24	18.17	18.35	18.47	nan	nan
18.17	3.11	10.79	17.68	18.1	18.35	18.33	nan	nan
157.67	40.22	7.75	17.05	17.87	18.05	18.23	nan	nan
22.61	8.09	13.93	19.76	19.55	19.42	19.41	nan	nan
130.49	40.25	7.9	16.96	17.91	18.07	18.0	nan	nan
122.3	35.47	12.38	15.38	15.11	15.27	15.19	14.7	14.73
115.05	38.99	11.16	19.35	19.17	18.98	18.66	16.08	15.8
282.39	40.34	11.13	14.77	14.94	15.23	15.23	nan	nan
273.33	30.19	4.83	15.15	15.7	15.82	16.0	16.15	16.42
284.97	39.18	5.32	18.94	17.55	16.67	17.39	nan	nan
267.01	32.48	12.74	19.18	19.1	19.09	19.28	nan	nan
124.9	31.24	4.53	15.14	15.81	15.97	16.14	16.49	nan
3.89	6.2	13.57	18.61	18.82	18.92	18.9	nan	nan
265.92	31.8	10.14	18.88	18.47	18.22	17.59	14.73	14.63
332.64	9.85	12.38	17.03	15.55	15.14	14.21	nan	nan
237.03	48.49	9.78	19.66	18.15	18.0	17.69	15.4	15.31
164.98	40.73	8.56	17.63	18.68	18.99	19.1	nan	nan
136.94	38.95	10.63	16.16	16.62	16.86	16.89	nan	nan
18.32	6.06	13.84	18.69	18.54	18.59	18.51	nan	nan
33.45	45.17	6.37	17.52	17.98	17.89	17.76	nan	nan
31.06	7.44	11.16	16.28	16.5	16.81	16.8	nan	nan
38.22	44.19	4.9	13.88	14.46	14.6	14.79	15.26	15.38
106.62	39.51	nan	19.14	17.6	17.26	16.34	nan	nan
348.08	33.38	13.13	19.29	19.38	19.53	19.58	nan	nan
130.27	39.39	10.82	16.38	16.73	16.93	16.99	nan	nan
155.48	40.84	10.94	16.28	16.63	16.87	16.94	16.29	15.98
331.6	13.43	10.97	17.7	17.97	18.04	18.23	nan	nan
27.96	5.28	10.99	17.23	17.7	17.83	18.02	nan	nan
134.38	40.27	10.68	14.64	15.0	15.25	15.32	nan	nan
334.79	10.08	9.56	18.17	18.76	18.84	19.08	nan	nan
240.69	43.93	12.61	19.36	19.14	18.88	19.0	nan	nan
158.72	39.52	11.54	17.84	18.2	18.36	18.48	nan	nan
35.56	45.38	nan	19.48	18.65	18.3	17.98	15.16	15.04
135.32	30.18	8.21	17.61	18.45	18.53	18.66	nan	nan
227.3	55.54	12.42	17.56	17.64	17.68	17.82	nan	nan
22.16	33.84	9.09	19.81	18.43	18.2	17.57	14.85	14.9
242.84	52.77	4.81	12.35	12.98	13.11	13.29	13.63	13.69
38.23	37.07	5.42	15.49	15.97	16.06	16.13	nan	nan
341.28	34.03	9.8	18.63	19.35	19.32	19.79	nan	nan
131.59	55.11	6.3	17.78	17.47	17.34	17.12	15.14	15.32
236.24	45.26	8.08	15.72	16.48	16.62	16.83	nan	nan
264.03	31.98	5.63	16.59	17.16	17.25	17.36	nan	nan
274.46	41.34	5.9	17.19	17.78	17.87	18.18	nan	nan
106.62	38.61	9.57	19.72	18.33	18.06	17.42	14.75	14.62

R.A.	Dec	Abs. mag (r)	$J0395$	r	$J0660$	i	$WISE1$	$WISE2$
236.2	45.84	9.39	17.05	17.75	17.98	18.12	nan	nan
134.62	40.18	8.37	18.6	19.17	19.01	18.94	16.3	15.12
282.38	39.62	4.39	17.0	17.66	17.76	18.01	nan	nan
109.26	39.89	7.74	15.84	16.8	16.95	17.06	16.36	nan
278.5	39.74	11.77	17.93	18.18	18.25	18.36	nan	nan
21.53	33.28	9.55	16.66	17.41	17.58	17.73	nan	nan
332.84	33.78	5.98	17.37	17.91	18.03	18.23	nan	nan
38.19	35.74	4.76	16.25	14.68	14.63	20.27	12.97	12.97
21.13	6.82	5.76	15.98	16.68	16.83	16.99	17.13	nan
282.86	40.91	1.49	17.84	14.46	13.84	11.48	4.84	4.3
188.96	42.38	4.71	11.59	12.17	12.34	12.51	12.89	12.96
120.94	30.75	3.32	14.84	15.29	15.45	15.58	15.76	16.02
194.93	57.4	8.83	16.33	17.17	17.39	17.56	nan	nan
337.41	32.42	10.69	18.23	18.73	18.83	19.2	nan	nan
130.77	33.46	4.5	14.46	15.06	15.21	15.35	nan	nan
340.73	11.76	4.93	12.58	11.61	10.97	14.72	12.83	12.69
276.97	40.88	9.5	18.16	16.45	15.21	15.39	12.08	11.72
14.88	41.4	9.88	17.36	18.09	18.09	18.41	nan	nan
130.26	39.94	4.84	14.99	15.62	15.82	15.97	16.18	nan
343.3	33.08	5.91	16.69	17.26	17.42	17.56	nan	nan
277.61	31.09	5.36	16.15	16.57	16.67	16.74	15.58	15.59
276.13	30.9	10.04	18.69	17.43	17.04	16.28	13.37	13.2
341.18	12.43	11.78	17.81	18.13	18.28	18.35	nan	nan
10.55	7.53	9.53	18.18	18.68	18.08	18.48	16.65	nan
109.7	40.85	8.07	16.14	18.7	18.64	18.76	nan	nan
1.77	6.43	11.31	16.0	16.42	16.64	16.7	nan	nan
14.39	4.93	8.64	18.13	16.99	16.58	16.58	13.88	13.81
6.73	6.59	13.3	17.49	17.13	17.27	17.11	16.39	nan
136.48	30.09	10.05	18.42	17.65	17.4	16.91	13.95	13.81
27.71	33.44	8.99	17.9	18.04	17.38	17.7	16.25	nan
277.26	30.53	4.51	14.93	15.47	15.62	15.77	15.94	16.4
121.25	35.22	12.07	18.51	18.83	18.71	18.91	nan	nan
131.15	39.95	11.94	17.48	17.75	17.84	17.89	nan	nan
39.38	44.98	12.05	17.86	18.08	18.2	18.26	nan	nan
261.03	56.33	8.57	15.91	16.56	16.67	16.73	14.97	14.79
108.29	40.21	10.31	19.69	18.26	17.93	17.46	14.45	14.36
121.0	40.33	11.74	19.17	19.83	19.82	19.67	nan	nan
122.03	33.73	13.02	18.19	18.12	18.11	18.25	nan	nan
128.5	36.99	12.58	16.35	16.06	16.23	16.13	nan	nan
17.73	5.76	11.9	17.64	18.04	18.06	18.24	nan	nan
236.79	53.12	10.59	18.86	18.0	17.54	16.8	13.79	13.6
130.72	34.41	11.45	16.3	16.4	16.7	16.69	nan	nan
26.64	7.98	12.44	18.31	18.43	18.51	18.48	nan	nan
336.1	10.62	6.83	17.58	18.11	18.1	18.36	nan	nan
330.35	9.67	11.19	17.62	18.01	18.12	18.31	nan	nan
7.29	6.43	6.05	16.95	17.57	17.65	17.86	nan	nan
107.32	39.68	11.33	16.31	16.71	16.79	16.98	nan	nan
347.56	34.03	4.2	14.9	15.63	15.76	15.99	16.35	nan
278.45	39.76	4.81	16.15	16.73	16.89	17.06	nan	nan
4.23	7.08	4.78	15.7	16.28	16.4	16.57	15.95	nan

R.A.	Dec	Abs. mag (r)	$J0395$	r	$J0660$	i	$WISE1$	$WISE2$
120.87	34.36	4.31	14.62	15.29	15.43	15.61	16.08	16.14
27.24	2.54	13.39	17.0	16.66	16.63	16.67	nan	nan
137.53	52.13	5.82	19.22	17.93	16.86	17.73	16.38	nan
257.25	23.54	13.97	18.99	18.66	18.61	18.65	nan	nan
125.69	36.24	11.18	15.51	15.75	16.05	16.01	15.52	15.37
0.88	35.09	11.86	18.58	18.59	18.68	18.71	nan	nan
134.74	32.14	11.98	19.26	19.18	18.98	18.21	15.27	15.03
39.72	43.39	5.2	16.6	17.24	17.36	17.52	nan	nan
8.57	39.61	12.08	17.09	17.31	17.38	17.5	nan	nan
277.92	31.11	8.73	18.13	18.07	17.95	17.67	15.09	15.28
135.67	32.36	6.79	18.94	18.32	18.36	18.36	17.42	nan
14.88	2.37	13.18	18.97	19.05	19.06	19.17	nan	nan
28.89	7.72	10.91	17.56	17.89	18.04	18.16	nan	nan
243.11	42.85	9.5	17.24	17.92	18.02	18.25	nan	nan
340.87	10.78	4.81	14.53	15.22	15.38	15.56	15.98	nan
140.57	30.67	11.02	17.41	16.28	15.86	15.07	12.11	11.93
342.48	11.68	12.62	17.43	17.52	17.58	17.66	nan	nan
259.75	56.4	12.62	19.17	19.16	19.04	19.19	nan	nan
242.65	44.18	4.94	14.48	15.06	15.2	15.41	15.63	15.74
282.23	40.26	4.71	16.94	17.68	17.85	18.0	nan	nan
241.34	43.08	9.65	14.38	15.06	15.26	15.41	15.93	16.05
343.8	9.61	10.13	17.17	16.54	16.23	15.52	12.63	12.47
213.69	56.56	11.42	17.91	18.2	18.26	18.46	nan	nan
213.96	53.61	4.92	16.3	17.03	17.2	17.37	nan	nan
197.48	55.06	12.98	18.88	18.57	18.59	18.72	nan	nan
124.89	32.4	10.46	17.68	18.14	18.27	18.48	nan	nan
240.89	51.81	5.9	17.25	17.95	18.07	18.26	nan	nan
121.62	32.52	4.88	15.04	15.61	15.76	15.92	15.97	15.73
259.93	33.32	12.48	18.65	18.91	19.01	19.08	nan	nan
235.51	50.43	10.39	16.56	17.18	17.33	17.5	nan	nan
136.2	31.55	4.8	14.59	15.36	15.51	15.7	16.25	nan
25.51	3.2	12.4	19.05	18.92	18.52	19.1	16.71	nan
245.79	42.98	6.51	17.3	17.96	18.13	18.31	nan	nan
233.07	45.77	6.29	16.41	16.64	16.7	16.72	15.71	15.83
2.88	2.14	13.65	19.2	18.94	18.75	18.97	nan	nan
134.15	37.65	11.76	19.83	19.01	18.72	17.93	15.02	14.88
38.55	35.73	5.32	17.22	15.73	15.67	20.45	14.12	14.24
335.37	30.42	4.73	14.87	15.56	15.71	15.9	15.87	15.62
263.76	32.61	4.97	14.8	15.37	15.53	15.68	15.78	15.99
258.62	22.79	4.16	14.32	14.96	15.13	15.31	15.78	15.92
33.93	33.67	4.37	13.42	13.94	14.08	14.25	14.46	14.59
263.97	32.29	5.3	12.28	17.26	17.24	17.11	15.91	16.23
107.63	38.27	8.38	20.01	18.82	18.45	17.8	14.99	15.08
341.88	33.81	7.81	20.22	19.44	19.15	19.67	16.44	15.78
121.26	40.99	1.65	17.0	12.83	12.27	10.41	nan	nan
4.68	2.56	12.78	17.21	17.15	17.14	17.28	17.21	nan
33.96	29.35	5.66	13.69	14.15	14.3	14.44	14.58	14.67
116.28	38.19	4.11	14.46	15.04	15.17	15.29	nan	nan
257.98	23.02	10.9	14.44	14.99	15.14	15.29	nan	nan
35.28	45.54	9.69	19.12	18.2	17.97	17.59	15.04	15.0

R.A.	Dec	Abs. mag (r)	$J0395$	r	$J0660$	i	$WISE1$	$WISE2$
231.65	48.97	12.57	17.92	18.2	18.23	18.29	nan	nan
227.44	55.98	9.81	13.84	15.7	12.11	11.94	11.76	11.67
135.67	36.75	11.1	17.37	17.71	17.83	17.93	nan	nan
342.2	10.44	13.79	19.02	18.53	18.46	18.49	nan	nan
115.01	39.78	3.2	15.0	15.78	15.92	16.15	nan	nan
110.0	40.36	11.14	14.59	15.02	15.12	15.3	nan	nan
5.57	2.53	11.73	17.53	17.75	17.83	18.07	nan	nan
122.19	31.52	7.4	18.76	18.46	17.75	17.97	15.53	15.46
134.31	33.31	9.59	18.56	18.6	18.48	18.11	15.46	15.61
330.18	33.38	0.88	18.09	13.6	13.47	11.15	nan	nan
138.64	58.21	8.68	17.27	17.99	18.07	18.21	nan	nan
34.0	35.69	11.25	15.17	15.92	16.07	16.27	16.56	16.12
38.93	7.5	14.19	18.93	18.7	18.68	18.58	nan	nan
38.98	35.93	6.77	16.79	17.37	17.41	17.39	nan	nan
150.98	40.57	3.58	12.72	13.5	13.66	13.87	14.38	14.48
136.98	56.0	12.37	18.9	19.13	19.24	19.18	nan	nan
126.02	31.08	13.14	17.81	17.58	17.6	17.63	nan	nan
124.73	37.5	10.78	16.35	16.69	16.95	17.0	nan	nan
132.15	31.34	12.36	18.02	18.36	18.41	18.51	nan	nan
16.15	41.3	7.13	13.92	13.61	13.3	13.31	10.87	10.73
216.9	53.81	11.57	14.85	15.13	15.29	15.35	nan	nan
40.01	45.46	12.35	17.7	17.63	17.76	17.86	nan	nan
279.27	40.36	11.63	19.03	18.34	18.17	17.53	14.72	14.54
279.55	30.59	12.27	18.74	18.88	18.9	19.11	nan	nan
132.3	40.61	12.8	18.32	18.25	18.19	18.58	nan	nan
37.45	35.3	4.46	17.33	16.11	16.08	20.74	14.7	14.67
37.76	27.72	5.12	14.7	15.3	15.42	15.61	15.96	nan
284.86	40.46	10.88	18.47	19.1	19.12	19.61	nan	nan
3.02	2.02	6.29	16.92	16.88	16.77	16.94	16.12	16.01
39.25	36.75	10.06	17.52	17.97	18.12	18.31	nan	nan
226.84	52.51	10.44	16.9	17.05	16.67	17.56	16.51	16.37
168.97	41.05	10.32	15.09	15.48	15.72	15.78	nan	nan
109.57	37.53	12.56	16.45	17.21	17.33	17.67	nan	nan
27.29	33.45	8.15	19.51	19.31	18.1	19.23	nan	nan
335.81	13.65	11.37	15.4	15.79	16.05	16.1	16.59	nan
330.7	27.84	8.81	16.0	16.79	16.95	17.22	nan	nan
282.7	41.75	11.3	19.26	17.65	17.27	16.3	12.99	12.87
121.55	33.74	11.47	16.12	16.47	16.55	16.69	16.73	nan
334.13	29.01	8.53	17.16	16.5	16.04	15.93	12.41	12.27
331.05	26.42	4.38	14.15	14.77	14.95	15.1	15.42	15.44
206.8	56.35	12.06	17.94	18.09	18.08	18.22	nan	nan
127.12	36.57	11.31	17.0	17.38	17.48	17.57	nan	nan
278.76	41.16	7.2	19.79	19.38	19.19	18.79	15.79	15.87
130.48	37.39	11.8	17.82	17.96	18.02	18.14	nan	nan
259.18	30.97	11.69	17.87	18.07	18.16	18.31	nan	nan
115.45	38.6	13.13	20.19	19.76	19.39	18.92	15.81	15.55
39.2	30.85	5.08	13.82	14.2	14.34	14.49	14.59	14.63
128.56	40.05	10.25	19.69	19.49	19.27	18.7	15.64	15.6
343.97	32.89	5.0	15.52	14.94	11.59	13.11	nan	nan
337.54	10.03	13.25	17.82	17.62	17.72	17.66	nan	nan

R.A.	Dec	Abs. mag (r)	$J0395$	r	$J0660$	i	$WISE1$	$WISE2$
7.7	3.78	13.88	16.73	16.09	16.05	16.01	nan	nan
211.88	53.4	12.54	18.07	18.17	18.25	18.25	nan	nan
39.86	35.32	2.98	14.76	14.71	10.83	14.58	nan	nan
257.29	23.33	12.21	17.25	17.43	17.47	17.57	nan	nan
35.62	28.5	10.75	16.94	17.36	17.49	17.41	15.09	14.84
183.05	54.87	13.0	17.95	17.87	17.96	18.12	nan	nan
12.76	4.94	11.74	17.49	17.82	17.91	17.93	nan	nan
114.32	41.44	9.6	17.9	17.09	16.77	16.33	13.73	13.58
23.24	2.19	9.6	16.15	16.84	17.0	17.18	nan	nan
19.49	44.06	12.63	17.07	16.82	16.93	16.87	16.36	16.38
262.47	32.39	0.35	16.51	13.2	12.88	11.13	6.56	6.47
332.4	12.39	11.36	17.15	17.45	17.58	17.71	nan	nan
258.9	33.22	9.89	14.34	14.64	14.87	14.93	nan	nan
16.21	7.18	nan	19.06	18.23	17.96	17.3	14.43	14.3
137.3	54.72	8.31	19.13	19.43	18.69	19.35	16.08	14.72
106.03	40.33	10.69	18.83	19.65	19.68	20.0	nan	nan
23.98	7.82	11.12	16.15	16.66	16.92	17.01	nan	nan
267.94	31.68	11.14	18.59	19.07	19.28	19.48	nan	nan
275.9	41.07	11.23	14.09	14.42	14.57	14.67	nan	nan
258.42	32.67	13.12	17.49	17.33	17.35	17.39	nan	nan
243.96	45.68	11.66	19.17	18.5	18.29	17.36	14.22	13.96
227.38	52.84	5.85	19.07	18.13	16.18	18.02	16.79	nan
233.59	53.04	13.39	18.85	18.48	18.33	18.58	nan	nan
25.5	7.56	11.53	18.22	18.67	18.65	18.89	nan	nan
169.34	41.0	12.59	18.13	18.23	18.27	18.39	nan	nan
343.56	32.4	14.48	18.78	17.58	17.48	17.38	15.77	15.92
109.29	74.01	10.23	14.95	15.22	15.46	15.45	14.0	13.76
133.43	57.81	10.51	15.91	16.41	15.52	16.35	13.88	13.55
132.65	32.13	12.02	17.22	17.33	17.47	17.52	nan	nan
112.54	30.37	10.73	18.87	17.58	17.2	16.51	13.61	13.47
333.76	33.45	2.1	17.13	13.61	13.2	11.47	6.3	6.03
222.82	52.84	3.49	14.64	15.48	15.6	15.87	16.42	16.55
139.82	29.74	nan	18.84	18.82	18.78	18.26	15.85	15.73
236.45	48.42	4.59	13.16	15.32	12.05	12.12	nan	nan
26.97	2.86	11.95	16.64	16.83	16.88	17.0	nan	nan
283.37	42.06	11.76	18.78	19.02	18.65	19.06	nan	nan
121.87	32.7	11.5	17.82	18.1	18.04	18.2	nan	nan
330.18	28.14	1.26	14.49	14.94	15.06	15.19	15.23	15.32
256.3	24.17	5.74	17.23	17.93	18.07	18.34	nan	nan
125.34	37.14	12.52	18.7	18.74	18.64	18.76	nan	nan
122.45	32.36	10.81	18.79	17.13	16.75	15.83	12.69	12.54
241.97	47.88	7.14	19.43	18.38	16.68	18.18	16.91	nan
276.73	42.8	9.6	19.62	18.73	18.43	17.82	15.11	15.0
334.94	12.6	11.85	16.67	16.92	17.01	17.13	nan	nan
12.16	8.05	8.53	14.97	15.74	15.91	16.12	16.52	nan
137.05	53.86	12.23	17.42	17.58	17.64	17.77	nan	nan
239.72	44.09	11.08	17.92	16.55	15.87	15.3	12.4	12.19
22.7	39.09	12.07	17.87	17.96	17.99	18.08	nan	nan
140.53	31.05	8.57	18.44	18.39	17.95	17.94	15.71	15.41
331.94	31.48	6.8	16.76	17.62	14.56	14.4	16.15	nan

Bibliography

Abril, Javier et al. (Feb. 2020). “Disentangling cataclysmic variables in Gaia’s HR diagram”. In: 492.1, pp. L40–L44. DOI: `10.1093/mnrasl/slz181`. arXiv: `1912.01531 [astro-ph.SR]`.

Akras, Stavros, Lizette Guzman-Ramirez, and Denise R. Gonçalves (2019). “Compact planetary nebulae: Improved IR diagnostic criteria based on classification tree modelling”. In: p. 1843. DOI: `10.1093/mnras/stz1911`. arXiv: `1907.10026 [astro-ph.SR]`.

Alam, Shadab et al. (2015). “The Eleventh and Twelfth Data Releases of the Sloan Digital Sky Survey: Final Data from SDSS-III”. In: 219.1, 12, p. 12. DOI: `10.1088/0067-0049/219/1/12`. arXiv: `1501.00963 [astro-ph.IM]`.

Anupama, G. C. (Dec. 2008). “The Recurrent Nova Class of Objects”. In: *RS Ophiuchi (2006) and the Recurrent Nova Phenomenon*. Ed. by A. Evans et al. Vol. 401. Astronomical Society of the Pacific Conference Series, p. 31.

Armitage, P. J. and M. Livio (Oct. 1996). “Accretion Disks in Interacting Binaries: Simulations of the Stream-Disk Impact”. In: 470, p. 1024. DOI: `10.1086/177928`. arXiv: `astro-ph/9606038 [astro-ph]`.

Astraatmadja, Tri L. and Coryn A. L. Bailer-Jones (2016). “Estimating Distances from Parallaxes. II. Performance of Bayesian Distance Estimators on a Gaia-like Catalogue”. In: 832.2, 137, p. 137. DOI: `10.3847/0004-637X/832/2/137`. arXiv: `1609.03424 [astro-ph.IM]`.

Bailer-Jones, C. A. L. et al. (2018). “Estimating Distance from Parallaxes. IV. Distances to 1.33 Billion Stars in Gaia Data Release 2”. In: 156.2, 58, p. 58. DOI: `10.3847/1538-3881/aacb21`. arXiv: `1804.10121 [astro-ph.SR]`.

Beuermann, K. (1998). “Magnetic Cataclysmic Variables: Observational and theoretical results”. In: *High Energy Astronomy and Astrophysics*. Ed. by P. C. Agrawal and P. R. Visvanathan. India: Universities Press, pp. 100–114.

Breedt, E. et al. (Oct. 2014). “1000 cataclysmic variables from the Catalina Real-time Transient Survey”. In: 443.4, pp. 3174–3207. DOI: `10.1093/mnras/stu1377`. arXiv: `1407.1907 [astro-ph.SR]`.

Carrasco, J. M. et al. (2016). “Gaia Data Release 1. Principles of the photometric calibration of the G band”. In: 595, A7, A7. DOI: `10.1051/0004-6361/201629235`. arXiv: `1611.02036 [astro-ph.IM]`.

Cenarro, A. J. et al. (2019). "J-PLUS: The Javalambre Photometric Local Universe Survey". In: 622, A176, A176. DOI: `10.1051/0004-6361/201833036`. arXiv: `1804.02667 [astro-ph.GA]`.

Chabrier, G. and I. Baraffe (1997). "Theory of low mass stars, brown dwarfs and extra-solar giant planets." In: *IAU Symposium*. Ed. by T. R. Bedding, A. J. Booth, and J. Davis. Vol. 189. IAU Symposium, pp. 331–340. arXiv: `astro-ph/9705059 [astro-ph]`.

Chen, A. et al. (July 2001). "Cataclysmic variables in the Edinburgh-Cape Blue Object SurveyQ3". In: 325, pp. 89–110. DOI: `10.1046/j.1365-8711.2001.04322.x`.

Chromospherically Active Binary Stars (Dec. 1994). Vol. 1181. ESA Special Publication.

Davis, P. J. et al. (2008). "How many cataclysmic variables are crossing the period gap? A test for the disruption of magnetic braking". In: 389.4, pp. 1563–1576. DOI: `10.1111/j.1365-2966.2008.13675.x`. arXiv: `0805.4700 [astro-ph]`.

de Kool, M. (July 1992). "Statistics of cataclysmic variable formation". In: 261, pp. 188–202. URL: `1992A&A...261..188D`.

Dirac, P. A. M. (Oct. 1926). "On the Theory of Quantum Mechanics". In: *Proceedings of the Royal Society of London Series A* 112.762, pp. 661–677. DOI: `10.1098/rspa.1926.0133`.

Downes, Ronald A. et al. (2001). "A Catalog and Atlas of Cataclysmic Variables: The Living Edition". In: 113.784, pp. 764–768. DOI: `10.1086/320802`. arXiv: `astro-ph/0102302 [astro-ph]`.

Eggleton, P. P. (1976). "Angular Momentum Loss and the Origin of Cataclysmic Binaries". In: *IAU Symp. 73: Structure and Evolution of Close Binary Systems*, pp. 209–121.

— (May 1983). "Approximations to the radii of Roche lobes". In: 268, pp. 368–369. URL: `1983ApJ...268..368E`.

Fermi, E. (1926). "On the Quantization of the Monoatomic Ideal Gas". In: *Rend. Lincei 3, 145s*.

Frank, Juhan, Andrew King, and Derek J. Raine (2002). *Accretion Power in Astrophysics: Third Edition*.

Gänsicke, B. T. (2004). "Observational studies of Cataclysmic Variable evolution: Of samples, biases and surprises". In: *Compact Binaries in the Galaxy and Beyond*. Ed. by G. Tovmassian and E.M. Sion. Conf. Ser. 20. Revista Mexicana de Astronomía y Astrofísica, pp. 152–154.

Gaia Collaboration et al. (2018). "Gaia Data Release 2. Summary of the contents and survey properties". In: 616, A1, A1. DOI: 10.1051/0004-6361/201833051. arXiv: 1804.09365 [astro-ph.GA].

Gänsicke, B. T., H. J. Hagen, and D. Engels (Jan. 2002). "Properties of a spectroscopically selected CV sample". In: *The Physics of Cataclysmic Variables and Related Objects*. Ed. by B. T. Gänsicke, K. Beuermann, and K. Reinsch. Vol. 261. Astronomical Society of the Pacific Conference Series, p. 190. arXiv: astro-ph/0111375 [astro-ph].

Gänsicke, B. T. et al. (July 2004). "HS 2237+8154: A new pre-CV just above the period gap". In: *Revista Mexicana de Astronomia y Astrofisica Conference Series*. Ed. by G. Tovmassian and E. Sion. Vol. 20. Revista Mexicana de Astronomia y Astrofisica Conference Series, pp. 271–271.

Gänsicke, B. T. et al. (2009). "SDSS unveils a population of intrinsically faint cataclysmic variables at the minimum orbital period". In: 397.4, pp. 2170–2188. DOI: 10.1111/j.1365-2966.2009.15126.x. arXiv: 0905.3476 [astro-ph.SR].

Gentile Fusillo, Nicola Pietro, Boris T. Gänsicke, and Sandra Greiss (Apr. 2015). "A photometric selection of white dwarf candidates in Sloan Digital Sky Survey Data Release 10". In: 448.3, pp. 2260–2274. DOI: 10.1093/mnras/stv120.

Goliasch, Jonas and Lorne Nelson (2015). "Population Synthesis of Cataclysmic Variables. I. Inclusion of Detailed Nuclear Evolution". In: 809.1, 80, p. 80. DOI: 10.1088/0004-637X/809/1/80. arXiv: 1607.06217 [astro-ph.SR].

Haberl, F. and C. Motch (May 1995). "New intermediate polars discovered in the ROSAT survey: two spectrally distinct classes." In: 297, pp. L37–L40.

Hameury, J. M. et al. (Mar. 1988). "Magnetic braking and the evolution of cataclysmic binaries". In: 231, pp. 535–547. URL: 1988mn.231..535H.

Hellier, C. (Jan. 2001). *Cataclysmic Variable Stars*. Springer.

Hind, J. R. (Jan. 1856). "On a new Variable Star". In: 16, pp. 56–56. DOI: 10.1093/mnras/16.3.56.

Howell, Steve B., Lorne A. Nelson, and Saul Rappaport (Apr. 2001). "An Exploration of the Paradigm for the 2-3 Hour Period Gap in Cataclysmic Variables". In: 550.2, pp. 897–918. DOI: 10.1086/319776. arXiv: astro-ph/0005435 [astro-ph].

Iben Icko, Jr., Masayuki Y. Fujimoto, and Jim MacDonald (Jan. 1992). "On Mass-Transfer Rates in Classical Nova Precursors". In: 384, p. 580. DOI: 10.1086/170900.

Igoshev, Andrei, Frank Verbunt, and Eric Cator (2016). “Distance and luminosity probability distributions derived from parallax and flux with their measurement errors. With application to the millisecond pulsar PSR J0218+4232”. In: 591, A123, A123. DOI: `10.1051/0004-6361/201527471`. arXiv: `1604.08452 [astro-ph.HE]`.

Kalomeni, B. et al. (2016). “Evolution of Cataclysmic Variables and Related Binaries Containing a White Dwarf”. In: 833.1, 83, p. 83. DOI: `10.3847/1538-4357/833/1/83`. arXiv: `1610.03051 [astro-ph.SR]`.

Kato, Taichi et al. (2013). “SSS J122221.7-311523: Double Superoutburst in the Best Candidate for a Period Bouncer”. In: 65, L11, p. L11. DOI: `10.1093/pasj/65.5.L11`. arXiv: `1307.5936 [astro-ph.SR]`.

Knigge, C., I. Baraffe, and J. Patterson (June 2011). “The Evolution of Cataclysmic Variables as Revealed by Their Donor Stars”. In: 194, 28, p. 28. DOI: `10.1088/0067-0049/194/2/28`. arXiv: `1102.2440 [astro-ph.SR]`.

Knigge, Christian (2006). “The donor stars of cataclysmic variables”. In: 373.2, pp. 484–502. DOI: `10.1111/j.1365-2966.2006.11096.x`. arXiv: `astro-ph/0609671 [astro-ph]`.

Kolb, U. (Apr. 1993). “A model for the intrinsic population of cataclysmic variables”. In: 271, pp. 149–166. URL: `1993A&A...271..149K`.

Lindegren, L. et al. (2018). “Gaia Data Release 2. The astrometric solution”. In: 616, A2, A2. DOI: `10.1051/0004-6361/201832727`. arXiv: `1804.09366 [astro-ph.IM]`.

Littlefair, S. P. et al. (Oct. 2007). “SDSS J150722.30+523039.8: a cataclysmic variable formed directly from a detached white dwarf/brown dwarf binary?” In: 381.2, pp. 827–834. DOI: `10.1111/j.1365-2966.2007.12285.x`. arXiv: `0708.0097 [astro-ph]`.

Littlefair, S. P. et al. (Aug. 2008). “On the evolutionary status of short-period cataclysmic variables”. In: 388.4, pp. 1582–1594. DOI: `10.1111/j.1365-2966.2008.13539.x`. arXiv: `0806.1129 [astro-ph]`.

Luri, X. et al. (2018). “Gaia Data Release 2. Using Gaia parallaxes”. In: 616, A9, A9. DOI: `10.1051/0004-6361/201832964`. arXiv: `1804.09376 [astro-ph.IM]`.

Mattei, J. A. G. (1990). “Active Close Binaries”. In: *Optical Properties of Cataclysmic Variable Stars*.

Nakata, Chikako et al. (2014). “OT J075418.7+381225 and OT J230425.8+062546: Promising candidates for the period bouncer”. In: 66.6, 116, p. 116. DOI: `10.1093/pasj/psu108`. arXiv: `1409.0237 [astro-ph.SR]`.

Neustroev, V. V. et al. (2017). "The remarkable outburst of the highly evolved post-period-minimum dwarf nova SSS J122221.7-311525". In: 467.1, pp. 597–618. DOI: `10.1093/mnras/stx084`. arXiv: `1701.03134 [astro-ph.SR]`.

Osaki, Y. (Jan. 1974). "An Accretion Model for the Outbursts of U Geminorum Stars". In: 26, p. 429.

Paczynski, B. and R. Sienkiewicz (May 1983). "The minimum period and the gap in periods of cataclysmic binaries". In: 268, pp. 825–831. URL: `1983ApJ...268..825P`.

Pala, A. F. et al. (2017). "Effective temperatures of cataclysmic-variable white dwarfs as a probe of their evolution". In: 466.3, pp. 2855–2878. DOI: `10.1093/mnras/stw3293`. arXiv: `1701.02738 [astro-ph.SR]`.

Pala, A. F. et al. (2018). "The cataclysmic variable QZ Lib: a period bouncer". In: 481.2, pp. 2523–2535. DOI: `10.1093/mnras/sty2434`. arXiv: `1809.02135 [astro-ph.SR]`.

Pala, A. F. et al. (2019). "The Space Density of Cataclysmic Variables from *Gaia* DR2". In: *arXiv e-prints*, arXiv:1907.13152, arXiv:1907.13152. arXiv: `1907.13152 [astro-ph.SR]`.

Patterson, Joseph (2011). "Distances and absolute magnitudes of dwarf novae: murmurs of period bounce". In: 411.4, pp. 2695–2716. DOI: `10.1111/j.1365-2966.2010.17881.x`.

Rappaport, S., P. C. Joss, and F. Verbunt (Dec. 1983). "A new technique for calculations of binary stellar evolution, with application to magnetic braking". In: 275, pp. 713–731. URL: `1983ApJ...275..713R`.

Rebassa-Mansergas, A. et al. (2007). "Post-common-envelope binaries from SDSS - I. 101 white dwarf main-sequence binaries with multiple Sloan Digital Sky Survey spectroscopy". In: 382.4, pp. 1377–1393. DOI: `10.1111/j.1365-2966.2007.12288.x`. arXiv: `0707.4107 [astro-ph]`.

Rebassa-Mansergas, A. et al. (2013). "White dwarf main-sequence binaries from SDSS DR 8: unveiling the cool white dwarf population". In: 433.4, pp. 3398–3410. DOI: `10.1093/mnras/stt974`. arXiv: `1306.0952 [astro-ph.SR]`.

Riello, M. et al. (2018). "Gaia Data Release 2. Processing of the photometric data". In: 616, A3, A3. DOI: `10.1051/0004-6361/201832712`. arXiv: `1804.09367 [astro-ph.IM]`.

Ringwald, F. A. (1993). "The Cataclysmic Variables from the Palomar-Green Survey". PhD thesis. Dartmouth College.

— (1996). "Population studies of cataclysmic variables". In: *Cataclysmic Variables and Related Objects*, ed. by A. Evans and Janet H. Wood. IAU Coll. 158. Dordrecht: Kluwer, pp. 89–92. URL: `1996cvro.coll...89R`.

Ritter, H. (May 1976). “On the masses and the evolution of cataclysmic binaries”. In: 175, pp. 279–295. URL: `1976mn.175..279R`.

Ritter, H. and A. Burkert (Apr. 1986). “The mass spectrum of the white dwarfs in cataclysmic binaries”. In: 158, pp. 161–173. URL: `1986A&A...158..161R`.

Ritter, H. and U. Kolb (2003). “Catalogue of cataclysmic binaries, low-mass X-ray binaries and related objects (Seventh edition)”. In: 404, pp. 301–303. DOI: `10.1051/0004-6361:20030330`. arXiv: `astro-ph/0301444 [astro-ph]`.

Robinson, E. L. (Jan. 1976). “The masses of cataclysmic variables.” In: 203, pp. 485–489. URL: `1976ApJ...203..485R`.

Savoury, C. D. J. et al. (Aug. 2011). “Cataclysmic variables below the period gap: mass determinations of 14 eclipsing systems”. In: 415.3, pp. 2025–2041. DOI: `10.1111/j.1365-2966.2011.18707.x`. arXiv: `1103.2713 [astro-ph.SR]`.

Scaringi, S. et al. (2013). “Spectroscopic identifications of blue-Hα-excess sources in the Kepler field of view”. In: 428.3, pp. 2207–2215. DOI: `10.1093/mnras/sts189`. arXiv: `1210.3038 [astro-ph.SR]`.

Schmidtobreick, L. (2017). “SW Sex Stars Then and Now: A Review”. In: *Proceedings of Science*.

Schmidtobreick, L., P. Rodríguez-Gil, and B. T. Gänsicke (2012). “The search for SW Sex type stars .” In: 83, p. 610. arXiv: `1111.6678 [astro-ph.SR]`.

Schreiber, M. R. et al. (2010). “Post common envelope binaries from SDSS. VIII. Evidence for disrupted magnetic braking”. In: 513, L7, p. L7. DOI: `10.1051/0004-6361/201013990`.

Speith, R. and S. Kunze (Jan. 2002). “Three-dimensional SPH simulations of stream-disc overflow in cataclysmic variables”. In: *The Physics of Cataclysmic Variables and Related Objects*. Ed. by B. T. Gänsicke, K. Beuermann, and K. Reinsch. Vol. 261. Astronomical Society of the Pacific Conference Series, p. 551.

Spruit, H. C. and H. Ritter (Aug. 1983). “Stellar activity and the period gap in cataclysmic variables”. In: 124, pp. 267–272. URL: `1983A&A...124..267S`.

Sterken, C. and C. Jaschek (2005). *Light Curves of Variable Stars*.

Szkody, Paula et al. (Jan. 2002). “Cataclysmic Variables from The Sloan Digital Sky Survey. I. The First Results”. In: 123.1, pp. 430–442. DOI: `10.1086/324734`. arXiv: `astro-ph/0110291 [astro-ph]`.

Szkody, Paula et al. (Sept. 2003). “Cataclysmic Variables from the Sloan Digital Sky Survey. II. The Second Year”. In: 126.3, pp. 1499–1514. DOI: `10.1086/377346`. arXiv: `astro-ph/0306269 [astro-ph]`.

Szkody, Paula et al. (Oct. 2004). “Cataclysmic Variables from the Sloan Digital Sky Survey. III. The Third Year”. In: 128.4, pp. 1882–1893. DOI: `10.1086/423997`.

Szkody, Paula et al. (May 2005). “Cataclysmic Variables from Sloan Digital Sky Survey. IV. The Fourth Year (2003)”. In: 129.5, pp. 2386–2399. DOI: `10.1086/429595`.

Szkody, Paula et al. (Feb. 2006). “Cataclysmic Variables from Sloan Digital Sky Survey. V. The Fifth Year (2004)”. In: 131.2, pp. 973–983. DOI: `10.1086/499308`.

Szkody, Paula et al. (July 2007). “Cataclysmic Variables from Sloan Digital Sky Survey. VI. The Sixth Year (2005)”. In: 134.1, pp. 185–194. DOI: `10.1086/518506`.

Szkody, Paula et al. (Apr. 2009). “Cataclysmic Variables from SDSS. VII. The Seventh Year (2006)”. In: 137.4, pp. 4011–4019. DOI: `10.1088/0004-6256/137/4/4011`. arXiv: `0901.3177 [astro-ph.GA]`.

Szkody, Paula et al. (Dec. 2011). “Cataclysmic Variables from the Sloan Digital Sky Survey. VIII. The Final Year (2007-2008)”. In: 142.6, 181, p. 181. DOI: `10.1088/0004-6256/142/6/181`. arXiv: `1109.6349 [astro-ph.SR]`.

Thomas, H. C. and K. Beuermann (1998). “Distribution and Space Density of Soft X-ray Emitting Polars in the Solar Neighbourhood”. In: *Berlin Springer Verlag Lecture Notes in Physics* 506, pp. 247–250. URL: `1998LNP...506..247T`.

Townsley, Dean M. and Boris T. Gänsicke (2009). “Cataclysmic Variable Primary Effective Temperatures: Constraints on Binary Angular Momentum Loss”. In: 693.1, pp. 1007–1021. DOI: `10.1088/0004-637X/693/1/1007`. arXiv: `0811.2447 [astro-ph]`.

Warner, B. (1973). “On the masses of cataclysmic variable stars.” In: 162, pp. 189–196. URL: `1973mn.162..189W`.

— (1976a). “Multiple Periodicities in Cataclysmic Variable and White Dwarf Stars”. In: *IAU Colloq. 29: Multiple Periodic Variable Stars*. Ed. by Walter S. Fitch. Vol. 60, p. 247. DOI: `10.1007/978-94-010-1175-4_13`.

— (1976b). “Observations of Dwarf Novae”. In: *IAU Symp. 73: Structure and Evolution of Close Binary Systems*, pp. 85–140.

— (Sept. 1986). “Accretion disc inclinations and absolute magnitudes of classical nova remnants”. In: 222, pp. 11–18. URL: `1986mn.222...11W`.

— (1995). *Cataclysmic Variable Stars*. Cambridge: Cambridge University Press. URL: `1995cvs..book.....W`.

Whyte, C. A. and P. P. Eggleton (Mar. 1980). "Comments on the evolution and origin of cataclysmic binaries". In: 190, pp. 801–823.

Zorotovic, M. and M. R. Schreiber (2017). "The origin of single low-mass WDs: another problem that consequential angular momentum loss in CVs might solve". In: 466.1, pp. L63–L67. DOI: `10.1093/mnrasl/slw236`. arXiv: `1611.07309 [astro-ph.SR]`.

Zorotovic, M., M. R. Schreiber, and B. T. Gänsicke (Dec. 2011). "Post common envelope binaries from SDSS. XI. The white dwarf mass distributions of CVs and pre-CVs". In: 536, A42.

Zorotovic, M. et al. (2016). "Detached cataclysmic variables are crossing the orbital period gap". In: 457.4, pp. 3867–3877. DOI: `10.1093/mnras/stw246`. arXiv: `1601.07785 [astro-ph.SR]`.